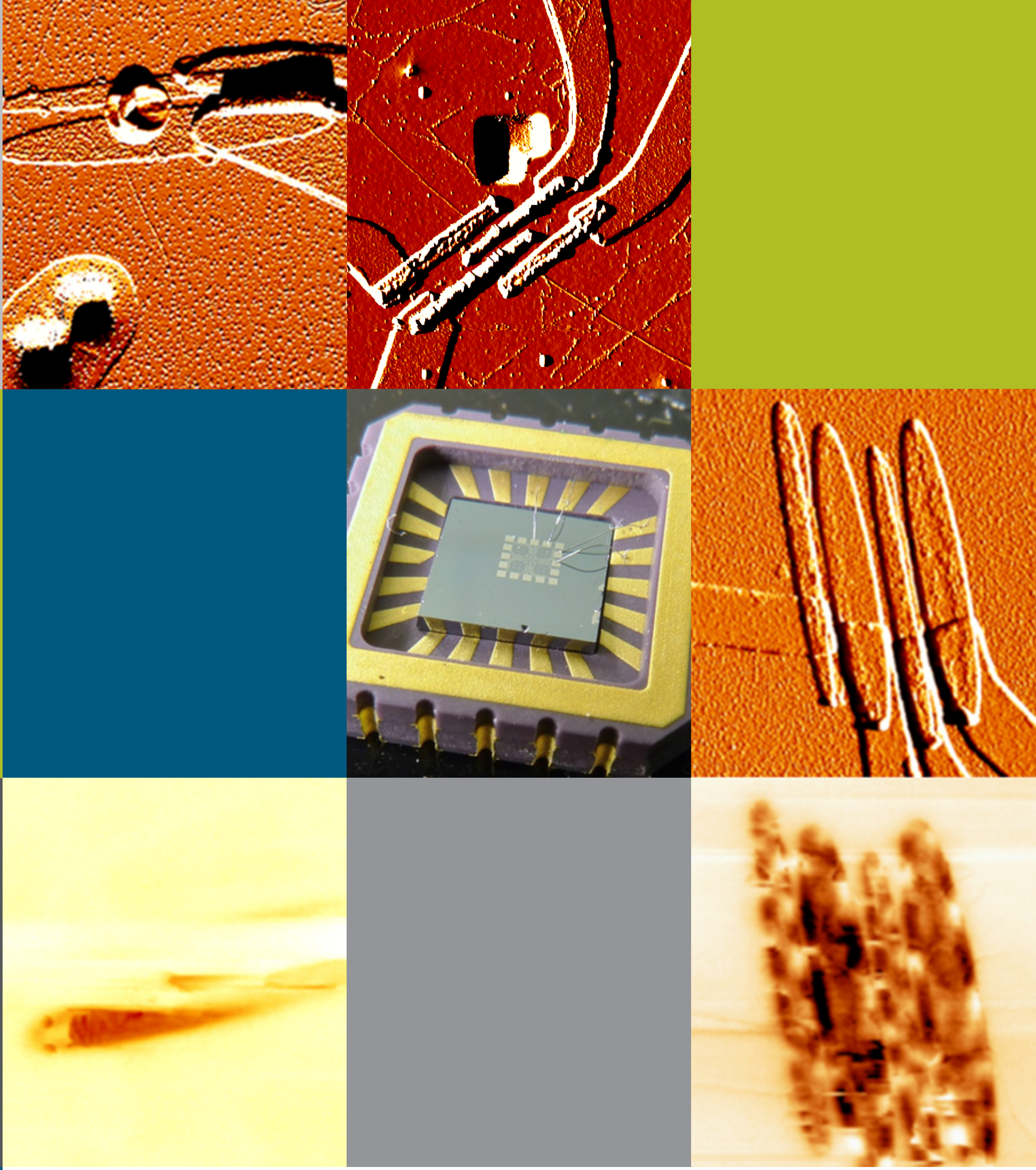

Magnetoresistance and transport in carbon nanotube-based devices

Caitlin Morgan

JÜLICH
FORSCHUNGSZENTRUM

Member of the Helmholtz Association

Schriften des Forschungszentrums Jülich
Reihe Schlüsseltechnologien / Key Technologies Band / Volume 78

Forschungszentrum Jülich GmbH
Peter Grünberg Institute (PGI)
Electronic Properties (PGI-6)

Magnetoresistance and transport in carbon nanotube-based devices

Caitlin Morgan

Schriften des Forschungszentrums Jülich
Reihe Schlüsseltechnologien / Key Technologies Band / Volume 78

ISSN 1866-1807 ISBN 978-3-89336-926-3

Bibliographic information published by the Deutsche Nationalbibliothek.
The Deutsche Nationalbibliothek lists this publication in the Deutsche Nationalbibliografie; detailed bibliographic data are available in the Internet at http://dnb.d-nb.de.

Publisher and Distributor:	Forschungszentrum Jülich GmbH Zentralbibliothek 52425 Jülich Tel: +49 2461 61-5368 Fax: +49 2461 61-6103 Email: zb-publikation@fz-juelich.de www.fz-juelich.de/zb
Cover Design:	Grafische Medien, Forschungszentrum Jülich GmbH
Printer:	Grafische Medien, Forschungszentrum Jülich GmbH
Copyright:	Forschungszentrum Jülich 2013

Schriften des Forschungszentrums Jülich
Reihe Schlüsseltechnologien / Key Technologies, Band / Volume 78

D 464 (Diss., Duisburg, Univ., 2013)

ISSN 1866-1807
ISBN 978-3-89336-926-3

The complete volume is freely available on the Internet on the Jülicher Open Access Server (JUWEL) at www.fz-juelich.de/zb/juwel

Neither this book nor any part of it may be reproduced or transmitted in any form or by any means, electronic or mechanical, including photocopying, microfilming, and recording, or by any information storage and retrieval system, without permission in writing from the publisher.

Kurzfassung

Diese Arbeit befasst sich mit dem Transport und der Kohärenz von Elektronen-Spins in Kohlenstoffnanoröhrchen (carbon nanotubes, CNTs). CNTs zeichnen sich durch ballistischen Transport von Ladungsträgern aus. Die niedrige Ordnungszahl und das sehr seltene Vorkommen von ^{13}C Isotop mit Kernspin führen zu schwacher Spin-Bahn-Kopplung [1, 2] und Hyperfeinwechselwirkung, was ein Indiz für eine hohe Kohärenzlänge von Elektronspins ist. Dies macht CNTs interessant für die Spintronik, wobei die Injektion eines spin-polarisierten Stroms aus einem ferromagnetischen Kontakt in einen nicht-magnetischen Leiter eine anhaltende Herausforderung darstellt. Typischen Ferromagneten formen in der Regel schlechte elektrische Kontakte zu CNTs [3, 4, 5]. Daher wird in dieser Arbeit die Legierung CoPd als neues Kontakt-Material untersucht, bei der der stabile, ohmsche Kontakt von Pd zu CNTs [6] mit der hohen Polarisation von Co und Co-basierten Legierungen [7] kombiniert werden soll.

Dünne CoPd Schichten zeigen eine Oberflächen- und Grenzflächen-Rauhigkeit von weniger als 0.5 nm auf einer SiO_2 Oberfläche. Ausgedehnte CoPd Schichten zeigen ein komplexes magnetisches Verhalten mit einer hohen Magnetisierungskomponente senkrecht zur Oberfläche, die sich in Blasen- und Streifendomänen manifestiert. CoPd Nanostrukturen zeigen allerdings eine leichte Richtung in der Ebene, mit kleiner oder verschwindender senkrechter Komponente und einer hohen Sättigungsmagnetisierung. Die Legierung $Co_{50}Pd_{50}$ zeigte dabei die besten elektrischen Eigenschaften in Kontakt mit CNTs, was auf einen hoch transparenten, ohmschen Kontakt hindeutet.

Lokale Messungen des Magnetowiderstandes (MR) zeigen Abhängigkeiten von der Geometrie der Kontakte, der Temperatur, und der elektronischen Struktur der CNTs. Proben mit nanostrukturierten Kontakten zeigen dabei definiertes und reproduzierbares Schalten. Die Größe des MR steigt mit niedrigen Temperaturen und mit der Stärke der Tunnelbarriere zwischen Kontakt und CNT. Solche Tunnelbarrieren sind intrinsische Eigenschaften von CNTs bei niedrigen Temperaturen und werden durch Grenzfläche zwischen Kontaktmetall und CNT bestimmt, können aber durch Bias und Gate-Spannungen unterdrückt oder verstärkt werden. Zuletzt wurden nicht-lokale Dreipunktmessungen durchgeführt. Während das Signal in lokalen Messungen durch Effekte wie anisotropen Magentowiderstand (AMR), Hall Effekte, und verschieden ohmsche Effekte beinflusst werden kann, detektieren nicht-lokale Messungen nur den reinen Spinstrom und sind daher ein Beweis für Spininjektion und -detektion in CoPd/CNT- Bauelementen. Zusätzlich zeigen Hanle Messungen eine klare Spinpräzession, mit einer Spinlebensdauer $\tau_s = 1.1$ ns.

Zusammenfassend wurde die Spininjektion und detektion in CoPd-kontaktierten CNTs erfolgreich demonstriert. Dieses System bietet alle Vorraussetzungen für ein Spinventil: stark polarisierte Kontakte, intrinsische Tunnelbarrieren, und transparenter Kontakt mit effizienter Injektion, einen nanoskalierten Kanal mit hoher Lebensdauer der Elektronenspins, sowie verlässliche Spindetektion, und bietet somit Zugang zu vielen Informationen für das Feld der Spintronik.

Abstract

This thesis investigates spin transport and coherence in carbon nanotubes (CNTs). In addition to exhibiting ballistic transport, the low atomic number and low abundance of ^{13}C spin nuclei in CNTs lead to low spin orbit coupling [1, 2] and hyperfine interaction, indicating a long spin dephasing length. This makes CNTs a material of interest in spintronics, where injecting a spin-polarized current from a ferromagnetic lead into a nonmagnetic channel presents an ongoing challenge. As typical ferromagnetic materials form unreliable contact to CNTs [3, 4, 5], we investigate a novel contact material, the alloy CoPd. We thus combine the stable ohmic contact Pd forms to CNTs [6] and the high polarization of Co and Co-based alloys [7].

This work begins with a characterization of the material CoPd to find the optimal alloy composition. When grown on an SiO_2 surface, CoPd is shown to have both surface and interfacial roughness of less than 0.5 nm. Magnetically, extended films of CoPd exhibit a complicated behavior with a large out-of-plane component manifesting itself in bubble and stripe domains. However, arrays of fabricated nanostructures of CoPd show a clear in-plane easy axis with little or no out-of-plane component and a high saturation magnetization. Lastly, electrical measurements performed in CoPd-contacted CNTs indicate the formation of highly transparent ohmic contacts. The best performance was found with the alloy $Co_{50}Pd_{50}$.

Local magnetoresistance (MR) measurements show a dependence on the contact geometry, temperature, and the electronic structure of the CNT. Devices with nanostructured contacts resulted in precise, reliable switching. The magnitude of local MR was shown to increase with lower temperatures and in devices where a stronger tunnel barrier was present. CNTs intrinsically form tunnel barriers at low temperatures, and the strength depends on the contact interface, although it may be suppressed and enhanced via tuning of the bias and gate voltages.

Finally, nonlocal three-terminal measurements were performed. While the signal in local measurements may be enhanced by effects such as anisotropic magnetoresistance (AMR), Hall effects, and various local ohmic effects, nonlocal measurements probe only the pure spin current, and are proof that spin injection and detection occur in CNT-based devices with CoPd contacts. Furthermore, Hanle measurements showed a clear spin precession, with a spin lifetime $\tau_s = 1.1$ ns.

In conclusion, we have successfully demonstrated the occurrance of spin injection and detection in CNTs contacted by CoPd. The system has all the requirements of a spin valve device: highly polarized leads, intrinsic tunnel barriers, and transparent contact resulting in efficient injection, a nanotube channel that allows for a long spin lifetime, and reliable spin detection, and can therefore provide much useful information for the field of spintronics.

Contents

1 Introduction **1**

2 Background of magnetism and magnetotransport **7**
- 2.1 Ferromagnetism and the Stoner Criterion . . . 7
- 2.2 Magnetic Anisotropies . . . 9
  - 2.2.1 Magnetocrystalline anisotropy . . . 10
  - 2.2.2 Shape anisotropy . . . 11
  - 2.2.3 Magnetoelastic Effect . . . 13
  - 2.2.4 Exchange bias . . . 14
- 2.3 Magnetic Domains . . . 16
  - 2.3.1 Domain walls and magnetization . . . 16
  - 2.3.2 Domain wall motion . . . 17
- 2.4 Magnetoresistance . . . 19
- 2.5 Conclusion . . . 21

3 Basic properties of carbon nanotubes **23**
- 3.1 Structure of carbon nanotubes . . . 24
  - 3.1.1 Crystalline structure . . . 24
  - 3.1.2 Electronic structure . . . 26
- 3.2 Fabrication . . . 28
  - 3.2.1 Electron-beam lithography . . . 29
  - 3.2.2 Fabrication of prepatterned substrates . . . 29
  - 3.2.3 Chemical vapor deposition . . . 32
  - 3.2.4 Metallization . . . 34
- 3.3 Transport properties in CNT devices . . . 35
  - 3.3.1 Low-temperature transport . . . 36
  - 3.3.2 Spin transport . . . 39
- 3.4 Conclusions . . . 39

4 Characterization of CoPd **41**
- 4.1 Thin films . . . 42

4.1.1 Structural properties of CoPd thin films 43
4.1.2 Magnetic properties of CoPd thin films 45
4.2 Nanostructures 48
4.2.1 Structure design 49
4.2.2 Room temperature magnetic behavior of CoPd nanostructures 51
4.2.3 Temperature dependence of magnetic behavior in CoPd nanostructures 54
4.2.4 Magnetoelastic effect 59
4.3 Electronic interface with CNTs 62
4.4 Conclusions 63

5 Electronic configurations and models 65
5.1 Local measurements 66
5.2 Nonlocal measurements 71
5.2.1 Hanle measurements 73
5.3 Conclusions 74

6 Transport in permalloy-contacted CNTs 75
6.1 Device Fabrication 76
6.2 Transport measurements 76
6.2.1 Device with micro-contacts 78
6.2.2 Device with nanocontacts 79
6.3 Magnetic characterization 85
6.3.1 Magnetic force microscopy of device 86
6.4 Conclusions 86

7 Magnetoresistance and transport in CoPd-contacted CNTs 89
7.1 Micro contacts 90
7.2 Nanocontacts 91
7.2.1 Geometry dependence of local magnetoresistance 92
7.2.2 Sample-specific local magnetoresistance 97
7.2.3 Electronic control and temperature dependence 105
7.2.4 Nonlocal measurements 109
7.3 Conclusions 114

8 Conclusions 115
8.1 Summary of main results 115
8.2 Future work 117

Appendix 121
A Catalyst preparation 121
B Supplementary information for electron beam lithography 121

1 Introduction

The influence of magnetism on electronic transport has long been known and studied. All metals may experience small, isotropic changes in resistance under the influence of an external magnetic field, an effect known as normal magnetoresistance. In the case of magnetic materials, larger, orientation-dependent effects occur. Anisotropic magnetoresistance (AMR), first observed by William Thompson (Lord Kelvin) in 1857, results in a different resistance in a ferromagnetic material depending on whether the electrical curent is flowing parallel or perpendicular to the plane of magnetization [8]. AMR has since been widely studied, and is known to be on the order of only a few percent for typical elemental ferromagnets [9].

The giant magnetoresistance effect (GMR) was discovered in 1988 independently by Peter Grünberg and Albert Fert [10, 11]. GMR was initially observed in layer systems with two ferromagnetic layers separated by a thin nonmagnetic metal. The thickness of the interlayer determined whether the ferromagnetic layers experienced ferromagnetic or antiferromagnetic coupling, according to the interlayer exchange coupling, already discovered by Grünberg in 1986 [12]. When the layers were switched via an external field to be parallel or antiparallel, the resistance through the layers was higher in the antiparallel configuration, due to spin dependent scattering at the interfaces. GMR was later used in a spin valve setup, where the polarization of one of the ferromagnetic layers is pinned by an additional antiferromagnetic layer, via exchange bias. The other layer changes magnetization when an external field is applied. Such spin valves allow for an extremely sensitive readout, and have found many applications, most notably in the field of information technology, where spin valves are important components in hard disk drives and magnetic random access memory (MRAM). The discovery of GMR was deemed so important that Fert and Grünberg won the Nobel Prize in physics in 2007.

While GMR has proven extremely important for magnetic data storage, it is limited by the typical resistance change between parallel and antiparallel alignment being approximately 10-15%. Furthermore, the conductivity mismatch between metals and semiconductors leads to a strongly reduced efficiency of spin injection, limiting the systems in which GMR may be used. A possible solution for these challenges was found in the discovery of a new effect, tunneling magnetoresistance (TMR). TMR was first observed in systems comprised of two ferromagnetic layers separated by a very thin insulating layer, called a tunnel barrier [13]. When a current is applied through the layer, electrons can move from one ferromagnetic layer into the other by tunneling through the insulating barrier. Due to the quantum mechanical phenomenom of spin dependent tunneling, more charge carriers tunnel through the insulating layer if the ferromagnetic layers are aligned in parallel, leading to an increase in resistance in the antiparallel configuration. The magnitude of the TMR effect in a given system is dependent on the polarization of the spin current, and relies on a clean interface to produce a reliable tunnel barrier. Compared to GMR, however, TMR produces an extremely high magnitude resistance difference, with the current record being 600% at room temperature and 1100 % at cryogenic temperatures using a CoFeB/MgO/CoFeB layer system [14]. Many applications attempt to exploit this strong effect. For example, the hard disks in modern computers use read heads which make use of the TMR effect.

As previously described, TMR was initially studied in magnetic tunnel junction (MTJ) systems composed of stacked layers. TMR has also been observed in lateral spin valves [15, 16]. In such a setup, rather than a stack of layers, the sample consists of a nonmagnetic bar or wire with ferromagnetic contacts. An insulating tunnel barrier is deposited between the contacts and the nonmagnet to provide a tunnel barrier. The length of the nonmagnetic channel must be smaller than the spin dephasing length of the material, defined in chapter 5, but the material is not limited to metals, as in the case of GMR. While the principle is the same as for a MTJ, such a device can exploit geometrical constraints, for example limiting the dimensions of a system, as well as make use of one-dimensional materials, which is impossible to realize in a thin-film based MTJ.

Largely due to the discoveries described above, the field of spintronics (spin transport electronics) has developed. Spintronics attempts to create solid state devices in which both the electrical current and the magnetic spin information of charge carriers may be collected and used[17]. The emergence of this field has made it possible to study spin-dependent transport phenomena. However, there are many challenges to overcome in order to further understand and exploit spin transport, such as the optimization of spin injection and detection, the measurement of spin accumulation in a nonmagnet, better ways to fully separate the spin and electronic effects, understanding and optimization of tunnel barrier efficiency, and the ability to electrically control spin transport.

Recently, the challenge of injecting spin polarized electrons from a ferromagnet into a nonmagnetic metal, semiconductor, or molecular structure has become widely studied [17]. Due to the continuing demand for size reduction in electronics, one-dimensional wires and quasi zero-dimensional molecules are materials of special interest for future spintronics applications, and the search is on for a system which can produce a high magnitude, reliable spin transport at or above room temperature. Much work must be done in order to better understand and harness spintronics, and finding a system with which to study the effects of spin-dependent transport is an extremely important research goal.

Carbon nanotubes (CNTs) are potentially an ideal system to use in fabricating a spintronics device. Electronically, they exhibit one-dimensional ballistic transport. Furthermore, due to the low atomic number of carbon, spin-orbit coupling, a major obstacle in spintronics in semiconducting nanowires, is thought to be quite small, although the atomic structure of CNTs potentially causes a small spin-orbit coupling to exist [18]. With the isotope ^{12}C (s=0) comprising almost 99% of all carbon, CNTs have relatively few spin nuclei, and therefore are not influenced by hyperfine interactions. For these reasons, it is suspected that low spin flip probability and high dephasing times occur in CNT-based spin valves [19, 20]. An additional benefit of CNTs is that at low temperatures, a potential barrier forms intrinsically at the CNT-metal contact interface [21], allowing for TMR without the additional step of fabricating a tunnel barrier. The further properties of CNTs, which are on the border between molecules and one-dimensional wires and can act as quantum dots at low temperatures, add to the intrigue of CNTs as a transport system.

However, an ideal nonmagnetic channel through which spins may flow is only one of the requirements for a spintronics device. Efficient spin injection and detection is also critical for the success of such a device. In a lateral spin valve, such as one based on a CNT, spin injection and detection takes place via ferromagnetic contacts. Such contacts must be highly polarized, preferably with magnetization in-plane with respect to the sample. The transition metal ferromagnets, Fe, Co, and Ni, all have high polarizations of 40%, 35% and 23% respectively, as defined by:

$$P = \frac{N_\uparrow - N_\downarrow}{N_\uparrow + N_\downarrow} \tag{1.1}$$

where N is the density of states at the Fermi level of spin up and spin down electrons in the ground state, respectively. Permalloy ($Ni_{81}Fe_{19}$) is also known to have a high polarization of up to 45% [22]. It should be noted that in order to determine the polarization of charge carriers during transport, the electron velocity must be considered as well, as discussed in chapter 2.

Ideally, the spin injector/detector should also have few magnetic domains, to allow for abrupt polarization reversal, and high shape anisotropy relative to magnetocrystalline anisotropy, enabling the control of coercive field via contact geometry. The easy axis should be in-plane with respect to the sample with no out-of-plane components, which cause stray fields. These magnetic behaviors depend on the material used, and can often be influenced by constraining the geometry of the magnet.

A crucial parameter for obtaining reliable spin injection is the interface between the ferromagnetic contact and the nonmagnetic material. Through extensive work in the field, the elemental ferromagnets and permalloy have been shown to form nonreliable contacts to CNTs, often resulting in very high contact resistances, and rough interfaces, which can lead to reduced or uncontrolled spin transport that varies between devices and may even change during thermal cycling of one device [23, 4, 5].

In order to overcome this obstacle, recent work has focused on studying ferromagnetic alloys with a stable ohmic contact to CNTs. Palladium is known to form transparent contacts to CNTs [6]. Furthermore, alloys of Pd and ferromagnetic materials have been shown to maintain a high polarization, even when only small amounts of the ferromagnet is used [24]. Therefore, there is currently much interest in the systems $\mathrm{M}_x\mathrm{Pd}_{1-x}$, where M=Ni,Co,Fe. FePd-CNT devices have been shown to produce TMR [5]. However, results were mixed, with many devices having incomplete, low magnitude switching, which is possibly due to the complicated crystal structure of FePd [7] resulting in undefined magnetocrystalline anisotropy. NiPd has proven to be much more successful as a contact material [25, 26, 27]. However, the strong magnetoelastic effect intrinsic to the material causes the easy axis to be transverse to the long axis of the contact. The effect seems to additionally create intermediate magnetic axes in the out-of-plane and in-plane longitudinal directions, which may result in strong stray-field effects.

In this work, the alloy CoPd is explored as a spin injector/detector material for CNT-based spintronics devices. CoPd alloys are known to have high polarization [7], but while thin films of CoPd have been extensively studied [28], the magnetic behavior of nanostructures, such as contacts, is not well known. Here, we study the CoPd system, and its compatibility to CNTs for spintronics applications. The thesis is organized as follows:

Chapter 2 gives a brief description of the magnetic phenomena relevant to this work. Ferromagnetism is defined, based on the Stoner criterion, magnetic anisotropies and domain formation are discussed, and magnetoresistance is introduced.

As this work is at the border between the fields of low-temperature transport and magnetism, chapter 3 is a second background chapter giving an introduction to carbon nanotubes and deriving the atomic and electronic structure from those of graphene. The growth method and parameters required for device fabrication in this work are presented. Additionally, transport properties of CNTs, specifically those at low temperatures, are discussed, with a focus on both electronic and magnetic transport.

In order to determine the feasibility of using CoPd as a contact material for spin injection/detection, the system was carefully studied with respect to both interfacial and magnetic properties. Chapter 4 begins with the results of a thorough characterization of thin films of various CoPd alloys. It continues with a characterization of fabricated CoPd nanostructures. The chapter ends with a discussion of the benefits of choosing CoPd as a contact material to CNTs. The summarized main results of this chapter have been published in reference [29].

When measuring magnetotransport, specifically in multi-terminal devices, the exact physical properties probed depend on the electronic configuration used for testing. Specifically, local and nonlocal measurements rely on different mechanisms, and can lead to different information. Chapter 5 describes the different measurement schemes it is possible to use for a CNT-based spin valve, and explains where each type of measurement is used in this work, and what this means for the results.

Chapter 6 begins the presentation of transport results obtained in this thesis. Permalloy (Py) is a well-studied ferromagnet that has been used with mixed results as a contact material in CNT-based magnetotransport devices. Here, Py was used as a reference material to determine whether CoPd contacts were an improvement to the system. Geometry dependent and voltage-dependent data are presented here. Results discussed in this section may also be found in reference [30].

Chapter 7 continues the discussion of magnetotransport, moving to the CoPd-CNT system. Two-terminal local measurements are discussed, with emphasis on optimizing the magnetoresistance signal via careful geometrical design and electrical tuning of the devices. In order to definitely determine spin transport, nonlocal measurements are also discussed. Several results discussed in this chapter have been published, and may be found in references [30, 31, 32].

Finally, chapter 8 summarizes the main results of this work and puts into perspective the challenges overcome and those still to be faced in implementing CNT-based spintronics devices. An outlook provides details of future work necessary to further improve the understanding and feasibility of such a system.

The appendix contains supplementary information with regard to the fabrication process, specifically details on the preparation of catalyst material, and the parameters used in electron-beam lithography (EBL), both of which were developed outside the scope of this thesis.

2 Background of magnetism and magnetotransport

Discovering which materials may exhibit ferromagnetism and under which conditions has been critical in the advent of the field of spintronics. The goal of this work, to study spin injection and coherence in CNTs, addresses another current challenge in the field. To accomplish this, reliable spin injection and detection must be achieved via ferromagnetic contacts. Understanding the magnetic properties of the contacts is essential in order to optimize the material system and geometry for spin transport. This chapter begins by explaining the principle behind ferromagnetism, focusing on the Stoner criterion, since this describes the itinerant ferromagnetism of the 3d transition metals Fe, Co, and Ni, which involves the strongly interacting 3d electrons of the Fermi level [33]. Next magnetic anisotropies, which determine preferential magnetization directions in a given material, are discussed, followed by a detailed description of domain wall formation, another magnetic phenomenon aimed at reducing energy in the system. Finally, magnetoresistance is defined, and several systems for measuring various types of magnetoresistance are presented, one of which, tunneling magnetoresistance, is studied in this work.

2.1 Ferromagnetism and the Stoner Criterion

The occurence of itinerant ferromagnetism in bulk 3d transition metals was first explained via mean field theory by Stoner in 1936 [34]. The Pauli principle states that no two electrons can share the same quantum state. Therefore, there are two options for a system with two electrons: stay in the same orbital and have different spins, or have the same spin, but form two orbitals. The most likely of these scenarios is determined by calculating which is energetically favorable to the material. When both kinetic and potential energy are considered, a competition arises.

According to the Heisenberg model, an exchange interaction between all spins of a system is defined by the Hamiltonian:

$$H = -\sum_{i,j} J_{i,j} \vec{s_i} \cdot \vec{s_j} \tag{2.1}$$

where s is the spin quantum number and J is the exchange interaction [35]. In Stoner's model, this leads to the exchange integral, I, which may be considered to be the sum of Coulomb interactions throughout the system, and will lead to a minimum potential energy in the case of a ground state where all spins are aligned in parallel.

However, to obey the Pauli principle, electrons with the same spin must be in different orbitals rather than both occurring in the lowest energy state. The necessity of having one electron in a higher energy orbital increases the kinetic energy of the system by the intrinsic amount ΔE, the level spacing of the material. Figure 2.1(a) and (b) show the two possibilities to minimize energy in a system where I=1 eV is the energy loss due to the exchange interaction. In (a), the energy added by level splitting is higher than I, and the electrons remain in the lower energy state with opposite spins. In (b), the level splitting adds less than 1 eV to the system, and the exchange interaction parameter dominates, resulting in preferentially aligned spins. For a material with relatively high Coulomb interactions and electrons in higher energy states, a high density of states (DOS) occurs at the Fermi level.

A material is therefore ferromagnetic under the condition:

$$U_n(E_F) = I \cdot D(E_F) \geq 1 \tag{2.2}$$

where U_n is the Stoner factor [34]. Figure 2.2(a) plots the Stoner factor vs. atomic number for the elements of atomic number 1 through 50. Only the 3d transition metals Fe, Co and Ni meet the condition. Figure 2.2(b) shows the calculated spin-split density of states of cobalt. It is seen that Co, as a FM, does indeed have a high DOS at the Fermi level. Furthermore, spin splitting occurs, resulting in separate spin-up (majority) and spin-down (minority) bands, separated by exchange splitting $\Delta(k)$=I· M where M represents the magnetization. For the sake of notation, it must be noted that the majority/minority carriers are defined by their overall presence in the band. Due to exchange splitting, it is possible that the minority carriers are actually in the majority at the Fermi level, which is indeed the case for Co, as well as for Ni. The separation of spin up and spin down channels is instrumental in explaining spin-dependent transfer, as it leads to a spin-dependent DOS at the Fermi level, which defines the polarization of the material according to:

$$P = \frac{(Nv)_\uparrow - (Nv)_\downarrow}{(Nv)_\uparrow + (Nv)_\downarrow} \tag{2.3}$$

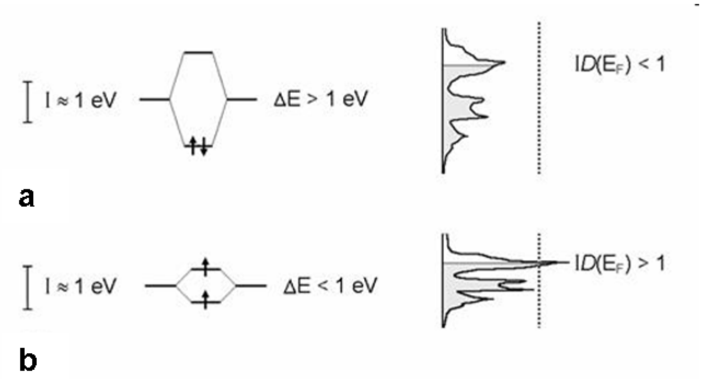

Figure 2.1: The Stoner criterion for ferromagnetism. (a) shows a case where the Coulomb energy gained by keeping electrons in the same orbital is less than the energy gained by splitting the electrons into two orbitals. (b) depicts the opposite scenario. The DOS at the Fermi level is low in the case of (a) and high in the case of (b). Figure adapted from [36]

in the case of a ballistic current, where v is the electron velocity and N is the DOS of the given spin band [37].

It is noted that although they do not meet the Stoner criterion for ferromagnetism, Pd and Sc have high Stoner factors. It has been experimentally shown that such materials become ferromagnets and exhibit high polarization when alloyed with small amounts of FM material [24].

2.2 Magnetic Anisotropies

Most magnetic materials exhibit preferential directions of magnetization, i.e. an easy axis, where only a low field is needed to saturate the magnet, and a hard axis, where saturation magnetization is only reached when a high field is applied. This occurs due to magnetic anisotropy, which is defined by the energy required to change the magnetization of a material from the easy to the hard axis. The main types of anisotropies relevant to this work will be discussed below. The various components of the magnetic anisotropy may be constructive or competitive in defining the magnetic easy axis.

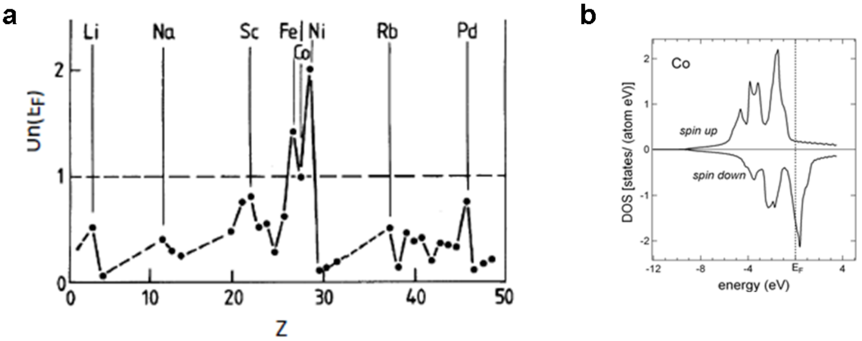

Figure 2.2: (a) Map of Stoner factor calculated for various elements. Only Ni, Co, and Fe exhibit $U_n(E_F) \geq 1$, defining them as the only elemental ferromagnets listed here. (b) shows a spin-split DOS for Co with a discrete DOS at the Fermi level, showing that it meets the Stoner criterion for ferromagnetism. Figures adapted from [38, 39] (a and b respectively).

2.2.1 Magnetocrystalline anisotropy

Although spin-orbit coupling in transition metals is typically only on the order of 1 meV [40], it gives rise to magnetocrystalline anisotropy (MCA), one of the largest magnetic anisotropies. MCA, which is intrinsic to a material, occurs when there is a preferred direction of magnetization along one crystalline axis of the material. Figure 2.3 shows the hard, easy, and intermediate axes of the 3d transition metal ferromagnets Co, Ni, and Fe, which tend to crystallize in the hexagonal close-packed (hcp), face centered cubic (fcc), and body-centered cubic (bcc) structures, respectively.

The energy added to a system by spin-orbit coupling can be defined as:

$$E_{soc} = -m_s \cdot H_{orb} \propto L \cdot S \tag{2.4}$$

where m_s is the spin moment, H_{orb} is the field in the center of the orbital, and L and S are the quantum numbers orbital momentum and spin. In a given material, L tends to lie along one crystalline axis, due to the bonding environment in the crystal. As can be seen in equation 2.4, the energy in the system will be minimized when spins align in a parallel direction, resulting in an easy axis of magnetization. A

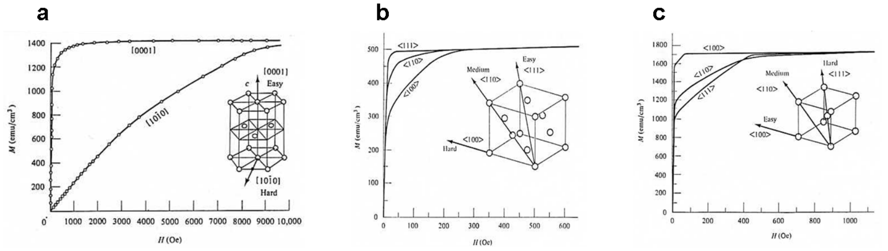

Figure 2.3: Diagrams showing the hard, easy, and medium axes of magnetization of (a) HCP Co, (b) FCC Ni, and (c) BCC Fe. This is caused by magnetocrystalline anisotropy, which is strongest in the case of (a). Image adapted from [41].

hard axis occurs when spins align exactly perpendicular to the orbital momentum, and intermediate alignments will fall between the two extremes[40].

MCA occurs in bulk magnets as well as thin films or nanostructures. However, in a polycrystalline material with randomly oriented grains, the overall effect can be quite small. Only in the case of a preferred growth direction can MCA be very large.

2.2.2 Shape anisotropy

For a sample of a specific geometry, magnetic dipole-dipole interactions give rise to another form of anisotropy, called shape anisotropy. In magnetostatics, it is energetically favorable for dipoles (both atomic and magnetic) to align parallel to one another in order to reduce stray fields. In the case of a thin film, dipole moments tend to align in-plane, which leads to a preferential orientation of magnetic moments. This effect is shape anisotropy, and tends to be higher when the geometrical aspect ratio is higher, although the effect is not linear [42].

For magnets with an appreciable bulk volume, as well as those with further geometrical restrictions, shape anisotropy can further control the direction of preferred magnetic orientation. Magnetism is often defined by the vectors $\vec{B}$, $\vec{H}$, and $\vec{M}$: magnetic induction, magnetic field, and magnetization, respectively, so that:

$$\vec{B} = \mu_0 \vec{H}_0 + \vec{M} \tag{2.5}$$

where μ_0 is the vacuum permeativity. Inside a magnetized sample, where the external field has been removed, this relationship translates to:

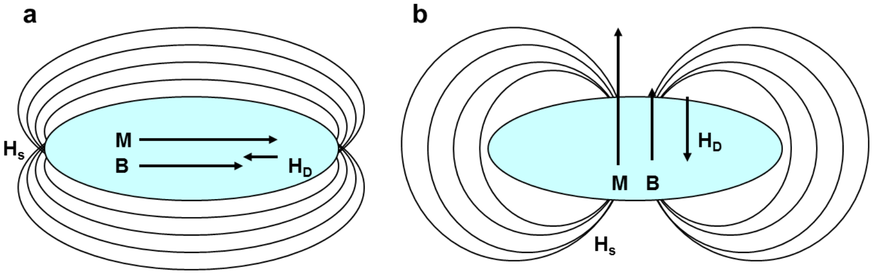

Figure 2.4: An elongated magnetic structure with magnetic field applied along the (a) longer and (b) shorter axis. Shape anisotropy exists because in (a), the demagnetization field is significantly smaller, leading to a preferred magnetization direction.

$$\vec{B} = \mu_0 \vec{H}_D + \vec{M} \tag{2.6}$$

where $\vec{H}_D$ is the demagnetization field, which is generated by the magnetization of the sample, and acts to reduce the overall magnetic moment in the sample. This effect is shown in figure 2.4 for the case of a 2-dimensional oval. It is illustrated that when the sample is magnetized along the long axis of the oval, the demagnetization field is significantly smaller than when the sample is magnetized along the shorter axis. The effect on the overall magnetostatic energy of the system may be considered as:

$$E_{ms} = \frac{N_D M^2}{2} \tag{2.7}$$

where N_D is the demagnetization factor, related in strength to $\vec{H}_D$. The magnetostatic energy will therefore be reduced in the case of magnetization along the long axis of the material, creating a preferred magnetization direction from shape anisotropy[40].

Outside the magnetized sample, another induced magnetic field, the stray field $\vec{H}_s$ is present. This field is also caused by the internal magnetization of the sample, and leads to domain formation, which will be discussed below.

In the case of spin valves, shape anisotropy is often used to achieve an antiparallel alignment of ferromagnetic layers/contacts, as a magnet experiencing higher shape anisotropy requires a higher field in order to change polarization. By controlling their aspect ratios, the coercive fields of the ferromagnets can be defined with respect to one another. This concept is used for all devices discussed in this thesis.

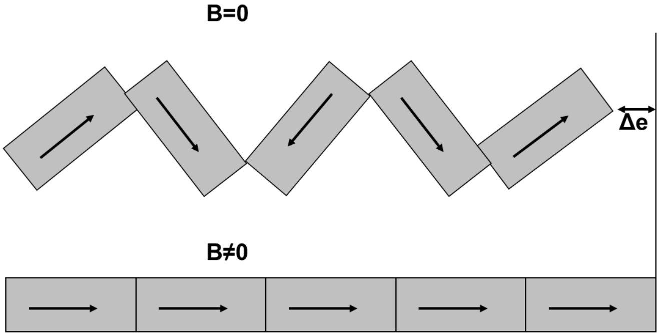

Figure 2.5: Diagram depicting magnetostriction. The upper line shows randomly oriented domains. When an external field is applied, the domains align, as shown in the lower image. This leads to an elongation of the structure, causing mechanical strain. The opposite effect, where physical strain changes the magnetism of a system, is called the magnetoelastic effect.

2.2.3 Magnetoelastic Effect

Mechanical strain leads to another magnetic effect, magnetostriction. Magnetostriction is defined as the change in mechanical strain of a system due to magnetization. Figure 2.5 is a schematic of a magnetic sample with several domains. In the upper image, the domains are oriented randomly. When the sample is exposed to a magnetic field, the domains align along the direction of the applied field. As this occurs, the length of the sample is slightly increased. The change in geometry will induce strain, especially if the sample is grown on a substrate where the size remains constant.

The magnetoelastic effect is the inverse effect to magnetostriction. In this case, the sample experiences mechanical strain, which in turn changes it's magnetic behavior. This can happen, for example, in the case of a ferromagnetic metal deposited at an elevated temperature on a silicon substrate. When the sample is no longer exposed to heat, the metal will shrink due to thermal expansion. Typical substrate materials such as silicon and many ceramics have a much lower coefficient of thermal expansion than most metals, and will therefore experience much less shrinking. This results in a strained bonding at the interface, which in turn affects the magnetic properties of the sample. Cycling the sample to cryogenic temperatures, which is necessary in order to perform many transport experiments, can similarly generate strain leading to the magnetoelastic effect. While the effect can exist in thin films, it is strongly enhanced in nanostructures, where there is a higher edge-to-volume ratio [43].

2.2.4 Exchange bias

As discussed above, ferromagnetic materials have a positive exchange integral, which leads to a parallel alignment of neighboring spins being favorable below the Curie temperature. Antiferromagnets have a negative exchange integral, and therefore an antiparallel alignment of nearest neighbor spins below the Néel temperature is energetically more favorable. When two materials with a positive and a negative exchange integral form an interface, exchange anisotropy, or bias, occurs when the system is magnetized, provided that the temperature is below $T_{Néel}$ of the AFM, which is typically lower than T_{Curie} of the FM. This concept is illustrated in figure 2.6. The layered system is first magnetized to saturation with a positive field. The spins in the FM align parallel to the field, and the spins in the AFM align in a pattern with nearest neighbors having antiparallel spins and a net spin of zero. However, the AFM is influenced by the FM at the interface via exchange coupling, causing the first layer to align parallel to the field in the spin-up direction, as seen in figure2.6(a). This effectively pins the interfacial spins, and a higher field is required to reverse the alignment of the FM when the field is swept in the negative direction. When the layers are subsequently saturated with a negative field, the FM will align in the opposite direction, as shown in figure 2.6(b), however unpinning the interface spins will add energy to the system, requiring a higher coercive field H_c to obtain a spin down alignment. Due to the exchange coupling, the first layers of the AFM at the interface will also slightly change alignment, as shown in figure 2.6(b), but only by a small amount. When sweeping the external field back in the positive direction, a lower field is required to return the FM to the energetically favorable spin-up state. If the exchange coupling is strong, reversal can even occur at a negative field value. Rather than being symmetric around zero, the hysteresis curve of such a system, shown in figure 2.6(c), exhibits a signature shift of the curve toward the negative external field direction.

A FM-AFM junction is often designed purposely to make use of exchange bias. For example, the read head in a hard disk drive relies on exchange bias to pin the magnetic orientation of a bit in an extremely field-sensitive manner. Fe, Co, and Ni all form intrinsic oxides that are AFM. Of specific relevance to this work, Co can form both CoO and Co_3O_4, with Néel temperatures of $T_{Néel}$= 270 K and 40 K, respectively [44]. Therefore, an uncapped FM structure can also exhibit an exchange bias.

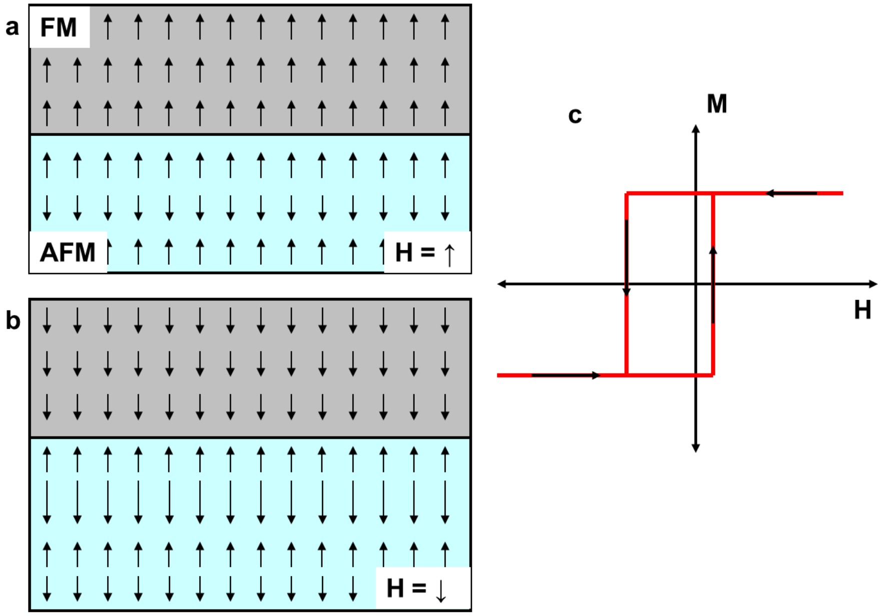

Figure 2.6: Exchange bias in a FM/AFM junction. Spin orientations in the junction when a positive (a) and negative (b) magnetic field are applied. (c) SQUID magnetization curve of a FM/AFM junction showing a clear left-shift toward negative values, indicating exchange bias. Figure based on [41].

2.3 Magnetic Domains

As discussed above, the demagnetization field within a sample, which is induced by the sample magnetization, is minimized via shape anisotropy. Stray fields, which exist externally connecting poles of the sample, are also induced by magnetization of the sample. In order to minimize the external induced field, a ferromagnetic sample will contain regions of different preferred magnetic orientations, called domains. The origin and motion of domain walls, as discussed below, are critical to the overall magnetization of a sample.

2.3.1 Domain walls and magnetization

Figure 2.7 depicts a ferromagnetic sample in remanence. In (a), the sample consists of one magnetic domain. The ends of the FM are poles with opposite surface charges, connected by a large external stray field with a strength:

$$\vec{H}_s = \frac{\vec{B}}{\mu_0} \tag{2.8}$$

In figure 2.7(b), the same sample is divided into two domains of opposite magnetization directions. Stray field lines run between the closer opposing surface charges, and are therefore significantly reduced in strength. Adding more domains can further reduce the stray field, and therefore the energy, of the ferromagnet. The optimal case, with closure domains resulting in zero stray field, is schematized in figure 2.7(c). While the magnetization direction of neighboring domains, dictated by anisotropy, can take on any value, a difference of 90° or 180°, corresponding to in-and out-of-plane, and antiparallel alignment, respectively, is usually observed.

In a ferromagnetic material, an abrupt reversal in magnetization direction between two spins would require a large energy to overcome the exchange interaction. To lower the energy cost, spins rotate gradually over an interfacial area, known as a domain wall. There are several types of domain walls, the most common being Néel and Bloch walls[40]. Néel walls occur when the magnetization rotates in-plane with respect to the wall, and are most commonly found in thin film samples. As a sample approaches bulk dimensions, Bloch walls, which require enough thickness to rotate the spins out-of-plane to the wall, become energetically favorable in what is known as the Néel-Bloch wall transition. The transition thickness has been calculated for several materials, and is usually on the order of several tens of nanometers. In general, a material with a high saturation magnetization and low magnetic anisotropy

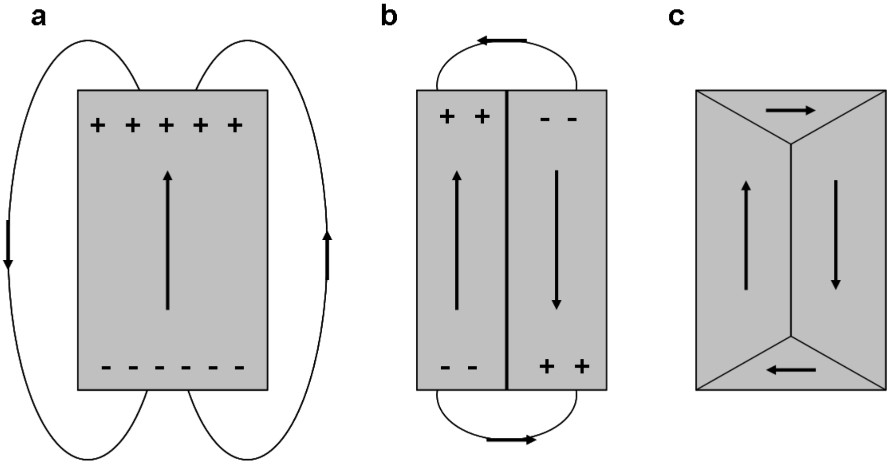

Figure 2.7: Effect of domain formation on stray field in a magnetic structure with (a) a single domain, (b) two domains, and (c) multiple domains. Stray field lines run between magnetic poles, labelled with positive and negative surface charges. Figure based on [45].

will have a higher Néel-Bloch transition thickness than a material with lower magnetization or high anisotropy [46]. The lateral dimensions of magnetic domains are similarly material dependent.

In addition to thickness, the overall amount of FM material influences domain formation, and there is a potential for Néel wall formation in very thin extended films. Also, combinations of in- and out-of-plane rotation, such as vortex domains, may form under the correct conditions. However, this was not observed in this work and will not be discussed further.

2.3.2 Domain wall motion

Applying a magnetic field to a FM will cause the domain walls to move, usually via the domain magnetization rotating slowly into the direction of the applied field, and eventually disappearing as the material becomes saturated. The type of domain wall influences domain wall motion. For example, much energy is required in order to shift an out-of-plane Bloch wall with an in-plane applied field: therefore a higher field will be required to saturate a magnet containing such a wall.

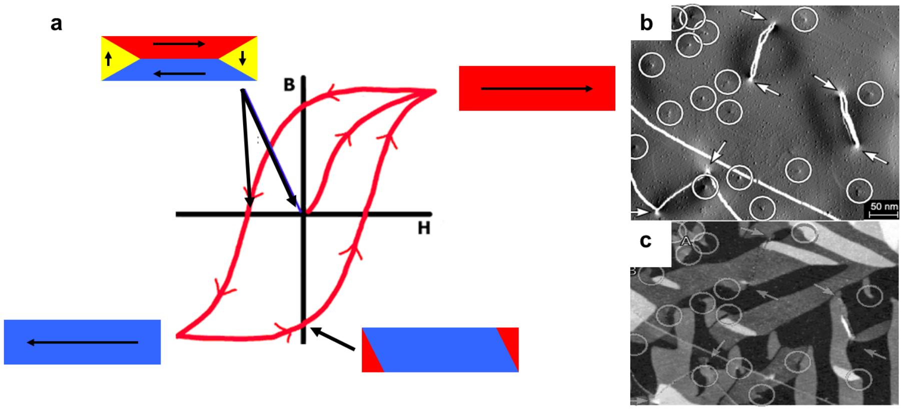

Figure 2.8: (a) Domain wall motion vs. magnetization showing saturated single-domain magnets corresponding to the saturation magnetization, shifting at the remanent field, and closure domain formation when the internal field is zero. The pinning of domain walls by topological defects is shown via height (b) and magnetic (c) imaging. Images (b) and (c) adapted from [47].

Gradual domain wall movement is responsible for the magnetic hysteresis observed in many FM samples. Figure 2.8(a) depicts the gradual displacement of 90° and 180° domain walls in response to an applied external field, and the resulting magnetization curve of the sample. At high positive or negative fields, the magnet is saturated, and therefore without domains. It is observed that at low applied fields, in the case of remanent magnetization, the internal magnetization of the sample increases slowly, with domains first nucleating at the ends of the bar. When the internal magnetization of the sample is zero, closure domains exist, regardless of the externally applied field.

It is possible for domain walls to be pinned in place. Figure 2.8(b) and (c) show how this can take place due to the presence of topological defects in a magnetic film. Such defects can be introduced into a system via fabrication errors, roughness due to evaporation, an initially rough substrate, or addition of impurities. Local changes in magnetic behavior and stray fields at the defects can block domain wall motion, influencing the magnetization of the entire sample. This will occur until a high enough magnetization is applied to overcome the pinning effect. Pinning can also occur in the case where an in-plane magnetic field is applied and an out-of-plane Bloch wall is present in the magnetic material. Therefore, the thickness of a magnetic material must be carefully considered to prevent the formation of out-of-plane domains.

Domain walls can dominate magnetotransport effects, and special care to avoid any such effects must be taken in sample preparation. As will be shown in chapter 7, the presence of domain walls, especially Bloch walls or Néel walls pinned by lithography-induced defects, strongly influences spin injection. When a magnetic field is swept, domains do not always form at the same position in a FM. In the case of spin transport, this can result in unreliable injection and detection. Eliminating domain walls via geometrical constraint is therefore a requirement for spintronics devices.

2.4 Magnetoresistance

A material exhibits magnetoresistance when the application of an external magnetic field effects electrical current flow through the material. All metals experience magnetoresistance (MR), as the mean free path of flowing electrons will be lowered by the Lorenz force when an external magnetic field is applied. As a result, the resistance slightly increases with increasing magnetic field. Less frequently, some materials exhibit a negative MR due to spin disorder effectively increasing the number of scattering channels, in which case the resistance slightly decreases with increasing field [48]. The normal MR effect is independent of sample orientation within the field.

However, larger magnetoresistance is more often found in the case of ferromagnetic materials, and is considered to be orientation-dependent. Such an effect was first discovered in 1857 by William Thompson (Lord Kelvin), where he observed the resistance of pieces of iron and nickel with respect to the direction of an applied magnetic field [8]. He found the electrical resistance to be lowest when the electrical current was propagating in the same direction in which the magnetic field was applied, and highest when the magnetic field was perpendicular to the applied current, an effect that is known as anisotropic magnetoresistance (AMR). AMR originates from spin-orbit coupling and is normally a very small percentage of the overall resistance. In permalloy, which is considered to exhibit high AMR, only 3% is observed, where the magnitude of AMR is defined by:

$$MR = \frac{\Delta R}{R_{\text{parallel}}} \cdot 100\% \tag{2.9}$$

All further values of magnetoresistance are defined with this formula.

In 1988, the groups of Peter Grünberg and Albert Fert independently discovered the phenomenon known as giant magnetoresistance (GMR)[10, 11]. The mechanism behind GMR is spin-dependent scattering. This effect was found in a system comprising two FM layers separated by a thin nonmagnetic layer. Due to interlayer exchange coupling, the two FM layers interact through the spacer layer and align. The resistance in Fe-Cr-Fe bilayers was found to increase when the layers experienced antiparallel alignment, and the effect was greatly enhanced with the use of multilayers [12]. The GMR effect is much larger than AMR. It is also interface sensitive, rather than bulk, because it relies on the mechanism of spin-dependent scattering, where majority and minority spin carriers have different resistances moving through the layers due to the nonequivalent spin-split density of states at the Fermi level of FM materials. In the case of both FM layers being polarized in one direction, the majority carriers can cross both interfaces (FM1-spacer and spacer-FM2) with little scattering, while the minority carriers scatter at both interfaces. According to Mott's two-current model, spin up and spin down electrons have independent current channels. The low scattering from majority carriers therefore results in a low overall resistance for the parallel state. In the antiparallel case, both majority and minority electrons will be scattered at one interface, leading to an overall higher resistance level in the device [49].

While the groundbreaking work of both Grünberg and Fert made use of interlayer exchange coupling to achieve antiparallel alignment in their experiments, this is now often done by creating a so-called spin valve, where the two FM layers have different coercive fields. This can be done by changing the layer thickness of one of the layers, or by using an AFM layer to pin only one of the FM layers. This latter effect is extremely sensitive, even at small fields, and is used in most of the many GMR applications available today [50].

GMR-based sensors and read heads are both smaller and more sensitive than their AMR-based predecessors, due the the higher resistance ratio provided by GMR. Since it's discovery, much research has been conducted in order to find material systems exhibiting high GMR, which would be extremely valuable for industrial application. As of today, a ratio of 80% has been observed at room temperature, although only with a high number of multilayers [51]. Due to extremely high spin polarization at their Fermi levels, a number of Heusler alloys are currently being investigated for GMR applications [52]. Meanwhile, another effect, tunneling magnetoresistance (TMR) has been developed [13]. A TMR device appears similar to the trilayer described above for GMR with two FM layers separated by a thin spacer layer. The important difference is that in TMR, an insulating spacer is used. Electrons must tunnel through the insulator in order to go between the FM layers. As in the case of GMR, resistance is typically much higher when layers are aligned antiparallel.

TMR is further set apart from GMR by it's high magnitude, which has been shown to exceed 600% at room temperature when an epitaxial MgO insulating layer is used [14]. This is due to the fact that during the quantum mechanical process of tunneling, both spin and energy are conserved. The tunneling probability is spin-dependent, again due to the spin split DOS at the Fermi level of FM materials. The high magnitude of TMR makes it a promising effect in the field of spintronics, and injecting spin-polarized current from a FM lead into nonmagnetic channels via a tunnel barrier is currently being intensively investigated in a wide variety of systems.

In this work, TMR is achieved in a lateral (quasi) spin valve system employing two FM contacts to a carbon nanotube, which intrinsically forms a tunnel barrier at low temperatures. In this case, antiparallel alignment is achieved by designing contacts with different geometries. The coercive fields H_c of the contacts are different due to shape anisotropy, and the contact material is carefully tailored to obtain optimal spin injection and detection. The mechanism behind TMR and the variety of effects that become visible in different measurement configurations will be discussed in detail in chapter 5.

Figure 2.9 shows an ideal magnetoresistance curve from a pseudo spin valve. For such a measurement, a constant bias is applied to the device, using the FM contacts/layers as source and drain electrodes. Then, the magnetic field is swept from positive to negative values (blue dashed line) and back(red line). In the region between the coercive fields of the FM layers/contacts, they are aligned antiparallel and the resistance increases. The shape of the curve would hold true for both GMR and TMR.

2.5 Conclusion

Relying only on the short-range exchange interaction, complete magnetic alignment would be impossible in all but the smallest of structures. Magnetic anisotropy and domain formation are critical components to enabling continuous magnetization in structures. Many factors determine the magnetic behavior, and therefore magnetotransport effects, of a system. Several factors, such as magnetocrystalline anisotropy and polarization, are intrinsic to the material. Others, such as shape anisotropy and domain wall formation may largely be controlled via the geometry of the magnet. Still more effects, such as exchange bias and magnetostriction, as well as domain wall pinning, can be influenced by the rest of the material system, such as the substrate, and native oxide. Many of the effects mentioned above are temperature-dependent.

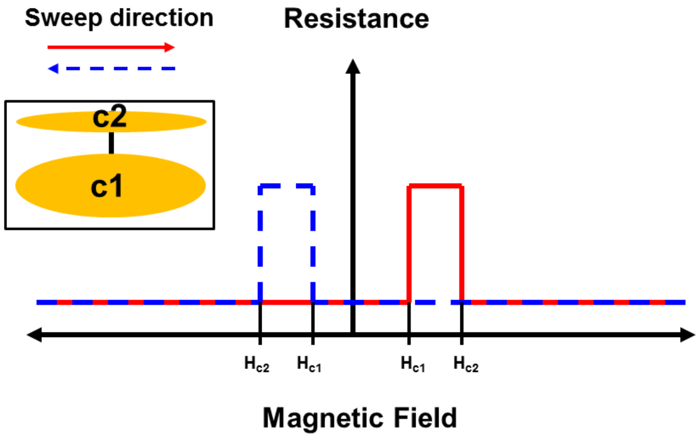

Figure 2.9: An ideal magnetoresistance curve, with peaks in resistance between the coercive fields H_{c1} and H_{c2} of two ferromagnets. For such a measurement, a fixed voltage would be applied. The solid red (dashed blue) curve represents a field sweep in the positive (negative) direction. The inset shows a device with two ferromagnetic contacts of varying dimensions, which would result in different coercive fields due to shape anisotropy.

In order to obtain reliable spin transport, the magnetization of the injecting and detecting FM layer or contact must be well understood. Ideally, the FM should have a high spin polarization, a strong preferred magnetization direction, the ability to achieve antiparallel alignment of injector and detector, and few or no domain walls to act as pinning sites. Such parameters may be obtained for a given sample via a judicious selection of material, geometry, and fabrication parameters based on a thorough characterization process. Therefore, a detailed characterization of the CoPd alloys used in this work will be provided in chapter 4. Magnetoresistance measurements are discussed in chapter 7, and examples of both optimized and nonoptimized spin injection are shown.

3 Basic properties of carbon nanotubes

Carbon nanotubes were initially reported in 1952 by Radushkevich and Lukyanovich [53], and were again observed by Oberlin in 1976 [54]. However, it was only in 1991, after the advent of nanoelectronics, that CNTs became well-known in the scientific community based on a publication by Iijima in 1991 [55]. Iijima further contributed to the advancement of CNTs by discovering single-walled carbon nanotubes (SWCNTs) two years later [56].

Carbon nanotubes have since been extensively studied, and are known to have excellent properties. Chemically, they are extremely stable, with a C-C binding energy of approximately 12 eV. They also have a high room-temperature thermal conductivity (approximately 2 kW/mK), and high elastic modulus and tensile strength (1-5 TPa and 10-100 GPa respectively). Electronically, they may be divided into families of semiconducting and metallic nanotubes. Semiconducting CNTs have high mobilities and have been shown to act as highly accurate transistors, even at room temperature. Metallic CNTs have very low resistivities, exhibit ballistic transport and act as one-dimensional conductors over distances as long as 1 μm. CNTs exhibit extremely high electronic stability, with a maximum current density of 10^9 A/cm^2 [57]. With regard to spin transport, the low atomic number of carbon and rarity of ^{13}C spin nuclei indicate that CNTs should have only small effects from spin orbit coupling or hyperfine interactions, suggesting that the spin dephasing length in CNTs could be quite high. Indeed, it has been experimentally shown to be at least 250 nm for SWCNTs [4]. A further benefit of using CNTs for spintronics applications is the spontaneous formation of tunnel barriers between CNTs and contacts at low temperatures, which is considered necessary for maintaining spin polarization when injecting a spin current from a ferromagnet into a nonmagnetic material[21]. The small diameter of CNTs also makes it possible to fabricate contacts without any further planarization efforts [58]. These characteristics set CNTs apart from materials such as graphene and semiconducting nanowires, indicating that CNTs may be simpler to integrate into spintronics devices. To do so optimally, however, one must consider the intrinsic properties of CNTs, which can largely be understood based on their structure.

This chapter explains details of the crystalline and electronic structure of carbon nanotubes. It will continue to discuss the chemical vapor deposition growth process and the various types of CNTs that may result from it. The work to establish this process was largely performed by Christian Spudat and more details may be found in reference [59]. Fabrication and transport properties of devices, including at cryogenic temperatures, where spin transport measurements are performed, are outlined, and a description is given of various transport regimes that have been observed during low-temperature transport measurements in CNT-based devices. The suitability of nanotubes for use in spin-coherent transport is briefly discussed.

3.1 Structure of carbon nanotubes

A carbon nanotube can be represented by a single layer of graphene that has been rolled into the form of a tube [60]. Therefore, in this chapter, the structural and electronic properties of CNTs are derived from those of graphene.

3.1.1 Crystalline structure

Figure 3.1 shows the crystal struture of a two-dimensional sheet of graphene. It can be seen that the carbon atoms in graphene form a hexagonal lattice with three nearest neighbors. The C-C interatomic distance is $a_0 = 0.142$ nm. The unit cell of graphene is defined by the unit vectors $\vec{a_1}$ and $\vec{a_2}$ and contains two carbon atoms at the positions $(\vec{a_1} + \vec{a_2})/3$ and $(2\vec{a_1} + \vec{a_2})/3$.

The direction in which a graphene sheet is rolled may be defined with respect to the unit vectors and is called the chiral vector, $\vec{c}$. For the formation of a cylindrical CNT, a graphene sheet must be rolled so that $\vec{c} = n\vec{a_1} + m\vec{a_2}$, where n and m are integers. In addition to the chiral vector, a chiral angle may be defined as:

$$\theta = arctan\frac{\sqrt{3}m}{2n+m} \tag{3.1}$$

Nanotubes fall into three categories based on their chiral vector: armchair $(n,\ n)$ and $\theta = 30°$, zigzag, $(n,\ 0)$ and $\theta = 0°$, and chiral, which encompasses all other chiral vectors and results in carbon atoms spiraling around the CNT axis. Many

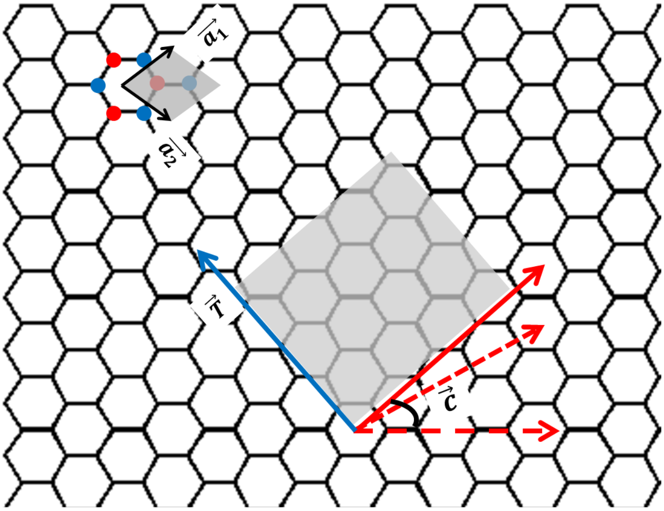

Figure 3.1: The hexagonal crystal lattice of graphene, which may be rolled to form a variety of CNTs. A 2-C unit cell with the atoms marked by red and blue dots is indicated, including the two unit vectors, $\vec{a_1}$ and $\vec{a_2}$. Examples of chiral vectors are shown for the cases of armchair (dashed) zigzag (dotted) and chiral (straight) nanotubes. For the chiral CNT, the axial vector of a rolled CNT is also included.

physical properties of CNTs are strongly determined by their chiral vector, such as electronic structure, as will be discussed in this chapter.

The case discussed above is for a single-walled carbon nanotube. CNTs may also grow concentrically, forming double, or even multi-walled CNTs (D/MWCNTs). Noncoaxial formations of nanotubes, called bundles, or ropes, are also possible. The individual tubes in such structures are held together by van der Waals interactions. In the case of both D/MWCNTs and bundles, CNTs within the structure exhibit arbitrary chiralities.

The diameter of the CNT is also determined by how the graphene sheet is ”rolled.” The smallest CNT ever measured had a diameter 0.3 nm [61], and diameters can easily become one or two orders of magnitude higher, especially when MWCNTs or bundles are concerned. The diameter of a CNT can also influence transport properties, as described below.

3.1.2 Electronic structure

CNTs have a variety of electronic properties, depending on their chirality. The band structures of CNTs of any given chirality may be derived from the band structure of graphene, which has been calculated via a tight binding approximation[62, 63]. Graphene has no band gap, as the valence band π and the conduction band π^* touch at six points at the corners of the Brillouin zone. These points may be reduced to two nondegenerate points, K and K′, and are at the end of cone-like structures in the band diagram, as depicted in Fig 3.2(a).

Around K and K′, there is a linear dispersion relation, defined by:

$$E_{+/-}(\vec{k}) = \hbar \nu_F \vec{k} \tag{3.2}$$

The Fermi velocity ν_F has been determined to be approximately 8×10^5 m/s [64]. This relativistic, quasilinear relation pertains to energies around the Fermi level, and defines graphene as a semimetal or zero-bandgap semiconductor. The dispersion relation at the K and K′ points is well-defined by the Dirac equation with the solution:

$$\hat{H} = \hbar \nu_F \vec{\sigma} \cdot \hat{k} \tag{3.3}$$

where $\vec{\sigma}$ is a Pauli matrix defining whether electrons belong to K or K′[65]. By this definition, electrons at these points resemble Dirac fermions with zero effective mass and a Fermi velocity approaching the speed of light. Hence, the points K and K′ are called Dirac points, at the tips of Dirac cones in the band structure of graphene.

The band structure of a carbon nanotube may be related to that of graphene via the zone-folding approximation [62, 63], which takes into account the change from a two-dimensional sheet to a one-dimensional CNT in which the electron wavevector must fulfill a periodic boundary condition along the circumferential direction of the nanotube:

$$\vec{k_\perp} \cdot \vec{c} = 2\pi p, \quad (p = integer) \tag{3.4}$$

where $\vec{k_\perp}$ is the component of the k-vector perpendicular to the axis of the nanotube and p is an integer. This condition defines specific values to which the k-vectors are limited.

Figure 3.2(b) and (c) show k-space models of the energy dispersion in graphene. The K and K′ points are depicted in blue, and represent the region of high density of

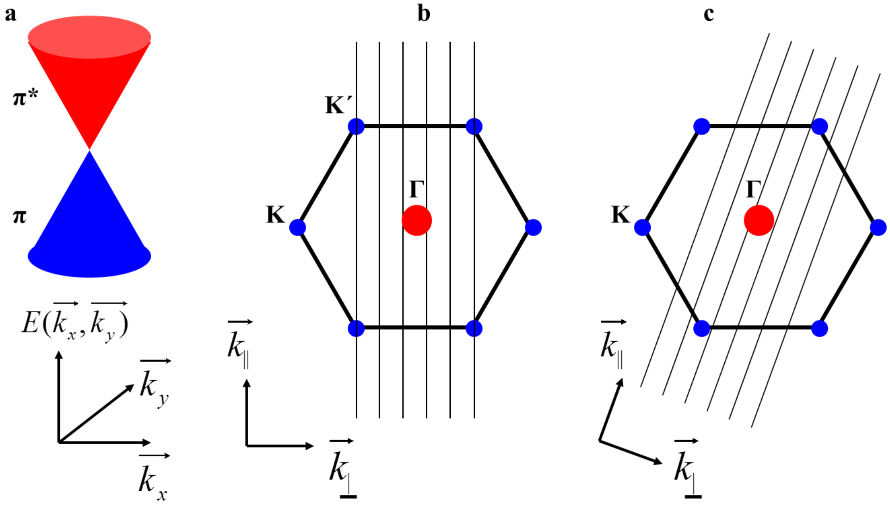
a
b
c
π*
π
$E(\overrightarrow{k_x},\overrightarrow{k_y})$
$\overrightarrow{k_y}$
$\overrightarrow{k_x}$
K′
K
Γ
$\overrightarrow{k_\parallel}$
$\overrightarrow{k_\perp}$
K
Γ
$\overrightarrow{k_\parallel}$
$\overrightarrow{k_\perp}$

Figure 3.2: The band structure of graphene and CNTs. (a) The band structure of graphene contains six Dirac cones, which may be reduced to two nondegenerate points K and K′ where the valence and conduction bands meet, determining transport through graphene. (b), (c) The zone-folding approximations defines specific allowed k-vectors for CNTs based on their chiralities, which determine whether the nanotube is (a) metallic, with an allowed vector going through the k-point, or (b) semiconducting.

states at the Fermi level. The DOS decreases from the K-points to reach a minimum at the central Γ point. Lines are drawn to indicate the allowed k-vectors of nanotubes with two different chiralities according to the zone-folding approximation. In (b), the allowed values include the Dirac point, where there is a clear density of states at the Fermi level. The nanotube is therefore metallic, as a direct result of the linear dispersion at the Dirac points. In (c), the k-vectors allowed by the periodic boundary conditions do not bisect the K-point. In this case, there are no occupied states at the Fermi level, leading to the opening of a band gap, which defines the CNT as semiconducting.

As the allowed states depend on the chiral vector of the CNT, it may be generalized that the metallicity of the CNT may be defined as:

$$(n-m) = 3p, \quad (p = integer) \tag{3.5}$$

According to this rule, 1/3 of CNTs should be metallic and 2/3 should be semiconducting. For a variety of reasons, this is not necessarily the case experimentally. The zone-folding approximation does not consider curvature effects due to the geometry of CNTs. When this is taken into account, only armchair ($n = m$) CNTs will be purely metallic, and other CNTs fulfilling the criteria above for a metallic nanotube develop a small band gap on the order of several meV[63]. Such nanotubes are considered semimetals, and are clearly distinguishable from true semiconducting tubes, with band gaps on the order of 1 eV, scaling inversely with tube diameter. With respect to transport measurements, there are additional reasons for the discrepancy between predicted and achieved electronic behavior. In double or MWCNTs, only one wall must be metallic in order for the transport to have metallic tendencies. Furthermore, at low temperatures, a small strain-induced band gap often opens in purely metallic nanotubes [66], which can be difficult to distinguish from that of a semimetallic CNT.

3.2 Fabrication

In order to fabricate transport devices based on CNTs, individual nanotubes were grown via chemical vapor deposition. Prepatterned substrates were used in order to roughly control the location of CNTs. Small islands of catalyst must also be carefully positioned, in order to ensure that CNTs have enough space between them to allow for contact patterning. The position of CNTs was then defined with respect to alignment markers on the patterned substrate, and individual contact structures could be written. Electron-beam lithography was used in all lithography steps described here. The end result is a multi-terminal transistor-like structure with the CNT acting as a one-dimensional conductance channel.

3.2.1 Electron-beam lithography

Lithography techniques are commonly used in fabrication technology to negatively or positively structure a sample. Lithography steps include coating the sample with a thin layer of polymer resist, then exposing only a selected area of the polymer to a beam of either light or electrons. The beam exposure alters the crosslinking of the polymer chains, and the parts that have been exposed may subsequently be selectively removed with a developer solution. Remaining polymer acts as a mask, which is then used to structure the sample. Photolithography, which utilizes an ultraviolet lamp to expose a pattern, is often the preferred choice, especially for industrial applications, as it may be performed quickly and reliable. The resolution of photolithography is limited to the wavelength of UV light, which is sensitive enough for most purposes. Additionally, the exposed area is selected via a chrome mask being placed over the sample, which is ideal for repetitive processes. In the case of this work, both extremely high resolution on the nm scale and the ability to write a new structure for every sample is required. Therefore, all structure described in this work were written with electron beam lithography (EBL). A description of the parameters used in this work may be found in the appendix.

3.2.2 Fabrication of prepatterned substrates

All samples are fabricated on substrates comprising of heavily p-doped silicon ($\rho = 0.01 - 0.02\ \Omega$cm) covered in 200 nm thermal oxide. Such a substrate ensures that the CNT is grown on an insulating surface while subsequently defining a capacitively coupled back gate for use in future electronic manipulation. The first lithographic step is the prepatterning of a virgin 10 × 10 mm substrate to contain EBL alignment markers, AFM markers, and larger letter and number markers used to distinguish various cells on the sample. The marker structures may be seen as blue, black, and red, respectively, in figure 3.3.

In this step, negative structures were used, as the subsequent high-temperature growth of CNTs was observed to distort metallic marker structures, prohibiting high-accuracy EBL writing. Negative markers are found in the electron microscope for the EBL process through a combination of the edge effect (based on the height difference between the substrate and the etch pit) and the conductivity difference between the silicon dioxide surface and the highly doped silicon bottom of the etch pits.

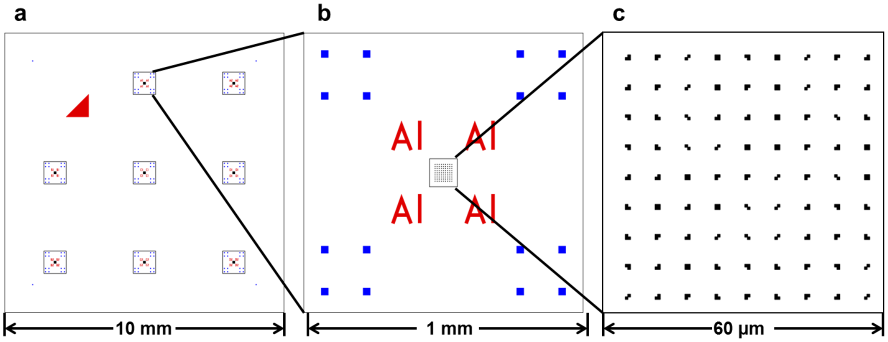
a
b
c
Al
Al
Al
Al
10 mm
1 mm
60 µm

Figure 3.3: A prepatterned substrate showing (a) the entire substrate, (b) a zoom-in to one cell of the substrate, and (c) a further zoom to show AFM markers in the center of the cell. After the sample is finished, it is cut into individual cells to allow for bonding in a chip carrier and mounting in a cryostat.

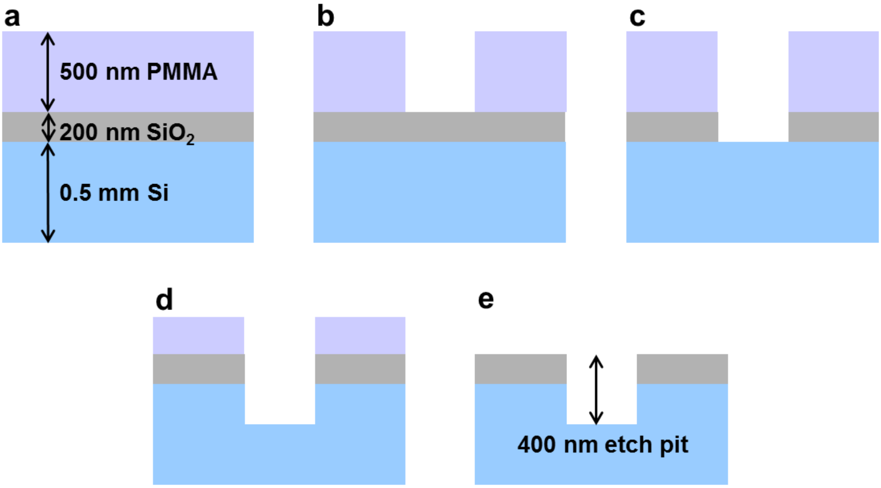
a
500 nm PMMA
200 nm SiO2
0.5 mm Si
b
c
d
e
400 nm etch pit

Figure 3.4: The fabrication steps necessary to prepattern a pristine Si/SiO$_2$ substrate include (a) spin coating a 500 nm - 1 μm thick single PMMA layer, (b) e-beam writing and development, (c) wet etching with BHF to remove exposed oxide, (d) RIBE etch to remove exposed silicon, and (e) stripping the remaining resist.

The lithography process steps developed for the etching of negative markers is detailed in figure 3.4. The steps include (a) spin-coating a pristine substrate, (b) e-beam writing and development, (c) removal of the thermal oxide via wet etching in buffered hydrofluoric acid (BHF), (d) Reactive Ion Beam Etching (RIBE) to remove exposed silicon, and (e) stripping the remaining resist. The last step is important, as the RIBE process destroys the PMMA and it cannot always be removed with acetone. Instead, a commercial resist stripper, such as EKC (Dupont) is used. Remnants of burned PMMA may later inhibit CNT growth. This process results in etched structures of a depth of approximately 400 nm, which includes etching through 200 nm SiO_2 via wet etching and 200 nm Si via RIBE.

RIBE relies on both physical and chemical etching processes. For etching silicon, fluorine-based reactive gases, such as SF_6 and CF_4 are ionized in an argon plasma and then accelerated onto the sample surface, where a combination of physical bombardment and chemical reaction result in the surface of the sample being etched away. The chamber is under vacuum, which removes the etch product. The benefit of combining physical and chemical etching properties is the formation of relatively sharp edges, especially when SF_6, which has a higher mass and therefore more momentum transfer, is used. However, due to the physical nature of the etch, it must be considered that RIBE will etch the entire sample, including the PMMA mask. It was determined that the etch rates for silicon, silicon dioxide, and PMMA are 30 nm/min, 60 nm/min, and 200 nm/min, respectively. Therefore, a very thick layer of PMMA is needed in order to prevent SiO_2 from being etched away, as described above. In this work, a 500 nm thick layer of 600 K PMMA was achieved with a spincoating time of 30 seconds, including a 5 second ramp, at 7000 rpm. The spincoating process was performed twice in order to obtain a 1 μm thick PMMA layer.

Using RIBE alone, the sidewalls of the etch pits were not smooth, as seen in figure 3.5(a). When a relatively large amount of material must be removed from the deepening etch pits, it cannot all escape into the vacuum and redeposits at the side of the pit comprising the remaining resist and the etched substrate. However, when a 6 minute RIBE etch using SF_6 was preceded by a wet etching step, a well-defined marker structure with straight sidewalls was obtained, as shown in figure 3.5(b). Such a marker structure is easily seen both by atomic force microscopy (used to locate CNTs with respect to markers) and SEM (for EBL) and will be unaffected by high temperature growth procedures. This will result in the implementation of high-accuracy device structuring, as needed for nanoelectronics.

Hydrofluoric acid is known to strongly etch SiO_2 but to have no effect on the (001) surface of Si or PMMA. However, the etch rate is extremely fast and difficult to control, often leading to overetching. Therefore, buffered hydrofluoric acid (BHF) which consists of NH_3 (40% in water) and HF (49% in water) in a ratio of 6:1, is

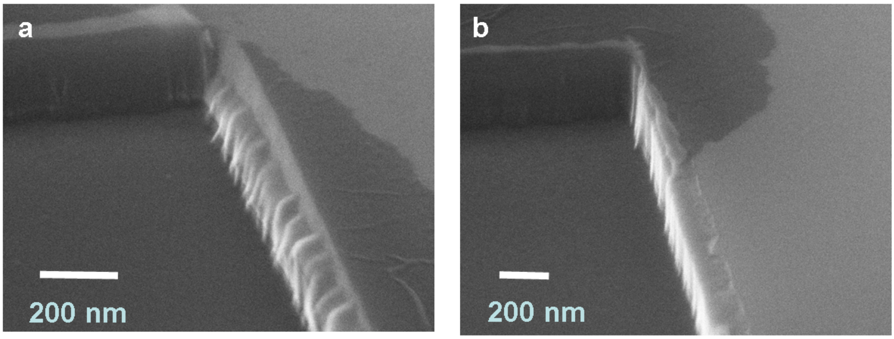

Figure 3.5: Negative marker fabricated by (a) RIBE and (b) a combination of wet etching and RIBE. The walls of the marker in (b) are much straighter, resulting in higher accuracy positioning and writing.

considered to be a better wet etchant for fabrication of nanoelectronics. The exact etching rate depends on many factors, such as room temperature and density of the oxide. Under the conditions used in this work (21 °C and thermally grown oxide) the etch rate was determined to be approximately 0.42 nm/s, necessitating 8 minutes of etching time to remove the 200 nm thermal oxide.

3.2.3 Chemical vapor deposition

Many techniques are currently used to grow CNTs. The most common techniques include laser ablation [67], arc discharge [55], and chemical vapor deposition (CVD). The first two methods result in a large output of CNTs growing as a powder in the deposition chamber. CVD allows for the growth of small amounts of CNTs on a substrate, and is therefore the method used in this work.

CVD relies on the catalytic decomposition of a carbon precursor gas for the growth of CNTs. Many carbon-containing gases are used, such as ethylene, acetelyne, carbon monoxide, and methane. In this work, methane was used as the carbon precursor. The carbon bonds in methane crack at temperatures only slightly lower than the growth temperature used, resulting in little amorphous carbon excess and relatively clean CNT samples. The catalyst material and CVD process used was developed by J. Kong *et* al. [68], and consists of $Fe(NO_3)_3$, Al_2O_3, and $MoO_2(C_5H_5O_2)_2$ nanoparticles in a methanol solution. This is sonicated to produce a solution-based iron-based catalyst. The molybdenum acts to attract amorphous carbon, preventing the active catalyst from being covered and preserving it's catalytic properties [69]. Varying the amount of Mo therefore influences the amount of CNT growth with a

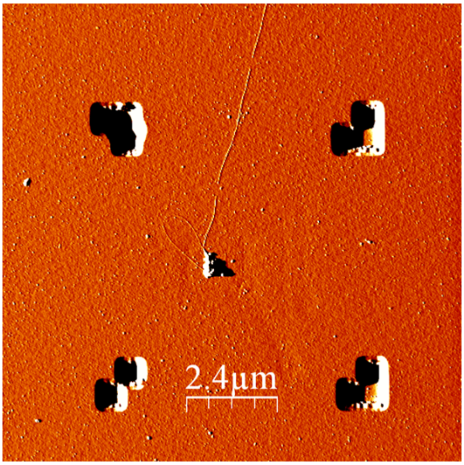

Figure 3.6: AFM image of a sample after marker etching, catalyst deposition and growth, where an isolated CNT is shown to grow from a catalyst island selectively deposited between AFM markers.

given catalyst. The alumina works as a scaffolding material, consolidating the other particles into islands, while iron is the active catalyst.

Such a catalyst may be selectively deposited on the prepatterned substrate. To accomplish this, a standard EBL process for positive structures is used, as detailed in the appendix. After the catalyst liftoff, the substrate contains clear islands of catalyst material at the predefined locations between etched markers, as shown in figure 3.6.

To accomplish the growth process, a quartz tube is inserted into the CVD furnace. The tube is heated to the growth temperature under an argon atmosphere. When the growth temperature is reached, hydrogen and methane are introduced at flow rates of 0.7 L/s and 0.5 L/s respectively. During the growth, methane breaks down to release carbon, while hydrogen is thought to promote CNT growth by acting as a reducing agent for the catalyst. The methane decomposes catalytically at the Fe-based catalyst clusters to form CNTs. When the growth is finished, the samples are cooled to room temperature under an argon atmosphere to prevent oxidation of the CNTs. Once the growth is finished, CNTs are present starting from the catalyst islands and growing in an arbitrary direction, as seen in figure 3.6.

To some extent, it is possible to use process parameters to control the results of growth. As discussed above, tuning the catalyst material can control the yield of CNTs. Also, it was determined by Spudat et al. [59] that changing the growth

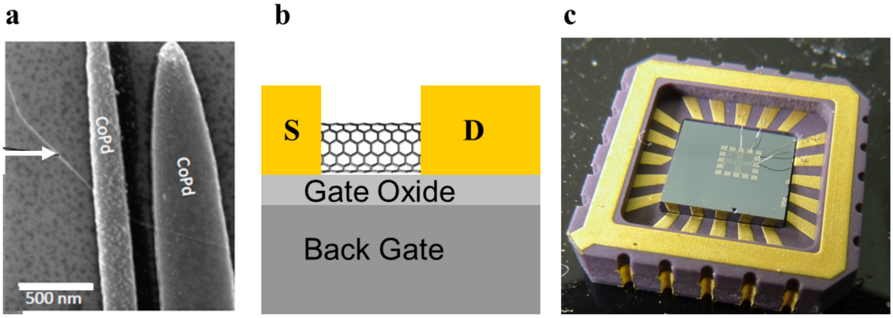

Figure 3.7: A finished device. (a) a scanning electron micrograph of a contacted nanotube (scale bar = 500 nm), (b) schematic of a side-view of the transistor-like device, and (c) a finished device diced and bonded into a chip carrier. The entire chip in (c) is 4 × 4 mm.

temperature affects the number of walls that most CNTs will have, with growth temperatures of 860, 940, and 1030 °C resulting in SW, DW and MWCNTs, respectively. However, CVD is a statistical process, and there will always be deviations in the results. Furthermore, the chirality of CNTs will be arbitrary.

3.2.4 Metallization

After the growth process, CNTs are located via atomic force microscopy. Due to the presence of AFM and alignment markers, it is then possible to define contacts to the CNTs via EBL. The deposition of contact material follows the standard metallization process, detailed in the appendix. Metal deposition is performed via electron-beam evaporation or molecular beam epitaxy, depending on the material used. Wider leads and bonding pads are also written, either in the same step, or separately if a different material is used.

One important difference to the catalyst liftoff is that, in the case of contact and bonding pad metallization, the CNTs are already present on the substrate. Sonication, as well as exposure to high temperatures or certain chemicals, can cause CNTs to break, and is therefore not performed. Instead, the liftoff is performed slowly in warm acetone.

After metallization, the device is complete. Figure 3.7(a) shows a contacted CNT with two ferromagnetic CoPd terminals, through which local electrical and magnetic transport can be measured (see chapter 5). Figure 3.7(b) shows a side perspective of the device, including the backgate, which allows the device to act as a transistor with the nanotube as a channel. In order to measure a CNT-based device, the as-fabricated sample must be diced and bonded into a chip-carrier, as shown in figure 3.7(c). The sample may then be inserted into a cryostat for thermal cycling and measurements.

3.3 Transport properties in CNT devices

When CNTs are incorporated into devices like the one shown in figure 3.7, the transport properties are highly influenced by the chirality of the nanotube. At room temperature, devices with metallic CNTs will exhibit ohmic I-V characteristics and show no gate dependence. Ideally, such CNTs exhibit one-dimensional ballistic transport, defined by perfect transmission of a charge current between two electrodes. Conductance in a quasi one-dimensional system is predicted by the Landauer-Büttiker equation [70, 71] to be:

$$G = \frac{e^2}{h} \sum_i T_i E_F \tag{3.6}$$

where T represents transmission for each conduction channel, i. Since CNTs have both K and K$'$ channels in addition to spin degeneracy, the conductance through a metallic nanotube as transmission approaches one is $\frac{4e^2}{h}$. Experimentally, it has indeed been shown that the mean free path of an electron in a SWNT can be up to 3 μm [72], allowing for ballistic transport, and that the conductance through a metallic CNT with transparent contacts can approach the $\frac{4e^2}{h}$ limit, which corresponds to a resistance of 6.5 $k\Omega$ [73]. However, a higher resistance is often measured, which may be attributed to defects in the CNT itself, and an additional resistance component at the CNT-contact interface. CNTs have been shown to have a high mean free path of electrons due to their low defect density [74], but contact resistance is expected to have large effect on the overall resistance of the device. Certain materials, such as palladium, are known to form transparent contacts to CNTs [6], while others, such as gold, form more opaque contacts.

Devices with semiconducting or semimetallic nanotubes exhibit a Schottky-like I-V characteristic, clearly indicative of a band gap. The height of the Schottky barrier may be controlled by applying a gate voltage, and the device behaves like a field-effect transistor at room temperature [75]. In the case of semimetallic CNTs, the band gap is often small enough that it is hidden by thermal fluctuations at room temperature.

3.3.1 Low-temperature transport

At low temperatures, the transport properties of CNT-based transistors can change drastically, due to an increasing potential barrier. Figure 3.8 shows the clear difference in scaling of resistance versus temperature of a metallic and semiconducting CNT (both with CoPd contacts). (a) is a resistance versus temperature measurement of a metallic nanotube, resulting in the typical decrease in resistance at low temperatures due to the occurrence of fewer scattering events. A bias voltage $V_{bias} = 1$ mV is applied. As is typical of metallic devices, no gate dependence was observed. The upper panel in (b) shows a similar measurement performed on a device with a semiconducting CNT. In this case, a bias voltage of $V_{bias} = 2$ mV is applied. The strong increase of resistance at lower temperatures is a signature of a semiconducting CNT, as is the gate dependence shown in the lower panel. It is not entirely clear whether the CNT is a small-bandgap semiconducting nanotube, or a (semi)metallic CNT developing a strain-induced band gap at low temperatures, as both cases result in the opening of a small band gap at low temperatures, which would be nonexistent or hidden by thermal excitation at room temperature. Figure 3.8(c) plots the low-temperature I-V characteristics of the devices, showing a linear behavior for the metallic CNT, and a Schottky-like behavior for the nanotube with the bandgap, as expected.

In the case of a purely metallic CNT where no tunnel barrier forms due to strain, it may be difficult or impossible to electrically tune the device, as it will not necessarily exhibit gate dependence at 4 K. However, in the case of semiconducting, semimetallic, and metallic CNTs with a strain induced band gap, low-temperature transport may be controlled via gate, offering the opportunity to probe many new effects. Figure 3.9 shows a gate sweep of a device with constant applied bias $V_{bias} =$ 10 mV. When only a small gate voltage is applied, gate-dependent oscillations are present. While the conductance oscillates around zero, it is never completely suppressed, indicating that the device never reaches Coulomb blockade. The energy in the device is too high, and the potential barriers too low, to observe single-electron tunneling, therefore the device operates in the few or multiple-electron tunneling regime, labelled as Regime II. In this regime, the presence of a large tunnel barrier is clearly influencing the device properties and allowing for full electronic control by the gate.

As the gate voltage is swept to more negative values, the conductance behavior in the device is shown to change. While gate-dependent oscillations are still observed, they become broader and the conductance remains at higher and higher values between the oscillations rather than approaching zero. This is caused as the device begins to behave as an opening transistor, rather than simply allowing a few electrons to tunnel at a time. In this opening transistor regime, labeled Regime III, the

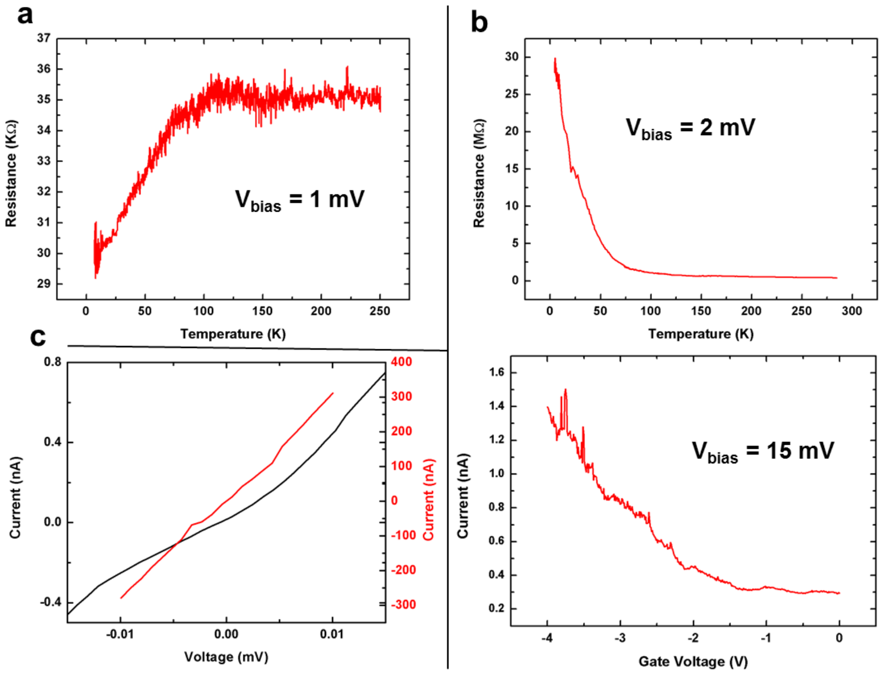

Figure 3.8: Resistance vs. temperature plots for devices containing (a) metallic and (b) semiconducting CNTs. The opening of a potential barrier is observed in (b), which leads to the gate-dependent transport observed for the device in the lower panel. (c) shows 4K I-V characteristics of the two devices, confirming ohmic and Schottky-like behavior of a metallic and semiconducting CNT.

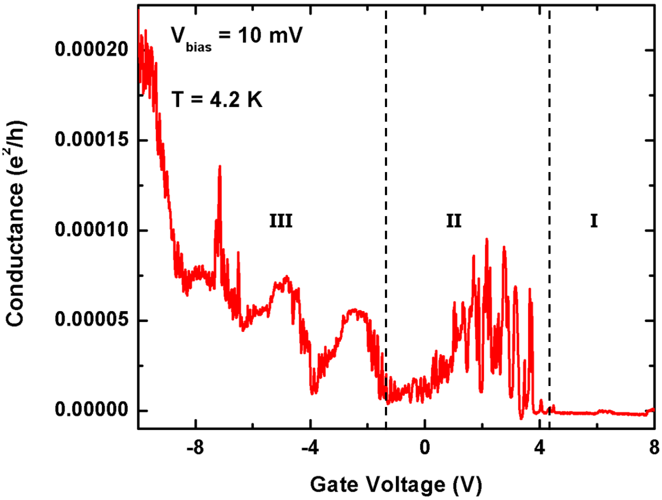

Figure 3.9: A plot of gate voltage versus conductance showing three regimes approximating (I) a closed transistor, (II) tunneling-like behavior, and (III) an opening transistor.

existence of gate-dependent oscillations indicates the continued presence of a tunnel barrier. The device is clearly not behaving as a fully open transistor, as conductance continues to both increase and fluctuate. However, an additional ohmic background component exists in this regime, which must be considered when analyzing data, as further described in chapter 6.

When the gate voltage is increased in the positive direction, the device acts as a closed transistor, with current becoming completely suppressed. As CNTs grown on oxide substrates are considered to be p-doped [75], the polarity of this behavior is expected.

The conducting regimes described above are intermediate transport regimes between two extremes. With highly transparent contacts, it is possible for the device to operate as a Fabry-Perot cavity. The signature of such a regime is a tartan-like interference pattern, and gate-dependent conductance oscillations reaching the full $\frac{4e^2}{h}$, as almost no backscattering occurs at the contacts. Similar transparency has yet to be observed in Co-based contacts, and, as is evident in figure 3.9, although the samples discussed here act as an opening transistor when enough gate voltage is applied, the transparency is far too low to be in the Fabry-Perot regime. At the other extreme, at subkelvin temperatures, when the charging energy of the device is greater than any thermal fluctuations, and the resistance is highly opaque, transport is completely controlled by the quantum mechanical effect of single-electron tunneling. Electrons tunneling into the CNT are essentially trapped between two barriers formed by the contacts, and the system is in full Coulomb blockade. This regime is highly studied, largely due to its interesting properties and stability [25], however single-electron tunneling is never resolved in this study, where all data were taken at a temperature T=4 K.

3.3.2 Spin transport

Due to their low atomic number and few spin nuclei, the spin-scattering effects of spin orbit coupling and hyperfine interaction are considered to be relatively weak in CNTs, leading to the assumption that there is a large spin dephasing time and spin flip length. Experimentally, a spin flip length on the order of 250 nm has been determined for SWNTs [4], and various groups have measured tunneling magnetoresistance in nanotubes with 200-500 nm contact spacing, although not always taking spurious effects such as (T)AMR and the magnetocoulomb effect into account, as discussed in chapter 6. With respect to fabrication, CNTs are promising for integration in spintronics devices. The spontaneous formation of an intrinsic tunnel barrier at low temperatures removes the challenge of fabricating an insulating tunnel barrier, as is the case for graphene, or semiconducting nanowires. Furthermore, the relative flatness of CNTs, when compared to materials such as InAs nanowires, is ideal for contact metallization, without the need of an additional planarization step, which is time consuming and would be extremely difficult to perform on a large scale [58]. However, in order to accurately measure and exploit the spin flip length in CNTs, a means must exist for the injection and detection of highly polarized spin currents. This is the goal of this thesis and will be discussed extensively in chapters 4-7.

3.4 Conclusions

In this chapter, the structural and electronic structure of carbon nanotubes was derived from that of graphene. It was shown that the properties of individual nanotubes are extremely sample-specific, based on factors such as chirality or number of walls. Such properties are difficult to predetermine, but will highly influence magnetotransport in CNT-based devices. Electronically, the behavior of CNT-based devices may fall into several regimes, described above, and may be tuned via the application of a gate voltage. The electronic state of a device has also been shown to have a large influence on magnetotransport, which will be discussed extensively in chapters 6 and 7

The diameter of a nanotube influences spin orbit coupling, which is typically negligible, but increases with decreasing CNT diameter [18]. At diameters below one nm, spin orbit coupling could potentially have a large effect on magnetotransport, including shortening the spin lifetime in a CNT.

Furthermore, as magnetoresistance in CNT-based quasi spin valves is widely thought to be tunneling magnetoresistance [4, 5, 25], the strength of the intrinsically formed potential barrier, which is chirality dependent, is expected to strongly influence the magnitude of the signal[76]. A high ΔR may be expected in the case of a device incorporating a CNT with a large potential barrier, whereas a low tunnel barrier is likely to result in both low magnitude and quality of TMR. The optimal electronic properties of a CoPd-contacted CNT-based device are studied in detail in chapter 7.

4 Characterization of CoPd

In a typical CNT-based transport device, most of the resistance is a direct result of the contact-nanotube interface. Both the interfacial quality and the electronic properties of the contact metal will strongly influence the device performance. It is therefore necessary to choose a contact material that forms a smooth interface to the CNT, and which leads to the formation of reasonably high-transparency devices. Gold and palladium have both been shown to form good contact to CNTs, with palladium being used to create especially transparent contacts[6]. For spin-transport measurements, the additional qualities of ferromagnetism with high spin polarization, preferably with a quantization axis in-plane of the sample, a coercive field that is easily manipulated via shape anisotropy, and a high remanent magnetization, to allow for step-like switching of the magnetization are also required. Traditional ferromagnetic materials, cobalt, iron, nickel, and permalloy have been used for initial experiments with CNT spintronics devices. However, they often led to high-resistance devices that were unable to maintain a constant magnetic signal and didn't survive multiple thermal cycles[4, 5, 23, 77].

Recently, research has been focused on using diluted ferromagnetic alloys to contact CNTs. Alloys of Pd and elemental FMs cobalt, nickel, or iron have been shown to maintain ferromagnetic properties even when only a small percentage of the FM element is used [24]. In combination with the excellent electronic properties expected of a palladium-based alloy, $\mathrm{M}_x\mathrm{Pd}_{1-x}$ where M = Ni, Co, or Fe is therefore a promising family of materials for creating an optimal contact material. However, results have been mixed. It has been shown that magnetic properties of FePd nanostructures, i.e. contacts, are strongly influenced by geometry and composition. Nonabrupt switching of at least one terminal was often observed, and was attributed to a large out-of-plane component in the magnetization [5]. NiPd contacts have been more successful, leading to extremely reliable devices in which a strong electronic control of magnetotransport could be observed [25, 26]. Results were optimized by applying a magnetic field transverse to the long axis of the contact, as NiPd displays an unexpected easy axis in that direction [26, 27]. Studies of both alloys point to the fact that in order to achieve optimal spin injection and detection in a CNT, the materials must first be thoroughly characterized with respect to both structural and magnetic behavior.

As they are expected to have a high spin polarization [7], we study alloys of the type Co_xPd_{1-x}. As a member of the CoPt group, CoPd has already been fairly extensively studied with respect to its magnetization and exchange bias properties. However, previous studies focused solely on thin-films or multilayers of CoPd [7, 28]. An investigation of the properties of fabricated nanostructures, where the magnetization may be highly affected by geometrical constraints, is necessary. For application in a quasi-spin valve, it is especially important that magnetic properties remain good at cryogenic temperatures, as CNTs have been shown to quickly lose their ability to transport spin as temperature rises over 4 K [77].

The first section of this chapter will discuss the growth and characterization of thin films of a series of Co_xPd_{1-x} alloys. The growth, structural properties, and magnetic behavior of such films are investigated in this work.
The following section will focus on nanostructures of $Co_{50}Pd_{50}$. The structures are designed to resemble contacts used in CNT-based transport devices. The fabrication process involves creating an array of such nanocontacts, which is then used to determine the magnetic properties of small nanostructures of CoPd. In order to accurately study the magnetic behavior of contacts under cryogenic conditions, temperature-dependent data was collected. In order to interpret such data, an in-depth discussion of the energy balance of the CoPd system is required. Finally, it is shown that CoPd creates stable low-ohmic contacts to CNTs that are capable of forming tunnel barriers at low temperature.

The main results of this chapter were published in reference [30].

4.1 Thin films

Thin films of CoPd were deposited via room-temperature molecular beam epitaxy (MBE) using coevaporation from individual Co and Pd targets. The substrates used in this investigation were Si/SiO_2 wafers, in order to replicate the environment of a CNT-based device equipped with a back gate. The 200-nm thick thermally-grown oxide exhibited no long-range crystallinity. For thin-film samples, film thicknesses were chosen as 20 and 40 nm, as these thicknesses are commonly used for contacts in devices. The alloys Co_xPd_{1-x} where $x \cdot 100 = 20, 30, 50$ and 70 were investigated in this work. $Co_{20}Pd_{80}$ was found to have only a very slight in-plane component of magnetization and will therefore not be considered here. Composition was determined in situ via Auger electron spectroscopy and later confirmed via X-ray diffraction.

4.1.1 Structural properties of CoPd thin films

In addition to confirming the alloy composition, X-ray diffraction (XRD) was performed in order to determine crystallinity and orientation in MBE-grown CoPd layers. 40 nm thick thin films of varying concentrations were studied, and the data is presented in figure 4.1. For all concentrations, only one diffraction peak was observed, corresponding to a (111) orientation in the face-centered cubic CoPd lattice. This indicates a strong preferential growth orientation, which is in good agreement with previous observations of CoPd films grown on amorphous oxide substrates [28]. The lack of any peak corresponding to pure palladium or to cobalt, which is hexagonal, indicates that the film consists entirely of a solid solution. The lattice constant recorded during these measurements is 3.73 Å for $Co_{50}Pd_{50}$. As expected, the lattice constant for the alloy $Co_{30}Pd_{70}$ is 3.77 Å, shifting closer to that of pure fcc Pd, which is 3.95 Å[78]. When the Co content is raised to $Co_{70}Pd_{30}$, the lattice constant is 3.64 Å, tending toward that of fcc cobalt (3.55 Å) [78]. Such a linear variation of the lattice constant with respect to concentration conforms with Vegard's law, confirming that the in situ determined concentrations are accurate.

From the full width half maximum (FWHM) of the diffraction peak, we determine that the sample exhibits a polycrystalline texture, with an average crystallite size of approximately 20 nm, confirming observations from atomic force microscopy. These crystal domains are quite small, and are on the same order of magnitude as expected for local ordering in the amorphous oxide the CoPd is deposited on. Differences in peak intensity for the different alloys may be attributed to sample alignment, and peak fitting indicates a similar polycrystalline domain size for all CoPd compositions.

It is important to know the crystal structure of a material, as it can strongly influence both electronic transport and magnetism. Low surface and interface roughness are also important material parameters for a potential contact material. Roughness can affect the magnetization, making it difficult to control. Furthermore, a rough substrate-contact interface can decrease the already small area where the metal is contacting the CNT, resulting in poor electronic control. After deposition, atomic force microscopy (AFM) was used to check the surface roughness of samples. The inset of figure 4.2 shows an AFM image from a 20 nm thick $Co_{50}Pd_{50}$ thin film. The height scale indicates a topology with average roughness of approximately 0.5 nm. Round polycrystallites with an average diameter of 10-20 nm are observed. Varying the composition or film thickness of the alloy had no visible effect on the surface roughness.

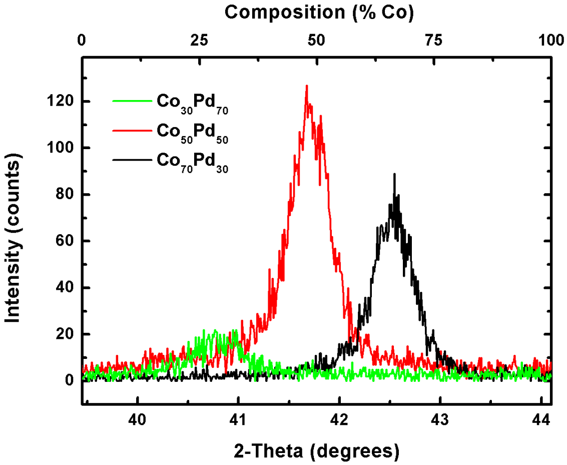

Figure 4.1: X-ray diffraction data of various alloys of CoPd thin films. All alloys exhibit face centered cubic structure with a (111) preferred growth orientation. Peak intensity is dependent on alignment, which varies between samples. The upper axis corresponds to the alloy composition with the left and right ends corresponding to the expected (111) peak positions of pure Pd and Co, respectively.

X-ray reflectivity (XRR) measurements were employed to confirm the thickness and surface roughness of samples, and to determine the roughness at the substrate-metal interface. All X-ray measurements were performed in a Bruker single-crystal diffractometer using standard Cu-K_α radiation. While a standard X-ray diffraction scan is taken by rotating the angle of the detector with respect to the X-ray source, XRR measurements are performed by keeping the source and detector at the same angle with respect to the sample and measuring the reflected X-ray intensity (in a setup with a stationary source, this is achieved by rotating both the sample and the detector). Oscillations in the intensity are a result of interference resulting from density, thickness, surface roughness, or interface roughness. Known parameters (e.g. density if the composition is known) and algorithms based on the Fresnel Laws are then used to fit the measurement and determine unknown parameters [79]. For a low-roughness film, an accuracy of 0.5 nm is expected. Figure 4.2 shows an XRR scan of the same 20 nm thick $Co_{50}Pd_{50}$ imaged via AFM in the inset. For the curve fitting, the density was taken to be a mixture of that of Co and Pd, as X-ray diffraction had proven the alloy to be a homogeneous solid solution. Fitting confirmed the thickness of 20 nm, which was measured via in situ quartz crystal microbalance (QCM) during deposition. Furthermore, a surface roughness of 0.25 nm and an oxide-CoPd interface roughness of 0.43 nm were calculated. These values are within the error margin of the fitting, proving that the CoPd film was extremely smooth.

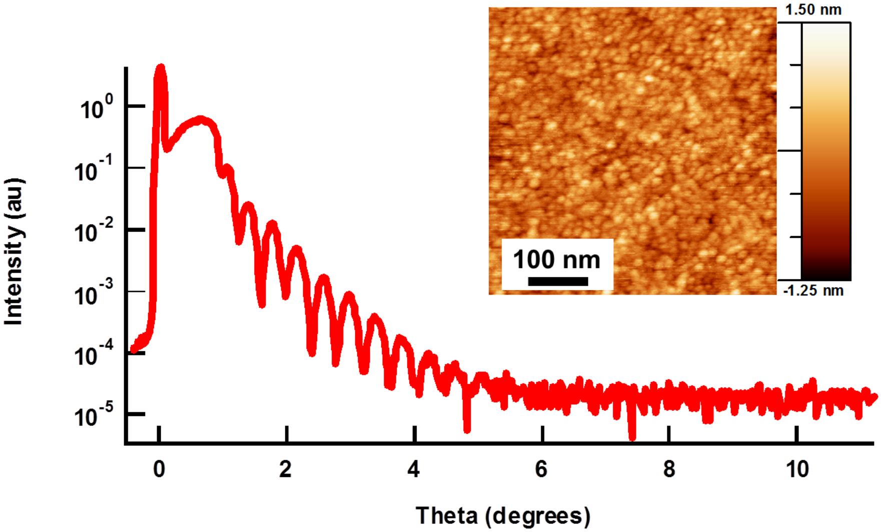

Figure 4.2: Low roughness of $Co_{50}Pd_{50}$. An X-ray reflectivity scan showing low surface and interface roughness in a CoPd thin film. Inset: atomic force micrograph of $Co_{50}Pd_{50}$ confirms low surface roughness and shows growth in 10 - 20 nm polycrystalline domains.

4.1.2 Magnetic properties of CoPd thin films

In standard non-contact mode AFM, a tip is scanned along a sample surface. On a flat surface, the tip feels a constant force, due to the van der Waals attraction between the tip and the sample. When surface roughness or other features are encountered, the tip will be deflected up or down, in order to maintain a constant force. This deflection can be measured, giving a highly accurate topological map of the sample. Magnetic force microscopy (MFM) employs a similar technique, but uses a tip coated with ferromagnetic cobalt. The magnetic stray field from this tip will interact with the stray field of domain walls or out-of-plane domains of a ferromagnetic sample, again deflecting the tip. After subtracting the data obtained from topology, MFM gives an accurate image of magnetic domains within a sample. MFM can be performed with a previously magnetized sample in remanence, as is the case here, or in a setup with a magnet.

MFM was performed on extended CoPd stripes of thickness $t = 40$ nm in order to determine the magnetic domain structure. Figure 4.3 shows results for the compositions (a) Co$_{30}$Pd$_{70}$ and (b) Co$_{50}$Pd$_{50}$. In the Co$_{30}$Pd$_{70}$ sample, bubble-like domains appear in a random pattern, whereas in the Co$_{50}$Pd$_{50}$ sample, the domains are stripe shaped and align along the longer axis of the patterned stripe, the direction in which the sample was previously magnetized. A similar domain structure has been observed for CoCr samples with a strong out-of-plane component, in which the creation of so-called bubble domains was observed [80]. The size of the domains are on the order of 1 μm along the magnetization direction of the CoPd stripe. It is important to avoid such domains in contacts for spintronics applications, as the position of domains will alter during magnetic field sweeps, leading to irreproducible switching behavior, as has been previously reported by Meyer *et* al. [31].

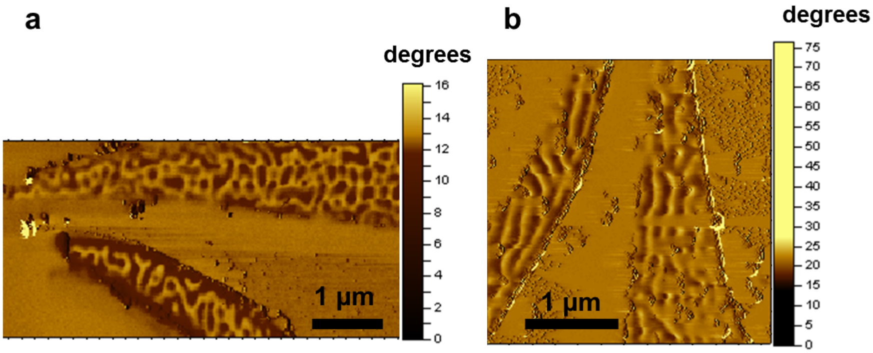

Figure 4.3: Magnetic force micrographs of extended stripes of (a) Co$_{30}$Pd$_{70}$ and (b) Co$_{50}$Pd$_{50}$ taken in remanence after magnetization along the long axis of the stripes show the formation of domains indicating a strong out-of-plane component of magnetization. The dimensions are similar to that of a thin film

As MFM shows a complex magnetic structure of CoPd, it is necessary to gain further understanding of the magnetic properties of the material. The magnetic behavior of the 40-nm thick thin film samples was further studied via SQUID magnetometry. Figure 4.4 shows in and out-of-plane magnetization data for the series of CoPd alloys. For the in-plane magnetization data presented in figure 4.4(a), the coercive field $\mu_0 H_c = 45$ mT is independent of the sample composition. The saturation and remanent field, however, are larger for higher Co content, making a shift from a hard-axis type hysteresis for the alloy Co$_{30}$Pd$_{70}$ to an easy-axis hysteresis curve for the alloy Co$_{70}$Pd$_{30}$. The magnetization is thus pushed in-plane with increasing Co content. Allowing for slight differences due to preparation techniques, saturation magnetization values are in agreement with previously reported data [81, 82]. Due to shape anisotropy, a predominantly in-plane magnetization is expected for the thin films.

Figure 4.4(b) shows a more complex behavior of the out-of-plane magnetization for different Co concentrations. The $Co_{70}Pd_{30}$ alloy exhibits a clear hard axis magnetization for the out-of-plane magnetized sample, which is still a significant out-of-plane contribution to the total magnetization. The two other compositions studied have an out-of-plane component that resembles a closed loop at zero applied field, but opens to have significant hysteresis at larger fields. $Co_{30}Pd_{70}$ has a significantly more square hysteresis than $Co_{50}Pd_{50}$, and opens much closer to zero, indicating that the out-of-plane component is more favorable. The shape of the magnetization curves corresponds well with that observed for CoCr samples with bubble domains [80], which were also observed in the MFM data discussed above.

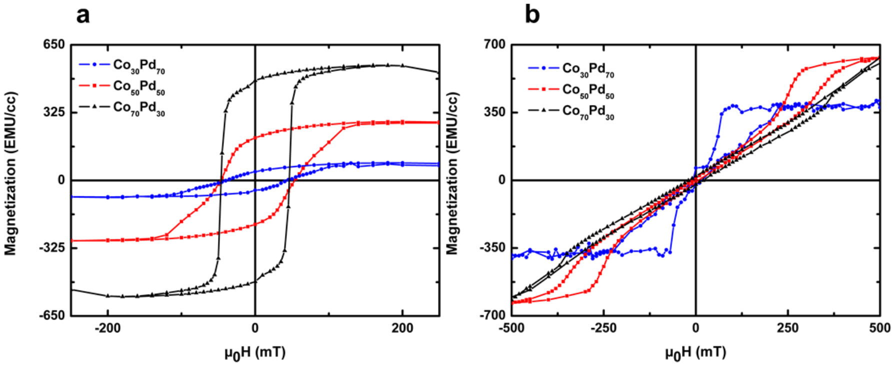

Figure 4.4: (a) In-plane and (b) out-of-plane SQUID data recorded on 40-nm thick $Co_{30}Pd_{70}$, $Co_{50}Pd_{50}$, and $Co_{70}Pd_{30}$ at room temperature. A paramagnetic baseline was subtracted.

The in-plane and out-of-plane components of the magnetization of a 20 nm thin $Co_{50}Pd_{50}$ sample are compared in figure 4.5. The coercive field of the in-plane component is reduced by a factor of 10 compared to that of the 40 nm film, while the out-of-plane hysteresis seems to have almost disappeared. The absence of an out-of-plane component of magnetization indicates the occurrence of a Bloch to Néel wall transition in $Co_{50}Pd_{50}$ films between 20 and 40 nm, a value similar to that found in other transition metal alloys [5]. Contacts with thickness of 40 nm would therefore be unfavorable for spintronics devices as Bloch walls create out-of-plane pinning sites in an in-plane magnetized sample.

Since magnetoresistance measurements of CNT-based devices are typically performed at cryogenic temperatures in order to ensure a strong tunnel barrier at the

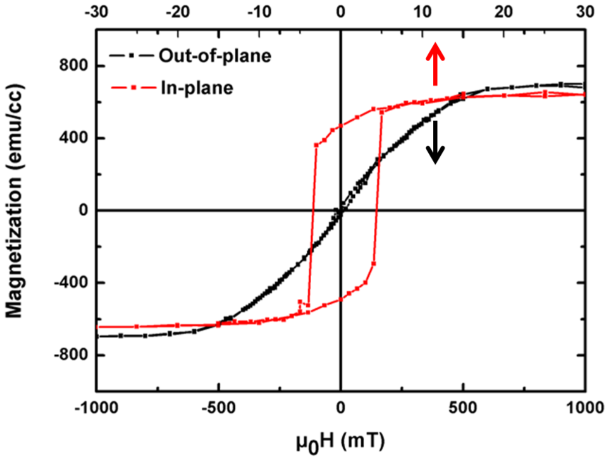

Figure 4.5: Room temperature SQUID data for a 20 nm thick $Co_{50}Pd_{50}$ film showing in-plane (red) and out-of-plane (black) components of magnetization.

interface of the contacts to the CNT, SQUID data at 4 K is recorded for the 40 nm thick $Co_{50}Pd_{50}$ film. A comparison of room temperature and low temperature data is shown in figure 4.6. As expected, the thin film exhibited a hysteresis curve that is wider and more square at T=4 K than at T=300 K. This is an expected result, as larger coercivity can be assigned to larger anisotropy values for lower temperatures, and thermally enhanced domain wall motion leads to bending of the loop with increasing temperature. The decrease in saturation magnetization with temperature is a further indication that anisotropy values are temperature-dependent [40].

4.2 Nanostructures

Above, it is shown that increasing the Co content and decreasing the thickness of a film ensures a high in-plane magnetization component. In order to further eliminate the effects of bubble domains and accurately study material characteristics for application, $Co_{50}Pd_{50}$ oval-shaped nanostructures resembling contacts were fabricated with dimensions 2 μm × 150 or 400 nm, and thicknesses of 20 or 40 nm. Fabrication was done via a standard lift-off technique described in chapter 3 and in the appendix. Since one nanostructure consists of a tiny amount of material, 3×3 mm^2 arrays, consisting of approximately two million nanocontacts, were fabricated to en-

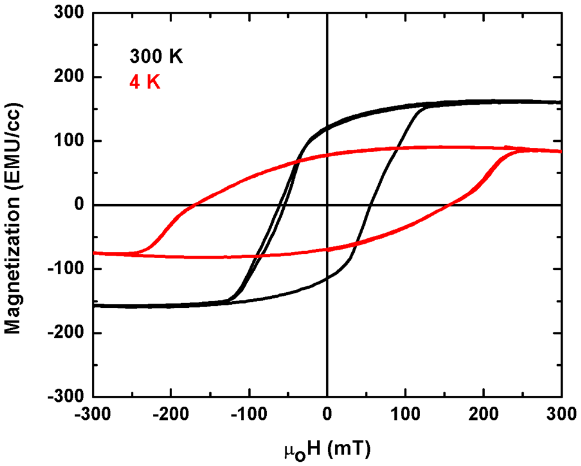

Figure 4.6: Room temperature (black) and 4 K (red) SQUID data of a 40 nm thick $Co_{50}Pd_{50}$ film. Data was recorded for in-plane magnetization.

sure the magnetic signal was high enough to accurately measure via SQUID. The spacing between structures was 1 μm in each direction, as this is larger than the distance expected to eliminate stray field effects between the magnetic structures, which was shown to be 500 nm for similar systems [5]. Note: the structures were uncapped. As a result, when performing low-temperature measurements, a small exchange bias (on the order of 5 mT) was sometimes present due to the formation of an antiferromagnetic native oxide, and has been subtracted in all data presented here.

4.2.1 Structure design

When designing the size and shape of nanostructured contacts, the first consideration was the size of the domains formed in extended films, as seen via MFM in figure 4.3. The dimensions of the contacts were chosen such that they ideally encompass only one magnetic domain. The widths of 150 and 400 nm were chosen as they are expected to result in a clear difference in coercive field H_c. Finally, the geometry of the contacts was considered. Typical rectangular shaped contacts often exhibit end domains which inhibit switching and could pose a challenge in a material that already shows a complicated magnetic behavior. By smoothing the edges and forming oval-shaped contacts, the issue should be avoided. However, the exact effect on the magnetization of the sample was unknown.

Simulations were performed using the Object Oriented Micro Magnetic Framework (OOMMF) software, developped at NIST [83]. OOMMF works to solve the micromagnetic structure of a given object based on the Landau-Lifshitz-Gilbert equation:

$$\frac{\delta M}{\delta t} = -\gamma m \times H_{eff} + \alpha m \times \frac{\delta m}{\delta t} \tag{4.1}$$

where M is the magnetization of the sample based on the saturation magnetization, γ is the gyromagnetic ratio of a material, H_{eff} is the effective field accounting for external field and demagnetization field within the sample, m is the magnetization at a given point, and α is a constant used to obtain a material-specific damping factor. This damping coefficient is usually between 0.01 and 0.5, with a lower coefficient increasing the time it takes for a material to fully relax. Most metals are accurately simulated with a damping coefficient of approximately 0.2.

The shape of the object can be implemented into the simulation, and a magnetic field sweep can be performed, with data points taken at various values. Additionally, several material parameters must be given, such as the anisotropy direction, anisotropy constant, and saturation magnetization. These values are very well known for the 3-D transition elements, but not for alloys.

In order to determine appropriate values for the material parameters of $\text{Co}_{50}\text{Pd}_{50}$, SQUID measurements were performed on arrays of both $\text{Co}_{50}\text{Pd}_{50}$ and Co nanocontacts. Figure 4.7 compares the magnetization at 4 K of an array of oval-shaped 20-nm thick Co and $\text{Co}_{50}\text{Pd}_{50}$ nanocontacts with dimensions 2 μ m × 400 nm. The hysteresis loop of the Co array exhibits a significantly higher saturation magnetization, almost twice that of $\text{Co}_{50}\text{Pd}_{50}$, as well as a higher coercive field, which is roughly expected, as twice the amount of ferromagnetic cobalt is present. Based on the ratio of saturation magnetization between the two materials, we were able to determine the approximate values for the saturation magnetization and anisotropy constant of the $\text{Co}_{50}\text{Pd}_{50}$ objects in our simulation as being $\text{M}_s = 7 \times 10^5$ A/m and $\text{K1} = 260 \times 10^3$ J/m^3, respectively. From our knowledge of the crystal structure of CoPd, we were also able to define the magnetocrystalline anisotropy as being based on a cubic system. With these parameters, it was possible to perform OOMMF simulations of CoPd structures.

Figure 4.8 shows the result of OOMMF simulations on a set of rectangular (top) and oval (below) contacts. The geometries and proximities of the contacts are designed to resemble an actual device. In both simulations, the contacts are saturated

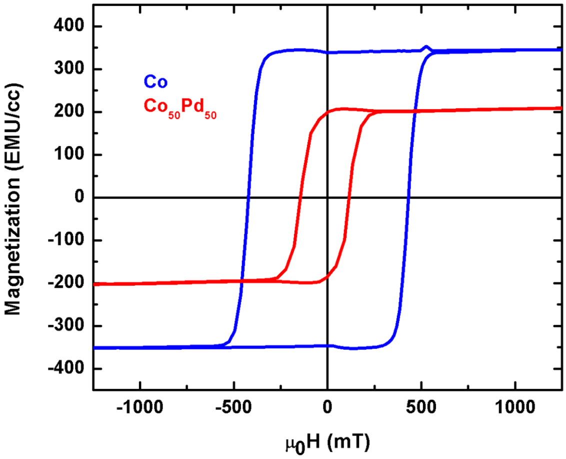

Figure 4.7: Comparison of the the in-plane magnetization behavior at 4 K of an array of 20-nm thick 400 nm wide Co (blue) and $Co_{50}Pd_{50}$ nanostructured ovals.

with a positive field to have a single magnetic domain (red). The contacts maintain their polarization throughout an external field sweep until reaching a field of approximately -50 mT, at which point they begin to flip their polarization to the opposite (blue) sign. In the case of rectangular contacts, the contacts are shown to develop edge domains, as well as closure domains. As a result, the contacts aren't fully polarized until a field of -80 mT is reached. On the other hand, oval-shaped contacts are shown to form fewer edge domains, reaching saturation in the negative (blue) direction at a field of approximately -67.5 mT. Edge domains are especially critical in CNT-based devices, which are typically fabricated with the nanotube at the end of the contacts, directly under the potential edge domain. In both simulations, a white color is equivalent to an out-of plane magnetization (i.e. domain walls). Based on the results of these and subsequent OOMMF simulations, it was decided to fabricate oval-shaped CoPd contacts throughout this work.

4.2.2 Room temperature magnetic behavior of CoPd nanostructures

Magnetic characterization was then performed on CoPd samples designed with oval-shaped contacts. Figure 4.9(a) shows an MFM image of 20-nm thick, 2 μm × 400

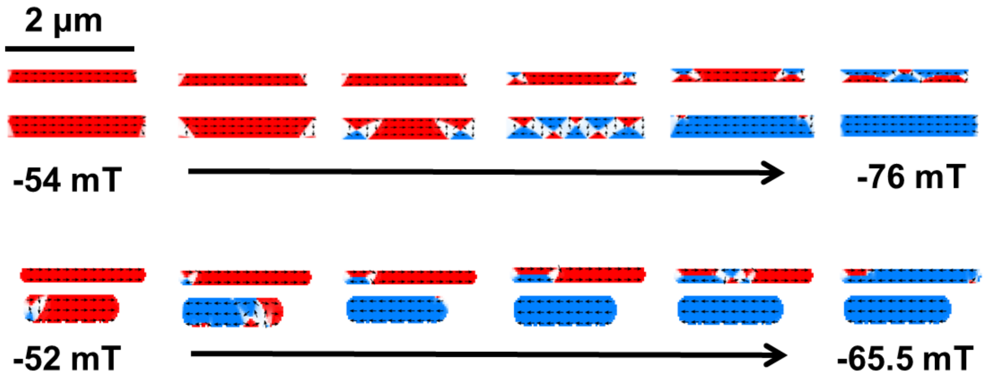

Figure 4.8: Object oriented micromagnetic framework simulation of the magnetization of rectangular (above) and oval (below) CoPd contacts. Oval contacts were shown to minimize the effects of end domains. Blue and red represent spin left and spin right domains, respectively, while white is intermediate. In order to focus on the intermediate magnetization, the fully saturated states are not shown.

nm CoPd contacts, fabricated in an array for SQUID measurements. Prior to the measurement, the sample was magnetized to saturation with a field pointing along the long axis of the structures. When the sample is measured in a remanent state, two domains are observed along the lateral direction. There is no sign of bubble or stripe domains, as in the case of a thin film.

Figure 4.9(b) shows the result of slightly changing the geometry of the contacts. In this case, a four-terminal device with CoPd contacts was imaged rather than a SQUID array. The contacts have varying widths, but both the length ($l = 4\ \mu$m) and the thickness ($t = 40$ nm) are greater than those of the individual nanocontacts in the SQUID array. The formation of multiple domains suggests a strong component of magnetization in the out-of-plane direction. It should be noted however, that the structure resembles closure domains, rather than randomly aligned bubble domains, indicating a higher remanent magnetization in the contacts than in the films despite the emergence of an out-of-plane component. Another consideration is that an in-plane component perpendicular to the long axis of the contact would also result in a complicated magnetic structure, and has been observed in similar material systems [26, 27]. Such a magnetic structure would result in a high, potentially unstable coercive field in a quasi-spin valve; therefore, the contact dimensions chosen for devices were kept to the range of those in the SQUID array. In both MFM images

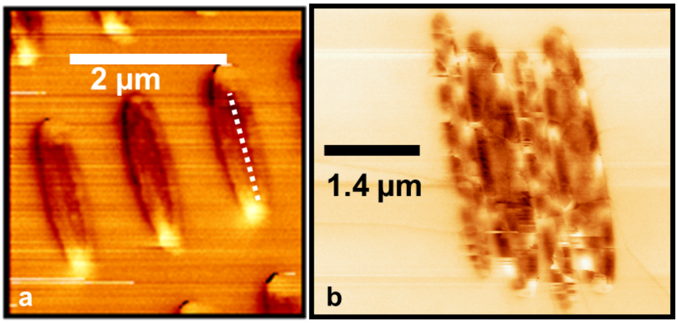

Figure 4.9: MFM images of (a) an array of 20-nm thick CoPd contacts, with the dotted line indicating what appears to be a Néel wall and (b) a sample with 40 nm thick contacts, show the formation of Bloch walls beginning at a thickness between 20-40 nm.

(a) and (b), areas of slight roughness are attributed to thermal cycling before the MFM measurement was performed.

In-plane and out-of-plane SQUID magnetization measurements were performed on the arrays, with results summarized in figure 4.10. The arrays involved different quantities of $Co_{50}Pd_{50}$, which influences the measured saturation magnetization recorded. In order to make valid comparisons, all data is therefore discussed in terms of magnetization density. Differences in saturation magnetization are partly the result of background fitting to remove the diamagnetic and paramagnetic signal coming from the substrate. In-plane measurements in figure 4.10(a) indicate that in the nanocontact arrays, the coercive field $\mu_0 H_c = 60$ mT for both of the 150 nm structures (red and blue), and $\mu_0 H_c = 25$ mT for the 400 nm wide structures (black). Such a reduced coercive field is expected due to the lower shape anisotropy of the wider contacts. In contrast to the thin films, the thickness no longer appears to influence the coercive field, as there is likely no longer enough material per contact to form multiple domains with pinning sites at Bloch walls.

Out-of-plane measurements are plotted in figure 4.10(b). The 20 nm thick wider contact array (black) has a very slight out-of-plane component, likely due to the non-single domain structure observed in MFM and shown in figure 4.9(a). The 40 nm thick narrow contacts show only a small out-of-plane component to the magnetization (blue), and for the 20-nm thick narrow contact (red), the remanent magnetization is zero, indicating a completely in-plane magnetization. The out-of-plane component in the wider contacts, which was absent in 20 nm thin films, is likely due to the decreased shape anisotropy of the system. Along with the MFM images, this data confirms that the bubble domains have indeed disappeared, leaving only

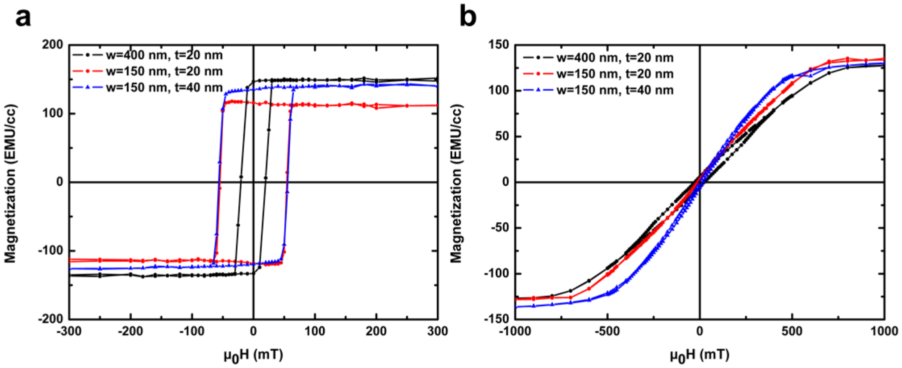

Figure 4.10: Room-temperature SQUID magnetization data for CoPd contact arrays with varying geometries (marked as black, red and blue). Magnetization is shown to be predominantly in-plane, and to be strongly influenced by contact width.

one domain wall in the wider contacts. Such contacts used in a FM-CNT-FM device would be expected to show stable switches in resistance when exposed to an in-plane magnetic field sweep, as the coercivity of the magnetic structures will be reproducible and the devices exhibit square in-plane hysteresis loops. The reproducibility comes from the fact that the switching mechanism will be originated by the nucleation sites already determined by the geometry and not in random sites like in the case of bubble domains.

4.2.3 Temperature dependence of magnetic behavior in CoPd nanostructures

The measurements were then repeated at 4 K, to simulate the behavior of contacts when exposed to measurement conditions. A comparison of SQUID magnetization curves at 300 K and 4 K is presented in figure 4.11 for a (a) wide and (b) narrow contact array of thickness $t = 20$ nm. It is observed that the scaling of coercive field with respect to contact width holds true at 4 K, indicating the continued prevalence of shape anisotropy. Furthermore, a small exchange bias develops, which appears most strongly in (b), due to the formation of native oxide on the uncapped CoPd. This was again done to similate device parameters. Several samples were fabricated with no gold capping layer, which has previously been shown to inhibit spin injection if the gold touches the CNT at the sides of the contact, bypassing the FM [77].

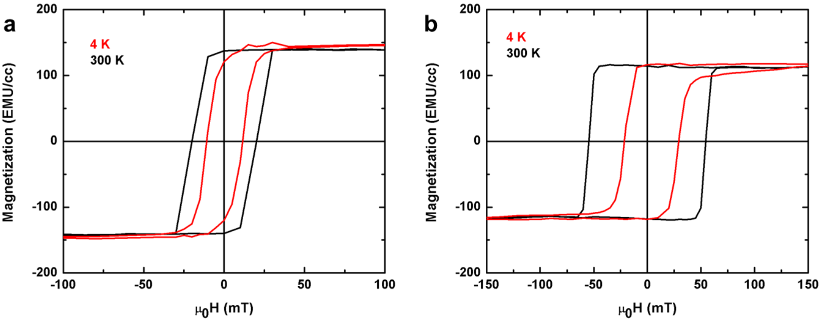

Figure 4.11: Room-temperature (black) vs. 4 K (red) SQUID magnetization data for CoPd contact arrays representing (a) wide and (b) narrow contacts. In both cases, the coercive field is smaller at 4 K than at 300 K.

The measurements at 4 K (red) yielded an unexpected result in that they exhibited smaller coercive fields than those at 300 K (black). In the case of the wider array in (a), the remanent magnetization was also significantly reduced. This result is specific to the nanopatterned sample, and indicates the presence of a new contribution to the anisotropy. In order to pinpoint the cause, in-plane magnetization was recorded at a series of intermediate temperatures, as summarized in figure 4.12.

Figure 4.12(a) plots three representative curves, showing magnetization at 300 K (black), 4 K (red), and the additional intermediate temperature 50 K (blue). Slight differences in the values with respect to those in figure 4.11 occur, as this measurement was performed in a different magnetometer with newly fabricated samples. The data reveals that at room temperature, the hysteresis is fairly wide and square. This would be favorable for spintronics devices, as squareness corresponds to abruptness of switching. At intermediate temperatures however, the hysteresis is significantly less square and has a significantly smaller coercive field. At $T = 4$ K, the shape of the hysteresis returns to a similar shape as the original room temperature curve, although still with a slightly lower coercive field. The coercive field versus temperature for all measurements performed is shown in figure 4.12(b), showing an initial sharp decrease in coercive field with respect to temperature, followed by a gradual increase.

Table 4.1 is a complete list of the coercive field and the remanent magnetization of the sample measured at various temperatures between 4 and 300 K. It is clearly seen that as the temperature is lowered, both coercive field and remanent magnetization experience an initial decrease, before beginning to rise as expected. The minimum

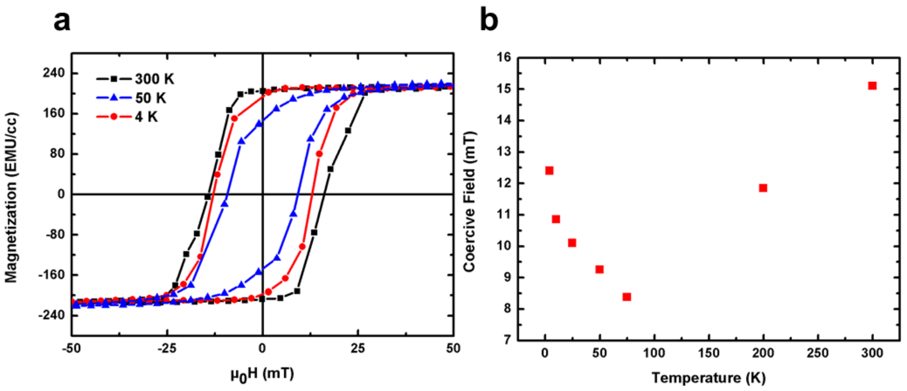

Figure 4.12: Temperature-dependent SQUID measurements for in-plane magnetization of an array of wide-contact CoPd structures showing (a) the evolution of the magnetization curve between 300 K (black), 50 K (blue), and 4 K (red). The coercive field values for a wider range of measurements is plotted in (b). Data has undergone removal of a paramagnetic background and exchange bias, but has not been normalized.

values appear at 75 K and 50 K for H_c and M_r, respectively. The values given here are averages over at least 3 measurements on two samples, all of which showed consistent results.

In order to explain the unexpected magnetic behavior of the CoPd nanocontacts, we consider the changing energy balance in our sample during magnetization and temperature sweeps. Contributions to the total energy of the system include Zeeman energy, exchange interaction, dipole interactions, and anisotropy. While the effects of the first two are relatively temperature independent, magnetic anisotropies can vary strongly with temperature. However, the magnetocrystalline anisotropy constant, which is normally the highest anisotropy contribution to the total energy, and the shape anisotropy constant, which arises from dipolar interactions, vary with the temperature with respect to a change in saturation magnetization, which tends to increase with lowering temperature for many systems. Equations 4.2 and 4.3 show the relationship between shape and magnetocrystalline anisotropy and temperature, showing the high dependency on saturation magnetization. Equation 4.2 is the form of an in-plane shape anisotropy but its dependence on the square of the magnetization is quite general independent of the actual form of the shape anisotropy. Equation 4.3 is the equation for the temperature dependence of the cubic anisotropy from the Callen-Callen theory [84]. However, in figure 4.12, it is observed that the saturation magnetization of the CoPd nanoarrays is quite constant when measured

Table 4.1: Temperature dependence of coercive field and remanent magnetization of a $Co_{50}Pd_{50}$ nanoarray. Saturation magnetization is not shown here, as it remained constant for all temperatures measured.

Temperature (K)	$\mu_0 H_c$ (mT)	M_r (EMU/cc)
300	151	204.2
200	118.5	185.7
75	83.5	144.8
50	92.5	139.3
25	101	142.9
10	108.5	164.3
4	124	181.0

at various temperatures. Therefore, additional contributions to the anisotropy are needed to explain the observed coercivities.

$$K_{\mathrm{sh}}(T) = -\frac{\mu_0 M_s(T)^2}{2} \tag{4.2}$$

$$K_{\mathrm{mc}}(T) = K_{\mathrm{mc}}(0\ \mathrm{K}) \left(\frac{M_s(T)}{M_s(0\ \mathrm{K})} \right)^{10} \tag{4.3}$$

A further contribution to the anisotropy energy of the system comes from inverse magnetostriction, or magnetoelastic anisotropy, where the sample acquires mechanical strain due to lattice mismatch or a structural phase transition, and the magnetization alters slightly in order to best reduce that strain. Due to thermal expansion and/or phase changes, this effect is highly temperature-dependent. Furthermore, a magnetoelastic effect has been previously observed in CoPd thin films, although predominantly for alloys with a lower Co content [28]. It has also been shown that particles and noncontinuous films are more strongly effected than thin films due to a more complex strain system [28], which is likely to also be the case for nanostructures.

A schematic representation of the the layer system in the contacts is presented in figure 4.13. The first interface, between the silicon substrate and the thermally grown SiO_2, which is shown for thoroughness, is unlikely a cause for strain, as both materials have low thermal expansion coefficients, on the order of 2.6×10^{-6} /K.

The next interface is between the amorphous SiO_2 and the CoPd alloy. As the substrate is an amorphous oxide, it is unlikely that the CoPd forms continuous bonds to it. Rather, bonds would form in random positions, which could later change to

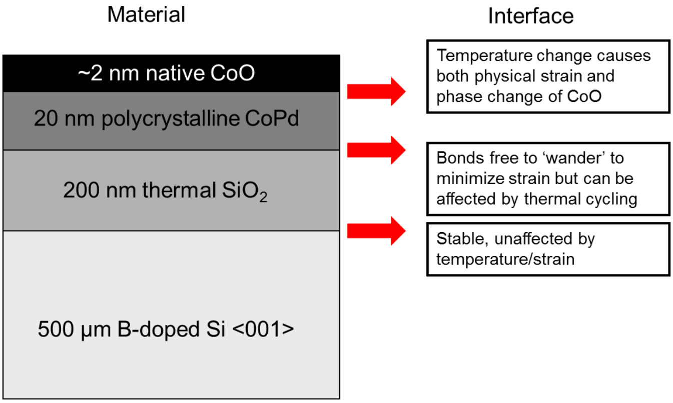
Material
Interface
~2 nm native CoO
20 nm polycrystalline CoPd
200 nm thermal SiO2
500 µm B-doped Si <001>
Temperature change causes both physical strain and phase change of CoO
Bonds free to 'wander' to minimize strain but can be affected by thermal cycling
Stable, unaffected by temperature/strain

Figure 4.13: A schematic side-view of the layered system of an uncapped CoPd sample. Exploring the various interfaces can pinpoint possible causes for the complicated magnetic behavior observed in SQUID data.

accommodate for a strain in the system. It is therefore unsure whether temperature variations affect the strain at the gate oxide-CoPd interface. However, it must be considered that the coefficient of thermal expansion for CoPd which is calculated to be 11.1 $\times 10^{-6}$ /K [85], is significantly larger than that of the substrate. Despite the noncontinuous bonding, this could result in a large strain at low temperatures, especially after the effects of multiple thermal cycles, especially if the roughness of the metal increases during cooling[86]. The presence of strain in the nanopatterned array and not the film could then be the result of internal strain enhanced by the fabrication/thermally-induced geometrical constriction.

A final interface to consider is that where the native cobalt oxide layer forms at the surface of CoPd. The common oxide, CoO is an antiferromagnet with a high Néel temperature of approximately 270 K. However, since our sample is exposed to atmospheric conditions in the course of the various experiments, the formation of some Co_3O_4, also an antiferromagnet, is expected as well. The presence of Co_3O_4 is indicated by an exchange bias in the hysteresis loops of the samples, when measured at temperatures below 50 K. The exchange-bias induced shift in coercive field is approximately -15 mT, and has been removed in figure 4.12 in order to more clearly focus on the change of hysteresis shape with respect to temperature. A comparable exchange bias is observed in measurements on thin films, although since the shape anisotropy and surface-to-volume ratio are highly reduced with respect to those of the nanocontacts, any strain effects resulting from the oxide play a less visible role. Co_3O_4 exhibits a phase change from a spinel structure to an ordered magnetic system at its Néel temperature of around 40 K [44].

As the temperature initially begins to lower, it is expected that the strain between the CoPd nanocontacts and the native oxide will begin to change. The (111) surface of CoPd has a lattice size of approximately 6.5 Å at room temperature, and a coefficient of thermal expansion of approximately $11.1 \times 10^{-6}\ /K$. The cobalt oxide has a much larger lattice constant of approximately 8.1 Å, indicating an initial strain on the system. As the temperature is lowered, the oxide lattice constant is expected to decrease in size at $9.3 \times 10^{-6}\ /K$, a slower rate than the CoPd, changing the strain and introducing magnetoelastic anisotropy into the system. At approximately $T = 40$ K, the oxide will become both cubic and antiferromagnetic, introducing both a change in strain, and an exchange bias into the sample, which will strongly effect the energy in the system. The observed minima of H_c and M_r around $T = 50$ K correspond well to this change, and SQUID data strongly implies that the strain system at $T = 4$ K helps to return the sample to the preferred in-plane magnetization. The CoPd-Co_3O_4 interface is therefore highly likely to induce strain in the system. Anisotropy effects from the oxide layer would be much more prevalent in the nanoarrays than the films, as the surface-to-volume ratio is greatly increased.

Changes in magnetic anisotropy, specifically magnetoelastic anisotropy, are therefore predicted to alter the micromagnetism of our sample in a way that clearly matches the temperature-dependent behavior we measure via SQUID. This indicates that while CoPd nanocontacts have a complicated strain system at higher temperatures, at $T \leq T_{Néel}$ Co_3O_4, structural changes allow for the creation of an in-plane magnetic system with a wide, dependable coercive field. This makes CoPd nanocontacts ideal for low-temperature magnetotransport applications, as well as having an interesting, non-negligible impact in the case of temperature-dependent magnetoresistance measurements. It should be included that in the case of in-situ capped contacts, some native oxide would still be expected to form at the sides of the contacts. Therefore, whether the substrate-metal interface, or the contact-oxide interface, or both, make the largest contribution to the magnetoelastic coupling found in the contacts, the effect is also relevant in capped structures.

4.2.4 Magnetoelastic effect

In addition to the out-of-plane component of magnetization, which is largely nonexistent for the nanoarray structures, it must be considered that the strong anisotropy from the magnetoelastic effect can lead to unexpected in-plane anisotropies. For the NiPd system, there is a strong anisotropy favoring magnetization in-plane transverse to the contact direction [26, 27]. This is unexpected, due to shape anisotropy, and has been attributed to a dominating magnetoelastic coupling in the system due to strain between the substrate and the contacts during thermal cycling. Furthermore, the effect is so strong that magnetotransport measurements were only successful in the case of a field sweep along the transverse (short) axis of the contacts. In the interest of obtaining high quality magnetotransport, it is therefore necessary to determine to what extent this effect is present in the CoPd contacts.

First, the material was tested for anisotropic magnetoresistance (AMR). In this measurement, a bias is applied to a material, and a magnetic field is applied in various directions. As spontaneous magnetization occurs along the easy axis of a material, the resistance will exhibit the smallest change in this direction, whereas in the case of a hard or intermediate axis, the moments will align as a field is applied, resulting in a change in resistance [27, 87]. AMR measurements were performed on a bar of CoPd with dimensions 1.4 × 0.4 mm and thickness $t = 60$ nm. This thickness induces an out-of-plane component to the magnetization that is neglected here, in order to focus on in-plane anisotropy. The in-plane dimensions were chosen to maintain the ratio used to obtain shape anisotropy in contacts, and the thickness was chosen in order to be able to bond directly onto the CoPd bar without the use of gold contacts, which were shown to negatively influence transport [88]. The AMR value in CoPd is also useful to consider when determining possible spurious effects contributing to the magnetoresistance observed in transport measurements, and will be revisited in chapter 7.

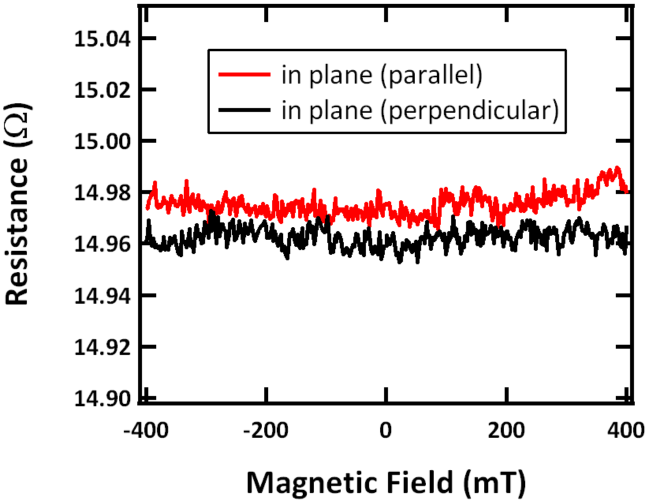

Figure 4.14: AMR measurements of CoPd stripes with a field sweep in the directions in-plane longitudinal and transverse to the long axis of the contact with 1 mV bias indicating no AMR. Measurements were performed at 4 K. Measurement from reference [88].

Results from AMR measurements in the in-plane directions parallel and transverse to the long axis of the stripe are shown in figure 4.14. The measurements were taken at 4 K while applying a constant bias of 1 mV. This represents a bias within the range used in magnetotransport measurements, although the resistance in CNT-based devices is several orders of magnitude higher. Approximately zero AMR is measured for either in-plane direction, which corresponds well to established results on permalloy contacts [87]. This indicates that AMR should have no influence on transport. However, it doesn't confirm a preferred magnetic orientation due to shape anisotropy, and further study is required.

Next, an array of CoPd ovals of dimensions 2 μm × 400 nm × 20 nm was studied via SQUID magnetometry. Room-temperature measurements were performed with the magnetic field in-plane parallel to and transverse to the long axes of the contacts. The results are shown in figure 4.15. Data has been normalized to more easily compare the shape of the curves. It is clearly seen that the magnetic easy axis occurs in the direction parallel to the long axes of the contacts (blue), while a hard or intermediate axis exists in the transverse direction (red).

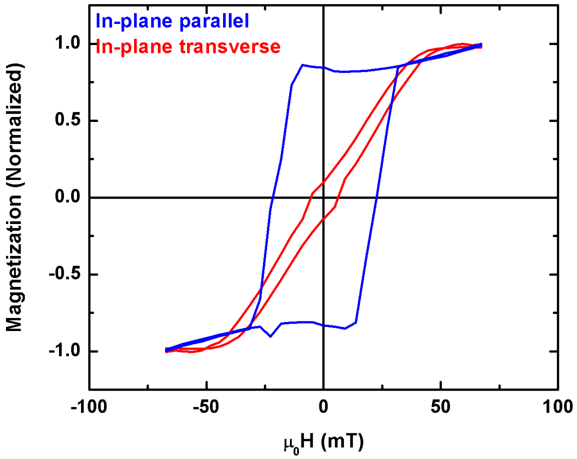

Figure 4.15: SQUID magnetization measurements of an array of CoPd contacts with field applied in-plane parallel (blue) and transverse (red) indicates an easy-axis in the in-plane direction perpendicular to the long axis of the contact. Data has been normalized and a diamagnetic background has been removed.

The conclusion of this study is that CoPd does not exhibit the same strong preferential easy axis transverse to the contact axis observed in NiPd. This could be the result, for example, of a higher polarization favoring less domain formation, a higher shape anisotropy, or slightly less strain induced in the system. Another consideration is that the aspect ratio, especially the lateral dimension of the contacts studied in this work is significantly smaller than those investigated for NiPd, leading to a lower internal lateral strain in our structures [27]. A small magnetization component along the in-plane transverse axis is present, but is not dominant enough to prevent a clear magnetoresistance measurement with a field sweep in-plane parallel to the long axis of the contacts.

4.3 Electronic interface with CNTs

Until now, this chapter has focused on obtaining a contact material with low roughness and high magnetization, neglecting the fact that a good electronic interface with CNTs is crucial for obtaining effective spin injection and detection. While transport in CoPd-CNT-CoPd devices will be primarily discussed in chapter 7, the characterization of CoPd as a contact material would not be complete without a brief electronic characterization.

Figure 4.16 shows the I-V characteristics of a typical device measured at room temperature in a probe station (a) and at 4 K in a flow cryostat (b). The device shown here appears to include a metallic nanotube with a low ohmic resistance of approximately 30 kΩ at room temperature. As CVD growth is a statistical process, the chirality and diameter of CNTs, and therefore their electronic properties, vary strongly. This device is an accurate representation of a typical device where CNT growth is performed at high temperatures, creating large diameter double or multiwalled CNTs, where the likelihood of at least one wall being chirally metallic or semimetallic is high. When the device is cooled to 4 K, the I-V characteristics are no longer linear, indicating the formation of a small potential barrier. Since spin injection in FM-CNT-FM devices is thought to be caused by tunneling magnetoresistance (TMR) [21], the formation of a barrier, thought to be related to the opening of a stress-induced band-gap [66] in a metallic CNT, strongly influences spin transport. Alternatively, the low-temperature measurement could indicate the presence of a semi-metallic nanotube with a small band gap overcome by thermal energy at room temperature. The data remained constant over multiple thermal cycles and current sweeps. These findings indicate that $Co_{50}Pd_{50}$ is indeed capable of forming an ideal electronic interface to CNTs comprising of a stable, low-ohmic contact with an intrinsic tunnel barrier at low temperatures.

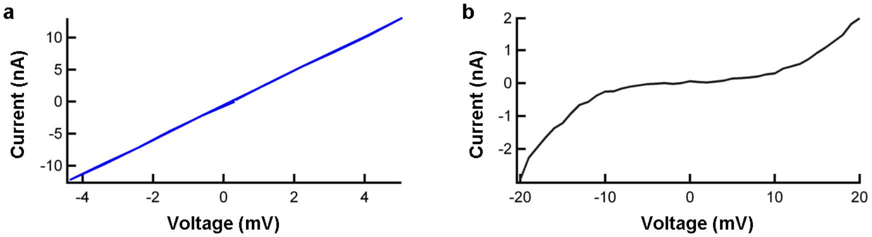

Figure 4.16: I-V characteristics of a CoPd-contacted (semi)metallic CNT device (a) at room temperature and (b) at 4 K.

4.4 Conclusions

In conclusion, a thorough characterization of CoPd thin film alloys of varying composition and thickness indicates that thin, Co-rich films have a primarily in-plane magnetization, but a complicated magnetic structure. Restricting the geometry of the material by fabricating nanostructures results in a quasi single-domain magnetic behavior. A strong anisotropy influence from the magnetoelastic effect leads to unexpected temperature-dependent magnetization of nanostructures, however at 4 K, where transport measurements are performed, the nanostructures have high in-plane saturation and remanence magnetization, and a coercive field that is controllable by shape anisotropy, although susceptible to an additional anisotropy from the magneto-elastic effect. The additional anisotropy in CoPd nanostructures is also present in similar NiPd nanocontacts. Unlike NiPd, however, CoPd maintains an easy axis in-plane parallel to the long axis of the contacts at 4 K, which is an imporant parameter to consider for magnetotransport measurements. Results also show that CoPd has a low interface roughness and good ohmic contact to CNTs. Taken together, these findings indicate that when the appropriate geometry is used, $Co_{50}Pd_{50}$ is a promising contact material for application in CNT-based quasi spin-valve devices.

5 Electronic configurations and models

At the border of magnetism and transport, both the applied magnetic field and the electronic configuration with which a measurement is performed determines which physical effects are being measured. In this work, the magnetic field was predominantly applied in-plane to the sample, along the long axis of the FM contacts, and fields of 500 mT or less were required to saturate the FM contacts. Electronically, however, both local and nonlocal configurations were used. In the local configuration, which corresponds to a two-terminal measurement in a lateral quasi-spin valve, voltage was applied and current was measured (or the reverse) via the same electrodes. Therefore, although the electrons may have a preferred polarization, there is no clear separation between electronic and spin current, and it is difficult to determine which parts of the measured signal are the result of spin current only, and which are due to ohmic effects. Such a situation where charge (Q) and spin (s) are both transported may be defined by:

$$\frac{\delta Q}{\delta t} \neq 0 \qquad and \qquad \frac{\delta \vec{s}}{\delta t} \neq 0 \tag{5.1}$$

in contrast to purely electrical current, where $\frac{\delta \vec{s}}{\delta t} = 0$.

In order to more clearly determine the effect of spin accumulation, nonlocal measurements were attempted. Nonlocal measurements were performed in a configuration in which a polarized current was injected along between two electrodes and detected in a location outside of this direct path. Signal detection becomes much more challenging in this setup, due to both fabrication factors and the nature of the signal. However, nonlocal measurements allow for the detection of a pure spin current with no spurious effects resulting from ohmic contributions. Such a situation may be described by:

$$\frac{\delta Q}{\delta t} = 0 \qquad and \qquad \frac{\delta \vec{s}}{\delta t} \neq 0 \tag{5.2}$$

The mechanisms behind such a measurement will be discussed in more detail below.

This chapter describes local and nonlocal configurations specifically for CNT-based devices used in this work, and discusses in which case each setup was used, with the ultimate aim of measuring TMR and determining spin coherence in carbon nanotubes.

5.1 Local measurements

As described in chapter 2, tunneling magnetoresistance relies on a spin-dependent tunneling process in which spin is conserved. TMR was first reported by Jullière in 1975, with a simple model to describe TMR in a magneto tunnel junction (MTJ) system based on transition metal ferromagnets (FM) separated by a nonmagnetic layer and a tunnel barrier. In his model, Jullière assumed a two current model, based on that of Mott [49], in which spin up and spin down electrons form separate current channels, the sum of which equals the overall current of the system. Consequently, the model is only valid in the case that the size of the nonmagnetic layer is less than the spin flip length λ in the material. Figure 5.1 depicts the spin-dependent tunneling described in the model. When the two ferromagnetic layers are aligned in parallel, majority carriers from the first FM layer tunnel into the majority band of the second FM layer. The tunneling process has a relatively low resistance, as the same number of states are available to majority and minority carriers in each electrode.

When the layers are in the antiparallel configuration, as depicted in figure 5.1(b), the majority carriers (spin up in this case) tunnel into the minority band of the second layer, and reverse. There are therefore a different number of available states for each spin-split band in the injecting and detecting layers, resulting in a higher overall resistance.

From this, it may be determined that the tunneling resistance is directly related to the spin-split density of states of each electrode at the Fermi level:

$$R_P \propto \frac{V}{N_1^{\uparrow}N_2^{\uparrow} + N_1^{\downarrow}N_2^{\downarrow}} \tag{5.3}$$

$$R_{AP} \propto \frac{V}{N_1^{\uparrow}N_2^{\downarrow} + N_1^{\downarrow}N_2^{\uparrow}} \tag{5.4}$$

Figure 5.2 illustrates via a resistance diagram how the Jullière model equates to a lateral CNT-based spin valve with FM contacts rather than layers. Tunnel barriers

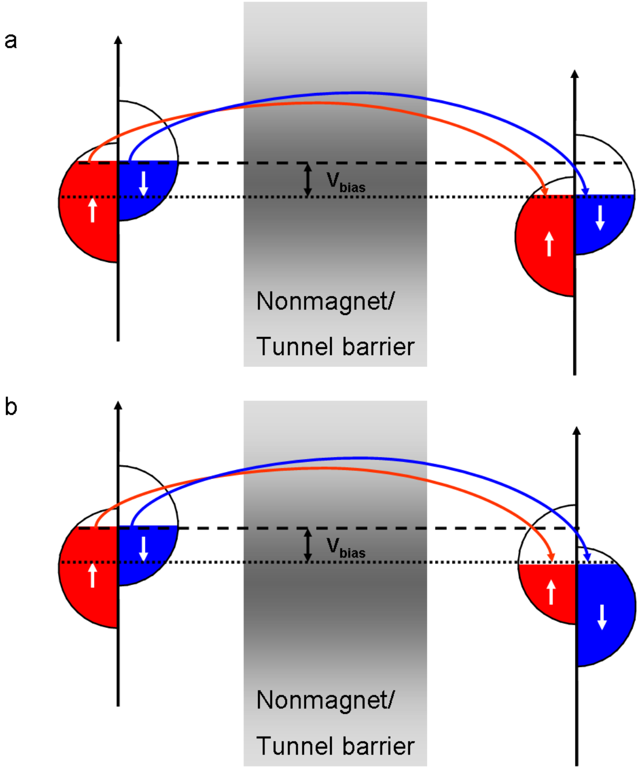

Figure 5.1: Two-current tunneling process for spin up and spin down electrons, as given by the Jullière model for (a) parallel and (b) antiparallel alignment of two magnetic layers separated by a tunnel barrier.

are neglected in this explanation, as they have a constant high resistance contribution. When the two contacts are aligned parallel in the spin up direction, the resistance for the injected spin-up electrons, which dominates transport, is low. The resistance states in (a) would also apply in the case of both contacts having spin down polarization. In the case of the injector and detector being aligned antiparallel (b), the resistance is higher. Therefore, as in the case of Jullière's MTJ, local magnetoresistance measurements tend to result in an increased resistance in the antiparallel configuration.

Figure 5.3 depicts a typical device for performing local measurements, comprising a CNT contacted by two ferromagnetic leads. The contact materials used in this work have been thoroughly characterized, and an optimal geometry is used for all

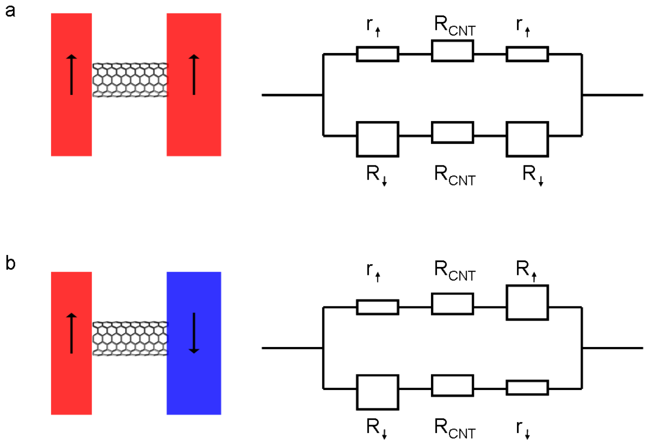

Figure 5.2: Model of the resistance levels of spin up and spin down current channels in a 2-terminal CNT-based device for (a) parallel and (b) antiparallel contact alignment. The resistance levels in (a) would be equal but reversed in the case of parallel spin down polarization.

samples, as discussed in chapter 4, in order to use shape anisotropy to control the coercive fields of the contacts. The TMR value is calculated by:

$$TMR = \frac{\Delta R}{R_{\text{parallel}}} \cdot 100\% \tag{5.5}$$

Note: throughout this thesis, when a sloping or uneven background is observed, $R_{parallel}$ is considered to be an average of the values. In the Jullière model, [13] %TMR may also be written in terms of polarization of the two ferromagnetic contacts:

$$TMR = \frac{2P_1P_2}{1+P_1P_2} \cdot 100\% \tag{5.6}$$

which in turn depends on the density of states of spin up and spin down electrons at the Fermi level as described in equation 1.1.

Using the simplified picture described above, it may be understood that positive MR is observed in a local spin valve measurement, and an ideal local TMR signal is shown in figure 2.9. It is possible, however, to electrically tune a device in order to obtain negative MR in a local configuration. This may be done, for example, by changing

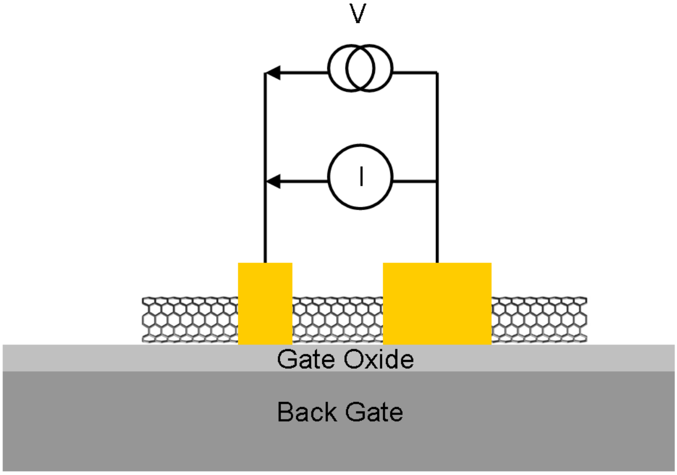

Figure 5.3: Schematic of a typical CNT-based device in a local measurement setup. The same two contacts are used both to apply voltage(current) and measure current(voltage). The substrate is highly doped and may be used as a backgate in order to electronically influence transport.

the polarization at only one electrode [89]. Furthermore, it has been shown that by adjusting the gate voltage, the tunnel barriers formed at low temperatures between the CNT and the contacts can be tuned, leading to suppression or enhancement of TMR, and even leading to a negative TMR at certain values [25]. This latter method offers more control, and is therefore more interesting for application purposes.

According to the simple model presented by Jullière, there should be a maximum TMR of $\Delta R = 14\%$. However, when Jullière published this result, several material systems had already been shown to exceed this prediction. For example, a 26% TMR had been observed in Fe-Al junctions[90]. This was attributed to magnetic coupling between ferromagnetic films and second order conductance phenomena [13]. More recently, high TMR values of 60% and 100% have been observed for CNT-based devices contacted with LSMO [91] and Co [3], respectively. In the latter case, the high TMR was attributed to cotunneling processes occurring at temperatures of T = 1.2 K.

Furthermore, although it was an important first step in understanding TMR, the Jullière model assumes that TMR is determined via the polarization of the ferromagnetic layer/contacts. In an important new finding in 1989, Slonczewski showed that the height of the tunnel barrier can also influence TMR [92]. The Slonczewski

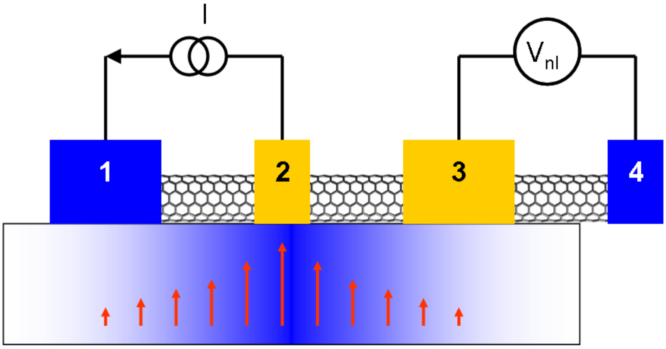

Figure 5.4: Schematic of a typical CNT-based device in a nonlocal measurement configuration. The inner contacts are ferromagnetic and act as spin injector (2) and detector (3) respectively. The outer contacts may be either ferromagnetic or nonmagnetic. The substrate and gate oxide are neglected in this diagram in order to illustrate the magnitude of the spin current at any given point in the nanotube, which is proportional to the length of the red arrow or depth of blue in the box below.

model is an important consideration, especially in the case of CNT-based spin valves, which rely on the intrinsic formation of potential barriers at cryogenic temperatures. The height of the barrier influences the probability of tunneling, which in turn has an effect on the effective polarization of the charge carriers. Therefore, both the choice of ferromagnetic contact, and the chirality of the incorporated CNT, which influences the strength of the potential barrier, are critical components to obtaining a high TMR.

Another explanation for unexpectedly high magnetoresistance in some systems is the possibility of measuring effects other than TMR. When performing local measurements, it must be considered that several effects can make nonnegligible contributions to the measured signal. For example, anisotropic magnetoresistance, Hall effects, magneto Coulomb interactions, and tunneling or contact resistance effects all can influence the observed magnetotransport. The contributions of such spurious effects can be significant. For Co-contacted CNTs, it has been determined that only 3% of the signal intensity in a local measurement is the result of spin accumulation [4]. In order to measure a pure spin current, electronic configurations utilizing multi-terminal devices with more than one transport channel must be explored.

5.2 Nonlocal measurements

Fully electrical nonlocal spin detection was first achieved in 1985 [93] and has since become an important tool for separating spin and charge currents and determining parameters such as the spin diffusion length of a material. As seen in figure 5.4, a nonlocal CNT-based device consists of four contacts. Contacts 2 and 3, which act as the spin injector and detector, must be ferromagnetic. The two outer contacts may be ferromagnetic [4], or made from normal metal[26]. In this work, all contacts were made of the same FM material because of the chosen fabrication process. In order to measure spin accumulation, the distance between the injector and detector must be less than the spin diffusion length in the nonmagnetic material. The magnitude of the remaining spin current at a given lateral position is indicated by the height of the red arrows and intensity of the blue background in the lower box in figure 5.4. In figure 5.4, there is no spin current present under contact 4.

To perform a measurement, a constant current is applied between contacts 2 and 1, and a magnetic field is swept from positive to negative values and reverse. The FM contact 2 injects a spin polarized current into the CNT. The nonlocal voltage drop is measured between contacts 3 and 4.

When a polarized current is injected by a FM contact into a nonmagnet, an imbalance between the spin up and spin down electrochemical potentials is created in the nonmagnetic channel at the point of injection, as shown in figure 5.5. Between contacts 1 and 2, in the direct electrical path of the current, the charge current moves with drift velocity ν_d. The spin polarized electrons move via a combination of drift and diffusion. Outside of the path of the electrical current, diffusion alone controls the motion of charge carriers. Although no electrical current is present, a spin current exists until the spin diffusion length, $L_s = \sqrt{D\tau_s}$, is reached [40]. This length is thought to be at least several hundred nanometers in the case of a SWNT [4], after which the spin up and down chemical potentials are once again equal and spin current is no longer detectable. The range in which the detector must be placed is highlighted in yellow in figure 5.5.

In the case of the spin injector and detector being aligned in parallel, a nonlocal spin accumulation measurement is probing the positive electrochemical potential of the majority charge carriers, μ, resulting in a positive voltage drop along the nonmagnetic channel (between contacts 3 and 4 in figure 5.4). When the contacts are aligned antiparallel, however, the negative electrochemical potential of the minority electrons is detected, resulting in a negative voltage drop along the detection path. Therefore, a drop in resistance at applied magnetic fields between the coercive fields of the spin injector and detector is characteristic of a nonlocal magnetoresistance measurement. The nonlocal voltage measured may be defined as:

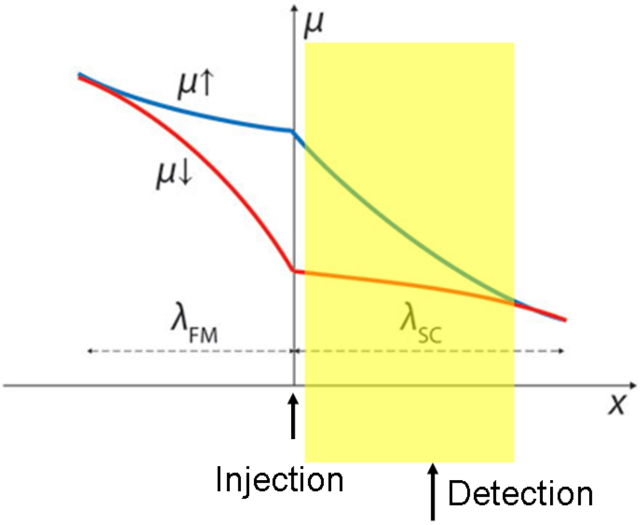

Figure 5.5: Electrochemical potential of spin up and spin down electrons. The values separate at the point of spin injection, and a spin current exists in a nonmagnetic channel until they come together again through a combination of drift and diffusion, before which detection occurs. Figure adapted from [40].

$$\Delta V_{nl} = \nu P_{FM} \frac{\Delta \mu}{e} \tag{5.7}$$

where ν is the zero-bias spin detection efficiency, which is dimensionless and considered to be around 0.5 for most semiconductors [94], P_{FM} is the polarization of the contact at the Fermi edge and e is the elementary charge, corresponding to 1.6×10^{-19} C. The exact value of ν for CNTs is unknown, and likely highly sample-specific, but may be approximated with that of a typical semiconductor. This method can further be used to characterize spin accumulation in the nonmagnetic channel by relating $\Delta\mu$ to the density of states in the channel at the Fermi level, resulting in:

$$\Delta V_{nl} = \frac{2\nu P_{FM} P_{channel} E_F}{3e} \tag{5.8}$$

Alternatively, a three-terminal (3T) configuration, in which the center contact is used for both the spin injection and detection path, is often used and considered to be a nonlocal measurement, both in the case of magnetoresistance and Hanle

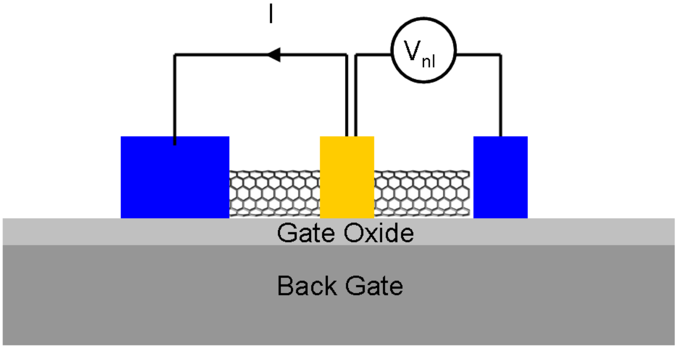

Figure 5.6: Schematic of a 3-terminal measurement setup in a CNT-based device. The center contact is part of both the application and measurement path, and can double as both spin injector and detector. The outer contacts may be ferromagnetic or nonmagnetic. In this work, all ferromagnetic contacts were used.

measurements, which are discussed below. A schematic of a 3T measurement configuration is shown in figure 5.6. Whether such a system is equivalent to a traditional four-terminal nonlocal setup is unknown, and appears to depend on the materials being used. It is hypothesized that the signal in 3T measurements may be enhanced by localized states at the contact/nonmagnet interface [95]. In systems where no localized states are expected to occur, such as in CNTs, which, unlike Si or GaAs are not doped by the contact metal, 3T measurements should give the same result as a nonlocal spin precession measurement.

5.2.1 Hanle measurements

In addition to using nonlocal TMR measurements to determine the spin coherence length of a material, it is possible to more directly measure the spin dephasing time via Hanle measurements. In a magnetoresistance measurement, an external field is applied in-plane parallel to the long axis of the sample for the duration of the experiment. In a Hanle measurement, the sample is first magnetized to saturation in-plane. Then, the sample is turned so that the field is applied out-of-plane. When a field sweep is performed while applying a constant current, the spins precess through the nonmagnetic channel toward the detector via diffusion driven motion. The rate of precession is the Larmor frequency:

$$\omega_L = \frac{g\mu_B B}{\hbar} \tag{5.9}$$

where μ_B is the Bohr magneton, and $\hbar$ is Planck's constant [94, 96]. An accepted g-factor for CNTs in an out-of-plane magnetic field is considered to be 2 [97].

The Larmor frequency is proportional to the externally applied magnetic field. Therefore, spins precess faster as the field is swept higher, eventually reaching a point where dephasing is complete and the Hanle signal obtained by an injector and detector with parallel and antiparallel alignment is equal. The shape of the Hanle curve, which plots the change in nonlocal voltage versus an applied magnetic field, may be fitted by a Lorentzian. At the full width half maximum (FWHM) position, the relationship between the Larmor frequency and the spin lifetime is:

$$\omega_L = \frac{1}{\tau_s} \tag{5.10}$$

Accordingly, fitting the curve allows one to extrapolate the spin relaxation time in a nonmagnetic channel. Hanle measurements are regularly performed in both the 3T and fully nonlocal configuration. Again, whether 3T measurements may be considered fully nonlocal appears to be material-dependent [96].

5.3 Conclusions

A typical CNT-based spin valve may be considered as a nonmagnetic channel connecting ferromagnetic leads through which ballistic transport occurs, and an intrinsic tunnel barrier between the contacts and CNT forms at low temperatures. For such a device, it is important to consider that according to the Slonczewski model [92], both the polarization of the contact material and the strength of the tunnel barrier can have a strong influence on TMR. The potential barrier is largely predetermined by the chirality of the CNT, although it may also be influenced by choice of contact material. Therefore, it is necessary to optimize the system in order to obtain reliable TMR. This has been partly done in this work by selecting CoPd as a contact material, as discussed in chapter 4. Chapter 7 will provide several examples of device-specific magnetotransport. When reading the following chapters, it is important to consider that similar devices can generate very different information, depending on the electronic configuration used to perform the measurement. While nonlocal measurements probe pure spin currents, and can provide information on the spin diffusion length through a CNT, and the polarization of the current, local (two-terminal) measurements tend to result in artificially high values for TMR, which appear to be enhanced by several local effects [4].

6 Transport in permalloy-contacted CNTs

Permalloy (Py) is a well-studied soft ferromagnetic material. Although the exact alloy varies slightly, $Ni_{81}Fe_{19}$ was used for all devices discussed herein. Permalloy could be considered a good contact material for spintronics devices for many reasons. First, the polarization is relatively high [7], allowing for injection of a highly polarized spin current. Secondly, permalloy has an fcc lattice, meaning that no large uniaxial magnetocrystalline anisotropy appears. Magnetization may therefore be more readily controlled via shape anisotropy, which is simple to define with contact geometry in quasi-spin-valve devices. Furthermore, in the case of thin films and structures, permalloy has been shown to magnetize in-plane of the sample with domains forming only at rather large dimensions, with thicknesses above $t = 50$ nm [98]. Therefore, achieving single-domain contacts that exhibit reliable, high-intensity, in-plane polarization reversal should be fairly straightforward. However, groups using permalloy to contact CNTs have had mixed results. Some groups have reported that permalloy resulted only in high-ohmic contacts to CNTs. The devices had to be annealed before measurement in order to obtain any signal, and were unreliable, with the signal decreasing over time [5]. Other experiments have achieved excellent results with Py-CNT-Py devices, obtaining stable TMR measurements with switching fields that correlated exactly to those expected according to AMR measurements [87]. Since the Py-CNT-Py system has been shown to achieve TMR, it was used as a reference in this thesis. Here, permalloy was found to form mostly low-ohmic contacts to CNTs, leading to promising devices. We were able to use such devices to learn about optimization of sample parameters and electronic settings in order to maximize TMR, as will be discussed in this chapter, and may also be found in reference [30].

This chapter begins by introducing the permalloy-contacted CNT devices used in this work, specifically with respect to fabrication and design. Transport measurements on different Py-contacted devices are detailed and discussed. Then, magnetic characterization of the as-measured samples is introduced in order to explain the functionality of different devices. The chapter concludes with a discussion of the use of permalloy as a contact material.

6.1 Device Fabrication

CNTs were grown and contacted with permalloy according to the process described in chapter 3. Permalloy was deposited via sputtering or electron beam evaporation, depending on the sample, with an intercontact spacing on the order of 250-300 nm, which is less than the spin dephasing length expected in both SWCNTs and MWNTs [4].

Two types of devices were fabricated. Originally, contacts were made to align in a specific direction, but with no specific geometry. These will be referred to as micro-contacts below. A topological AFM image of a device with micro-contacts may be seen in Fig 6.1a.

Later, the contact geometry was improved to consist of small bars of permalloy, as may be seen in Fig 6.1b. This is expected to improve the quality of the magnetoresistance signal, as shape anisotropy is better controlled, and there is no longer the possibility for domains to form due to slight changes in the contact direction. Ideally, the structures should contain a small enough amount of material so that domain formation is no longer energetically favorable. Smaller devices will have fewer pinning sites, both due to lack of domain walls and less chance of roughness from the fabrication process. The long axes of the patterned bars are in the range of 3 micrometers, and the shorter sides on the order of hundreds of nanometers. Throughout this work, these and similar fabricated structures will be referred to as nanocontacts. The nanocontact devices were fabricated in the same way as above, but with large parts of the contact also made of gold. Fig 6.1b contains an AFM image of such a device.

6.2 Transport measurements

In this chapter, three devices will be discussed. Device parameters are summarized below in table 6.1. Although fabricated separately, all samples were grown at a temperature of 960 °C, where the formation of mostly double-walled CNTs is expected. As explained in chapter 3, results of CVD growth are statistical, however, CNT diameters, as measured via AFM, indicate values that are consistent with those expected for double-walled to few-walled CNTs, although AFM cannot be used to determine if the CNTs are concentric or formed as a rope or to calculate

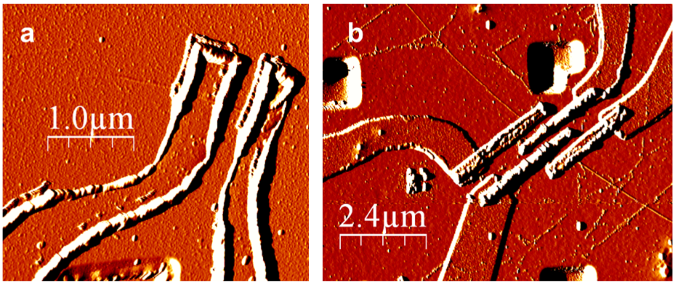

Figure 6.1: Atomic force microscopy images of CNT devices with (a) unshaped permalloy microcontacts, and (b) rectangular Py nanocontacts with large Au leads. Note: before imaging, the samples have been exposed to multiple thermal cycles, which may lead to dirt on the sample and slightly distorted contacts. Although a 4-terminal device is shown in (b), only local measurements will be discussed in this chapter.

the exact number of walls. Room temperature resistance values for the devices were all on a similar order of magnitude, indicating low-ohmic contact resistance of the CNT-Py interface. When cooled to 4 K, all samples experienced an increase in resistance, and the formation of a so-called ”s-shaped” I-V characteristic, indicating the formation of a potential barrier, as described in chapter 3. The 4 K resistance levels indicated in table 6.1 correspond to the voltages applied when performing measurements.

All transport measurements discussed here were performed in a He-4+ cryostat at a temperature of 4K, and an external magntic field sweep was applied in plane of the sample along the long axis of the contacts. In the case of measurements with a nonuniform background resistance, the values for ΔR are taken as an average of each side of the peak. The bias voltage used for measurements varies with each device, and was chosen so that the overall current between two contacts in a two-terminal measurement was in the range of 1-10 nA. This range was first chosen as it has previously been shown that magnetoresistance is higher when a low voltage is used [23]. In this work, this was often the lowest range able to give results that were well beyond the noise limit of our measurement systems. When much higher currents were applied, no magnetoresistance was observed, and the noise level increased, likely due to local heating at the contact-CNT interface or to an increase in ohmic effects as the tunnel barrier is bypassed by more electrons.

Table 6.1: Summary of fabrication parameters and electronic data for the three Py-contacted CNT devices discussed in this chapter.

Sample name	diameter (nm)	R(300K)(kΩ)	R(4K)($R_{\|\|}(k\Omega)$)	$\Delta R(\%)$
Py1	1.5	143	835	0.8
Py2	3.5	317	520	12
Py3	2	51	1000	5

6.2.1 Device with micro-contacts

For the inital devices, represented by Py1 from Table 6.1, contacts were made by sputtering permalloy. As seen in figure 6.1a, this resulted in the formation of slight sidewalls in many of the devices. However, the room temperature resistance tended to be stable and relatively low, with several devices in the range of 50 kΩ - 1 MΩ.

When cooled to 4K, the sample continued to show stable I-V characteristics, while indicating the formation of a potential barrier. Magnetoresistance measurements subsequently performed on the sample also led to repeatable switching behavior. Figure 6.2 shows one of several magnetoresistance curves taken with $V_{bias} = 20$ mV. A magnetoresistance of ΔR=0.8% was measured with a peak occurring at approximately $+/-80$ mT. It is observed that the rise in resistance after passing zero external field, corresponding to the polarization switching of the wider contact, is gradual rather than abrupt. This indicates that the wider contact is subjected to an effect that inhibits spins from abruptly rotating to the opposite polarization, such as pinning sites at domain walls or lithographic roughness. The signal then sharply drops at an external field corresponding to the coercive field of the narrow contact. Such an asymetric switching is fairly common and has been observed previously in Py-CNT-Py devices [5]. In this case, it can likely be attributed to geometry, where either an out-of-plane magnetization component is introduced by the large amount of extra Py in the side walls, or the eventual widening of the contacts, far from the nanotube, introduces extra magnetic domains.

In the case of this sample, no measureable magnetoresistance was obtained at lower bias voltages due to lack of a functioning back gate.

While it was possible to measure MR with Py1, the sample was far from ideal. The ΔR observed was extremely low, as local magnetoresistance of 100% or more has previously been observed in CNT-based devices contacted with cobalt [23]. Furthermore, the non-abrupt switching makes such a sample less sensitive and controllable. The next step to obtain better results was to carefully optimizing the contact geometry in the devices.

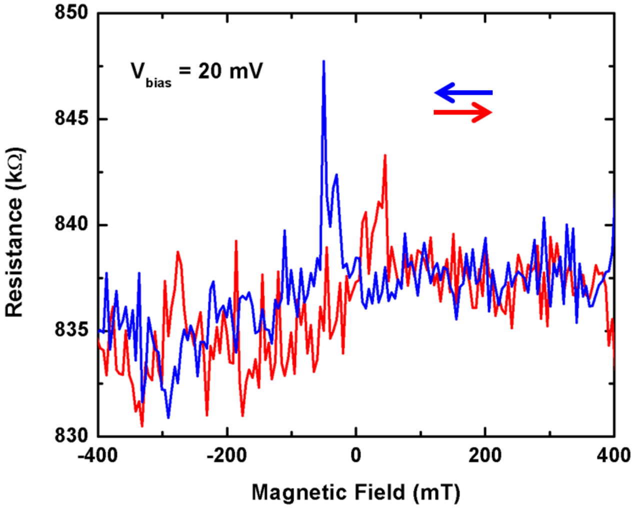

Figure 6.2: Magnetoresistance measurement taken on the device Py1. Bias voltage = 20 mV, and no gate voltage is applied. The magnitude of MR in this device was $\Delta R = 0.8\%$.

6.2.2 Device with nanocontacts

The simplest approach to obtaining contacts that are free of pinning sites is to improve the fabrication process. Therefore, for subsequent samples, electron-beam evaporation of Py was used instead of sputtering. It can be seen in figure 6.1(b) that this technique does indeed stop the formation of sidewalls. Both images do show some surface roughness, but this is at least partially caused by thermal cycling of the samples, as the images were taken after the samples had been cooled for measurements three times. A second change in the fabrication process was made with regard to designing the contacts. Here, it was attempted to create contacts with single magnetic domains by limiting their size to several μm × 100-500 nm, dimensions which have previously been shown to lead to single domains in Py. Thickness must also be considered. As it has previously been shown that Py transitions from having out-of-plane Bloch walls to in-plane Néel walls at an approximate thickness $t = 45$ nm [5], 40 nm thick contacts were used. Large gold leads then connected the contacts to the bonding pads.

The result of one magnetoresistance measurement performed on a nanocontacted sample, Py2, may be seen in figure 6.3. This measurement was repeated multiple times, and always resulted in a sharp peak at +/− 30 mT followed by a gradual return to the base resistance level. The abrupt jump in resistance likely corresponds to the coercive field of the wider contact. However, the exact magnitude of the jump, as well as the base resistance fluctuated slightly between measurements. For this measurement, $V_{bias} = -5$ mV was used. Changing the bias had no clear effect on the shape or magnitude of the MR. The sample seemed to be only weakly coupled to the gate, and no gate-dependence was observed. TMR of ΔR=12% was recorded, using an average of the two sweep directions. This is indeed much higher than that seen for Py1. However, the shape of the MR is still far from ideal, although in this case the wide contact switches abruptly while the narrow contact appears pinned. Magnetic characterization of the device, discussed below, attempts to explain this observation. Additionally, there was no clear electronic control of the device via bias or gate voltage, making it impossible to optimize the MR.

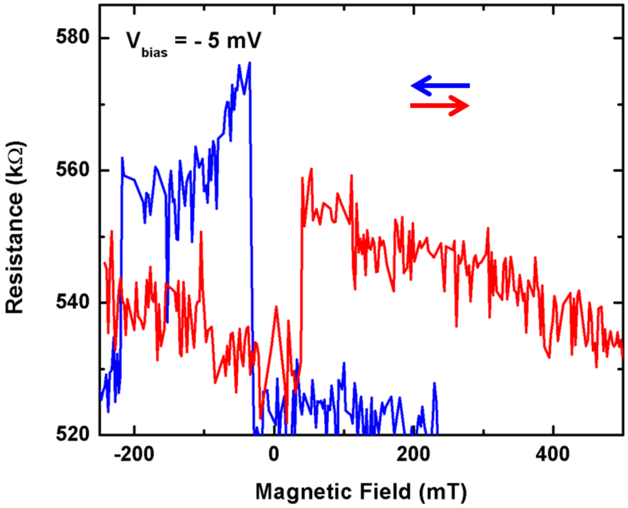

Figure 6.3: Magnetoresistance measurement taken on the device Py2. Bias Voltage = -5 mV, and no gate voltage is applied. The magnetoresistance of this device varied strongly, with only one sharp switch, but was approximately 12%.

Py3 is another device fabricated on the same chip as Py2, although measured at a different time. Unlike Py2, this device showed a strong coupling to the gate when cooled to 4K. Fig 6.4 shows gate sweep measurements of the sample, where the bias voltage was constant at +/-2 mV and -5 mV. Coulomb oscillations appear in the entire sweep range, indicating the formation of a potential barrier, as expected for

Py-contacted CNTs [5]. The oscillations reproduce nicely over several bias voltages, which shows the stability of the device. While room temperature measurements suggested that the CNT was chirally metallic, the low-temperature gate-dependence indicates that the CNT is either a semimetal with a small bandgap that is overcome by thermal excitation at room temperature, or is indeed a metallic CNT experiencing the opening of a stress-induced band-gap [66].

In the measurements, two distinct transport regimes may be defined. First is the few-electron tunneling regime, which is present when a gate voltage between 0 and -1.2 V is applied, labelled as Regime I in figure 6.4. When $V_{bias} = +/-2$ mV is used, gate-dependent conduction fluctuations approach zero from both the positive and negative direction, although never appearing to fully reach zero. When $V_{bias} = -5$ mV is used, the current is higher, and it can be more clearly observed to oscillate around zero while never being completely suppressed, meaning the device never reaches Coulomb blockade. At this point, the sample is clearly operating in the few or multiple-electron tunneling regime.

Regime II appears at V_{gate} below -1.2 V. Here, the Coulomb oscillations are less pronounced, although still present at all biases, indicating that a tunnel barrier is still contributing to the transport properties of the device, and gate control is still possible. However, the current remains high, rather than fluctuating back to a value around zero, as seen in Regime I. This is clearly caused by the device beginning to behave as an opening transistor, rather than simply allowing a few electrons to tunnel at a time. It is therefore necessary to consider the possibility of an additional ohmic contribution to the resistance, which can strongly influence magnetotransport, as discussed below. In both transport regimes, the peak positions of the oscillations are reproduced at the same gate values for all biases, indicating the high electronic stability of the device.

Magnetoresistance measurements were then performed on the sample using a bias voltage V_{bias}= -5 mV at various gate voltages representing both transport regimes I and II. First, measurements were taken at V_{gate}= 0 and -0.4 V, points clearly in the few-electron tunneling regime. For these measurements, no MR was observed, although it is possible that MR was present, but less than 1%, and therefore lost in the signal-to-noise ratio of the measurement. Figure 6.5 shows MR measurements performed using V_{bias} = -5mV and V_{gate} = -1.37 and -2 V respectively. Both of the latter points are in Regime II. Clear peaks in the resistance values were measured between -5 and -25 mT and 20-45 mT (a slight shift toward positive fields was observed, likely due to exchange bias between the uncapped Py and an antiferromagnetic native oxide), with MR = 3% for V_{gate}= -1.37 V and 4.5% for V_{gate}= -2 V.

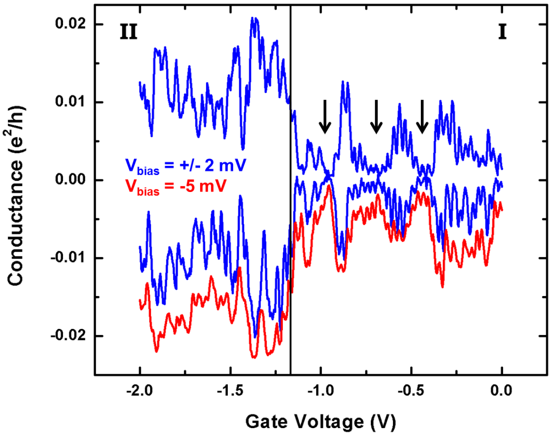

Figure 6.4: Gate sweeps performed on the sample Py3 at various bias voltages. Both a multiple-electron tunneling regime (I), and an opening-transistor regime (II) are observed. Arrows indicate areas where conductance is approaching zero.

Transport regimes

Back-gated devices may be considered as transistors which have a closed state at certain voltages, then begin to open at a critical threshhold voltage. As CNTs grown on oxides tend to be p-doped [75], this is usually best observed by sweeping the gate to a negative voltage. Is is often attempted to manipulate magnetotransport via changing the electronic state of the sample. This can be done by using a capacitively coupled backgate, which controls level splitting within the device, changes the overall conductance through a nanotube, and helps to define the potential barrier between the CNT and the source/drain, all of which can possibly restrict or facillitate spin transport. Therefore, the ability to drive a device to different regimes is a valuable tool in understanding and optimizing magnetoresistance. Additionally, the likelihood of spurious effects, such as local ohmic contributions, also depend on the electronic regime of a sample, so it is crucial to consider the regime in order to rule out such effects and determine the validity of the measurement.

Perhaps the most well-studied is the single-electron tunneling (SET) regime. A device is in the SET regime when, by sweeping a gate voltage, it is possible to inject one electron into the nanotube. Over a large range of gate and bias voltages, this is characterized by a pattern of Coulomb diamonds. To achieve SET, the bias

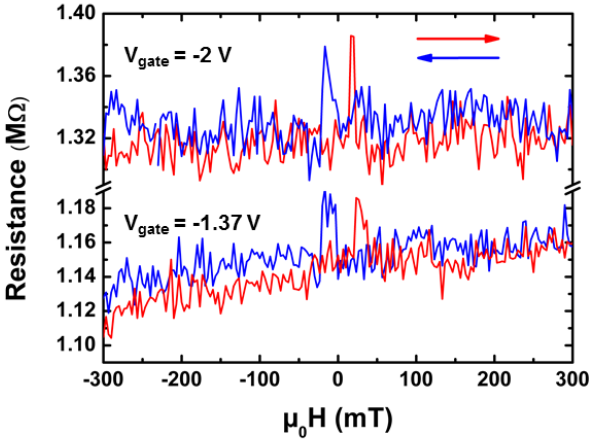

Figure 6.5: Magnetoresistance measurement taken on the device Py3. Bias Voltage = -5 mV, and gate voltage is -1.37 V (lower curve) and -2 V (upper curve). The magnetoresistance of this device was gate-dependent.

voltage must be low enough that only one electron tunnels from the source. For CNT-based devices, this regime usually occurs only at subKelvin temperatures in a dilution refrigerator, where thermal excitation is negligible and the sample is in full Coulomb blockade, highly increasing the contact resistance. Much work has already been devoted to studying both electronic and magnetic transport through CNTs in this regime [25].

When the transistor is completely opened, devices may be said to be operating in the Fabry-Perot regime. The Fabry-Perot regime is reached when the contacts approach complete transparency. The electronic signature for devices in the Fabry-Perot regime are gate-dependent oscillations with a conductance reaching $4e^2/h$ for a gate sweep at constant bias. In the case of a two-dimensional measurement where multiple side gates are swept, a tartan pattern is observed, due to interference effects. In this case, where the system acts as multiple interferometers in series, the effect of phase coherence on spin transport can be studied [26].

Py3 operates in two distinct regimes, defined above, that are intermediate to the SET and Fabry-Perot regimes. In regime I, the oscillations never fully close, as they would in the case of SET, especially when a bias voltage $V_{bias} = -5$ mV is applied. As seen in 6.4, the overall conductance of the device is on the order of $0.1e^2/h$ at the highest point in regime II, indicating that even as the transistor opens, the device is never transparent enough to be operating in the Fabry-Perot regime. Py3 may therefore be used to gain understanding of electronic control of magnetoresistance in such intermediate regimes.

Spin transport dependent on electronic regime

The inverse relationship between conductance and TMR has already been shown in the single-electron tunneling (SET) regime. Previously, Sahoo et al. [25] performed a gate sweep of a PdNi-CNT-PdNi device showing clear Coulomb diamonds. They were then able to measure local magnetoresistance at a series of gate voltages, which demonstrated that as the conductance of the device increased, the TMR decreased, even becoming negative at the very peaks of the Coulomb diamonds, ranging from +17 to −7 %. The dependence was shown to be almost exactly inverse, with a small offset that is likely due to a small misalignment of the sample within the magnetic field.

Recently, PdNi-CNT-PdNi devices in the Fabry-Perot regime have also been investigated for both two [99] and four-terminal [26] devices. The two-terminal devices in this regime showed only positive TMR, with a maximum ΔR=4%, which is much lower than the results seen in [25]. This is attributed to the fact that the conductance through the sample is an order of magnitude higher. In the four-terminal devices, conductance is even lower than for the devices measured in reference [25]. As expected, such a measurement results in a higher, negative TMR. In both the local and nonlocal measurements, devices in the Fabry-Perot regime showed a similar dependence of TMR on conductance as devices in the single-electron tunneling regime.

Other than the magnitude of the TMR, which is extremely sample-specific, another difference between the local measurements in different regimes is the amplitude of the MR oscillations with respect to gate voltage. In the SET regime, the magnitude of TMR oscillates constantly with respect to overall conductance, seeming to return to a given maximum and minimum value. However, the device in the Fabry-Perot regime shows an increase in the minimum TMR as the gate voltage is increased, while the maximum TMR remains relatively constant. No explanation is presented for this small effect. One possible cause is that while in the SET regime, it may be assumed that all current enters the device through a tunnel barrier, in the Fabry-Perot regime, ohmic effects must be considered to also influence the measured TMR.

As we are measuring between these regimes, it is important for us to consider this possible shifting in the minimum TMR. While we do not have enough measurement points from Py3 to make a direct comparison to the papers discussed above, we observe the same trend of TMR decreasing when conductance through the sample increases. Although we are far away from $4e^2/h$ point, and the conductance we see is closer in magnitude to the SET regime, we also achieved no measurable TMR in the purely tunneling regime. This could be a result of ohmic contributions increasing the TMR to a detectable level in regime II in our sample. The lower TMR we observe is attributed to the fact that the device Py3 exhibited much more transparency than the NiPd contacts discussed above.

Our data provides an important addition to the current understanding of how gate-dependent MR works. It has previously been shown that for devices in the SET and Fabry-Perot regime, the maximum MR signal is observed at gate voltages corresponding to a minimum in the current[25]. Our measurements show that this effect is not linear when driving the device out of the SET regime. While for small currents in Regime I, any MR present was below the detection limit, a larger signal appeared in Regime II, as the gate began to drive the device into the p-conduction region, even though the absolute current through the device was much higher. However, within Regime II, larger MR was obtained at $V_{gate} = -2$ V than at $V_{gate} = -1.37$ V, even though the absolute current was lower, in agreement with established results within both regimes [25]. Driving a device into Regime II is therefore one way to improve local TMR in a CNT-based quasi-spin valve.

6.3 Magnetic characterization

As described in chapter 3, our devices often have extremely different electrical properties based on the electronic structure of the contacted nanotube, which cannot be determined by the growth process. Both the contact resistance of the device and the number of walls of the CNT have previously been considered to have an effect on the device magnetoresistance [23, 100, 101, 102].

Furthermore, it is frequently the case that devices with similar electronic properties exhibit different magnetoresistance. Our samples Py2 and Py3 were fabricated on the same chip under identical conditions. While not identical, the devices were comprised of CNTs of similar diameter and room temperature resistance. After cooling to 4K, the devices exhibited similar resistance increases, and their low-temperature I-V characterizations both indicated the opening of a small potential barrier. However, Py2 yielded high magnitude but oddly shaped magnetoresistance while Py3 showed a small but abrupt switching. A likely reason for the unclear switching observed in Py2 is that one of the contacts is unable to abruptly switch polarization due to a pinning site. Pinning often occurs at domain walls, but has many other potential causes, for example, surface roughness due to the fabrication process, or stray-field interactions between contacts that are too close together. In this section, we study the sample Py2 using magnetic force microscopy, which was briefly introduced in chapter 4, in order to characterize the sample and determine possible sources of pinning.

6.3.1 Magnetic force microscopy of device

Figure 6.6a is an AFM image of Py2 after multiple thermal cycles. Dirt on the sample is a result of thermal cycling and removing the sample from the chip carrier. Here, it may be seen that the contacts are roughly 300 nm apart (the same spacing applies for the other devices discussed here), and the narrow contact has a high surface roughness in the area directly over the CNT. It is unclear whether this is a result of lithography or thermal cycling.

The sample was then magnetized along the main axis of the contacts and MFM was performed in remanence. Figure 6.6b shows the magnetic data superimposed over a height image for clarity. In the image, a black and white spot appear at opposite ends of the contacts (this effect was also present at the other end of the narrow contact, not visible here). This is typical of single-domain structures measured in MFM, as the tip interacts with the stray fields resulting from the north and south pole of the magnet. Here, the direction of magnetization is in plane along the long axis of the contact, as expected, and the stray fields of the contacts do not appear to influence the magnetization of the neiboring contact. It can also be seen that the rough part of the narrow contact differs from the rest of the area. While the majority of the contact is in a single domain state, this local area exhibits less in-plane magnetization, possibly due to extra material locally pushing the magnetization out of plane. As this area is directly over the CNT, this magnetic behavior would be expected to have a strong effect on spin injection or detection. Indeed, in figure 6.3, the magnetoresistance measurements of Py2 show an abrupt switch at the lower coercive field, corresponding to the wider, smooth contact, while the outer switch, corresponding to the narrow contact occurs gradually or in individual jumps. As discussed above, magnetoresistance in this device was still fairly repeatable, especially with regard to the coercive field of the wider contact. However, MFM data clearly shows that in order to have abrupt switching occur in a chosen magnetic field range, carefully controlled and consistent contact geometry in all directions is important.

6.4 Conclusions

In conclusion, reference samples with high-transparency Py contacts provided valuable information about optimizing local TMR in CNT-based devices. One important finding was the importance of contact geometry. Nanostructuring the contacts into

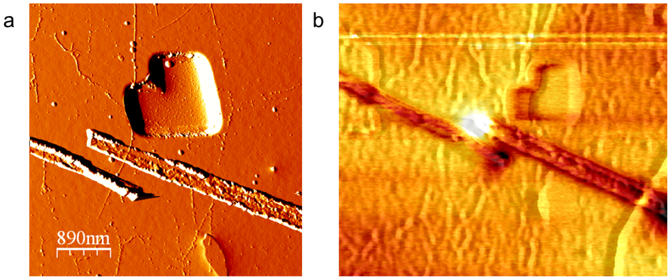

Figure 6.6: (a) Atomic and (b) magnetic force micrograph of device Py2. In (b), magnetic data is superimposed over topological data as a guide to the eye. Single domain magnetization is observed, with a likely pinning site due to surface roughness in the lower (narrow) contact.

single-domain magnets was shown to clearly improve the shape of MR. Even in structured devices, fabrication-induced defects were shown to cause pinning and result in non-abrupt switching. Therefore, in order to achieve reliable switching, it is necessary to have a sample with smooth, single-domain contacts, which will be the case for any contact material.

When a reliable, working device was achieved, the TMR was quite small, approximately 3%. Gate-dependent TMR measurements indicate that ΔR is increased as the device is driven out of the few-electron tunneling regime and begins to act as an opening transistor. Until now, this regime has been largely unreported, despite being of interest for potential future applications. This regime is of special interest to this work, as it investigates high-transparency contacts, which often result in devices within this electronic regime even without applying a gate voltage. As discussed in chapter 5, the strength of the potential barrier has a strong influence on TMR, which will be extensively studied in the following chapter, as we attempt to further optimize TMR via the fabrication of higher transparency CoPd contacts.

7 Magnetoresistance and transport in CoPd-contacted CNTs

The CoPd material system was fully characterized, as presented in chapter 4, with the main result that with careful control of the geometry, $Co_{50}Pd_{50}$ is expected to be an excellent choice of contact material for a CNT-based spintronics device. Electrically, the material forms a stable low-ohmic contact to CNTs, but loses its transparency and forms an intrinsic tunnel barrier at 4 K. Magnetically, CoPd structures exhibit reasonably high, in-plane magnetization when the dimensions are carefully designed. With this in mind, the next step is to transfer the expected results into the reality of transport measurements. As transport in CoPd-CNT-CoPd devices has never before been reported, and as results are extremely sample specific, the ideal nanotube chirality or size for MR measurements is unknown. The nanotubes used in this chapter were mostly grown at high temperatures and were likely multi-walled carbon nanotubes (MWCNTs), according to the average diameter seen in AFM height profiles. MWCNTs were chosen for this study as they allow for a large contact-CNT interface. It has previously been shown that CNT-based devices with Co contacts show the highest ΔR when a low bias is used [23], although that result doesn't always appear to hold true when fabrication parameters are altered [4]. The temperature-dependence of MR for this system is also unknown, although it may be estimated based on that of Fe-CNT-Fe devices [77]. In order to accurately determine such parameters, a large number of samples must be studied.

It is also necessary to consider all possible causes of the MR signal. In two-terminal measurements, local electrical and magnetic effects often introduce an extra component to the measured data. Nonlocal measurements are the only way to definitely show spin injection and detection in the devices.

This chapter begins with a brief discussion of magnetoresistance in nonshaped CoPd contacted CNTs. The focus then moves to devices with optimized oval-shaped contacts, which gave improved results and were the main goal of this work. First, local MR was studied, focusing on the changing shape and magnitude of ΔR for various samples, and with respect to bias, gate voltage, and temperature. Finally, preliminary nonlocal MR measurements, which offer the first proof of spin injection in CoPd-CNT-CoPd devices, are presented. All samples in this chapter were fabricated with $Co_{50}Pd_{50}$ contacts, which will henceforth be abbreviated CoPd.

Results in this chapter are summarized in references [30], [31] and [32].

7.1 Micro contacts

CoPd-CNT-CoPd devices were fabricated using standard metallization and liftoff techniques on as-grown CNTs. CoPd was coevaporated via molecular beam expitaxy. The first devices were fabricated using contacts shaped only at the ends, which then extended to be as long as one mm and had an arbitrary direction. An AFM image of such a device is shown in figure 7.1(a), in comparison with the device with nanocontacts shown in (b). Magnetic imaging of similar samples (see figure 4.3) showed ordered stripe domains with dimensions up to several μm.

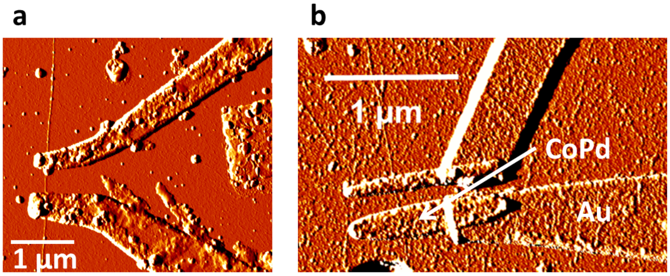

Figure 7.1: Atomic force micrograph of 2-terminal CoPd-contacted nanotube devices with (a) unshaped contacts and (b) carefully designed nanocontacts and coarse gold leads. Magnetic data for similar structures is presented in chapter 4. Images were recorded after thermal cycling of the devices.

Devices with such complex magnetic structure would be expected to exhibit complex MR as well. Figure 7.2 shows that this is indeed the case. At T = 4 K and $V_{bias} = 20$ mV, the magnetoresistance resembles a hysteresis curve. Such a measurement is referred to as a minor loop, and occurs when the magnetization of one contact remains unchanged during the magnetic field sweep, usually due to pinning. In principle, sweeping the field to a higher value would eventually overcome the pinning and a normal MR peak would be observed. However, this is far from ideal, as spintronics applications rely on sensitive low-field writing and readout. The unpinned contact in this measurement appears to switch polarization fairly sharply.

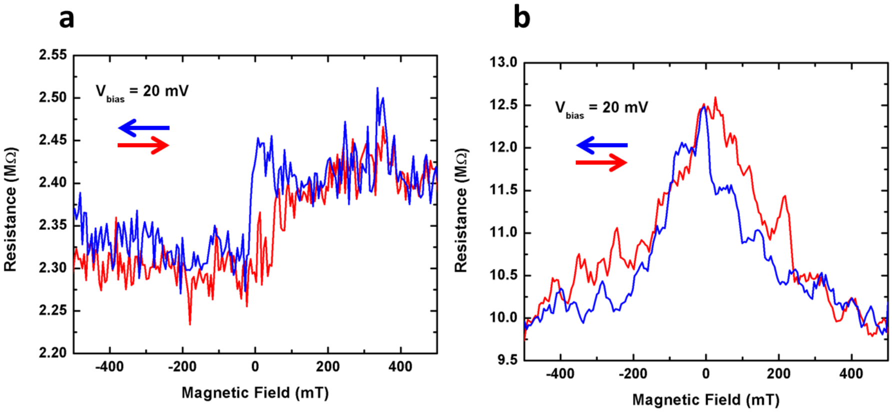

Figure 7.2: Local magnetoresistance measurements on the device shown in figure 7.1a performed at T = (a) 4 K and (b) 50 K. V_{bias} = 20 mV in both measurements.

At T = 50 K, thermally activated domain wall motion comes into play, allowing both contacts to switch polarization when an external field is swept. However, the switching is no longer abrupt. Rather than the ideal, sharp peaks occurring exactly at the coercive fields of the two contacts, a large, gradual peak is observed. This is in agreement with the temperature-dependent SQUID data presented in chapter 4, which shows a strong decrease in remanent magnetization at 50 K due to the magnetoelastic effect.

Despite the nonideal switching, one benefit of using CoPd contacts may already be noted. In comparison to the nonshaped Py reference contacts, where $\Delta R = 0.7\%$ was recorded (see chapter 6), this device gave $\Delta R = 2.5\%$. While the magnitude of MR is highly device specific, this suggests that CoPd contacts perform at least as well as permalloy, which is a well-established contact material.

7.2 Nanocontacts

Both precharacterization and preliminary results are in agreement that CoPd will exhibit sharp in-plane polarization reversal only when geometrically restricted. Therefore, oval-shaped contacts with a long axis of 2-4 μm, short axes of 150-400 nm, and thickness of 10-40 nm were fabricated. An AFM image of a representative device is shown in figure 7.1(b). Many devices were studied and their characteristics are summarized in table 7.1.

Table 7.1: Summary of fabrication parameters and electronic data for the CoPd-contacted CNT devices discussed in this chapter. In the case of nonohmic I-V characteristics at 4 K, the resistance listed is that corresponding to the bias voltage used in transport measurements.

Sample name	diameter (nm)	R(300K)(kΩ)	R(4K)($R_{\parallel}(k\Omega)$)	$\Delta R(\%)$
CoPd1	0.9	400	1×10^5	na
CoPd2	8	25	32	2
CoPd3	0.7	3700	11000	6.4
CoPd4	5	35	30	0
CoPd5	2.5	35	70	20
CoPd6	1.6	150	210	5
CoPd7	3.2	1×10^3	9×10^3	12
CoPd8	3	350	31×10^4	5-17
CoPd9	1.5	nonohmic	higher	15

The device CoPd1 consisted of a SWCNT (diameter = 0.9 nm according to AFM) contacted with 4 μm × 400(150) nm oval CoPd contacts. The thickness of the contacts was 25 nm, capped with 5 nm Au. While the room-temperature resistance was ohmic, the device exhibited a strong increase in resistance of several orders of magnitude as the temperature dropped to 4 K, indicating the formation of a large potential barrier. The device also exhibited a strong gate-dependence. Figure 7.3 shows Coulomb oscillations measured for the device in a gate sweep using a constant bias $V_{bias} = 10$ mV at a temperature of 9 K. The oscillations never appear to close completely at zero current, which is probably due to the high temperature and bias used. At a backgate voltage of approximately $V_{gate} = 3.5$ V, the current drops to zero and it is no longer possible to manipulate the barrier height via sweeping the back gate, further indicating the presence of a semiconducting CNT with a band gap.

No stable magnetoresistance could be recorded for this device, despite attempts using multiple bias and gate voltages. A possible reason for this is that the capping layer circumvents the ferromagnetic CoPd, inhibiting spin injection [77]. Several devices fabricated on this chip failed to exhibit magnetoresistance. Therefore, future devices were prepared with a thinner capping layer of only 2-3 nm Au, or in some cases, without a capping layer.

7.2.1 Geometry dependence of local magnetoresistance

The section discusses results that were obtained in reference [88].

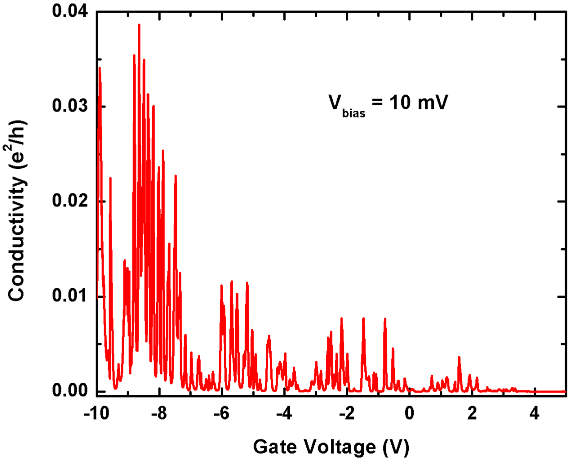

Figure 7.3: Bias current versus gate voltage dependence for the device CoPd1. 2-dimensional Coulomb diamonds, indicating gate control occur until V_{gate} = 3.5 V, at which point the current drops to zero, indicating the band gap of a semiconducting CNT. The measurements were taken at T = 9 K and V_{bias} = 10 mV. Measurement from [88].

As shown in chapter 4, extended films of CoPd have a complicated magnetic structure, which is simplified by structuring the material into small, single-domain nanocontacts. SQUID measurements provided an idea about how slight changes in the geometry would influence the magnetization of the sample. Here, we investigate precisely what this means with respect to local MR.

The first measurements were performed on the device CoPd2, which consisted of an 8 nm high MWCNT or rope with oval CoPd contacts of dimensions 4 μm × 150 (400) nm and a thickness of 10 nm. A 3 nm gold capping layer is added to improve electrical contact to the bonding pads. These dimensions were chosen as they are expected to result in largely single-domain contacts [29]. Figure 7.4 shows a magnetoresistance measurement with the blue (red) curves representing magnetic field sweeps in the negative (positive) direction. For this measurement, a constant voltage V_{bias}= 2 mV was applied. No gate dependence measurements were performed, and the low-temperature transport characteristics indicate a metallic nanotube, possibly with a small strain-induced band gap [66].

The device exhibits clear, abrupt switching, with resistance peaks from -2 – -13 mT and 6 – 21 mT. These values correspond to the coercive fields of the wide and narrow contacts, respectively. The slight shift in the positive direction is likely caused by a small misalignment of the sample with respect to the applied magnetic field.

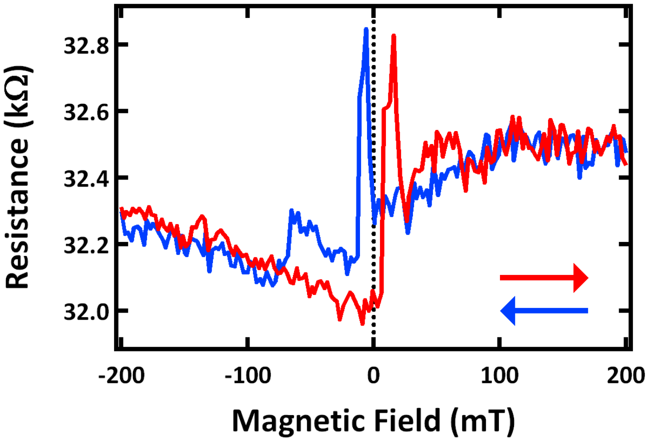

Figure 7.4: Local magnetoresistance measurement performed on the device CoPd2. Blue (red) curves correspond to field sweeps in the negative (positive) direction. Sharp peaks are observed, corresponding to the respective coercive fields of the contacts. The measurement was performed with a constant bias V$_{bias}$ = 2 mV.

The device has a TMR of $\Delta R = 2\%$. This value is rather small, and is likely due to the fact that the nanotube incorporated in the device is quite high, with a diameter of 8 nm measured via AFM. The contact above such a large CNT loses it's planarity, an effect which likely diminishes the overall magnitude of the in-plane magnetization, and thus the TMR. In addition to the main switching event, a side-switching appears at approximately +/- 50-70 mT. This switching, which occurred consistently but is more strongly visible in the negative sweep direction, is also thought to be the result of the planarization of the contact being skewed by the presence of the large multi-walled CNT or bundle [103]. Nevertheless, the shape of the main MR curve is ideal, with abrupt switching, and is repeatable over multiple measurements. The low TMR may also be the result of the tunnel barrier in the device being quite low, with only a small increase in resistance at 4 K.

Figure 7.5 shows a magnetoresistance measurement performed on the device CoPd3, a sample with a slightly different contact geometry. The contacts in this case were 4 μm × 400 (150) nm with a thickness of 40 nm. Again, negative (positive) field sweeps are indicated by the blue (red) curves. This device had a significantly higher resistance, and electronic characterization shows it to include a semimetallic CNT, or possibly a metallic CNT with a strain induced band gap [66]. The diameter of the

CNT was measured via AFM to be only 0.7 nm, which corresponds to a single-walled CNT. To accomodate for the different electronic state of the device, a higher bias of V_{bias} = 15 mV and a gate voltage of V_{gate} = -3 V were applied when performing magnetotransport measurements.

The 400 nm wide contact, which is expected to switch first due to shape anisotropy, no longer switched magnetization abruptly at a given coercive field. Rather, it appears to rotate gradually until the polarization is reversed. The narrow contact appears to experience domain pinning, switching only at high fields of -75 and 113 mT. Furthermore, rather than one abrupt switch, it seems to fluctuate back and forth before completely switching polarization, an effect which is especially noticeable in the positive sweep direction. This is thought to result from domain walls moving over the spin injection site, as spin injection occurs only at a specific point at the end of the CNT-contact interface [100].

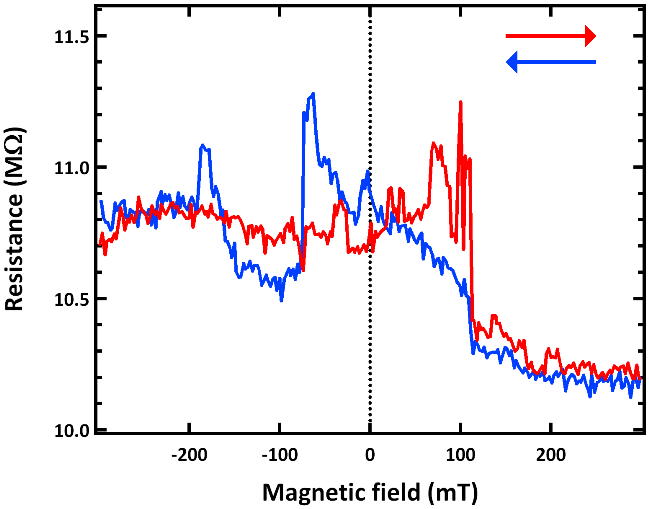

Figure 7.5: Local magnetoresistance measurement performed on the device CoPd3 with 40 nm thick contacts. Blue (red) curves correspond to field sweeps in the negative (positive) direction. The peaks begin gradually, corresponding to domain movement. A constant bias of 15 mV and a backgate voltage of -3 V were applied.

The magnitude of TMR in this sample was measured to be $\Delta R = 6.3\%$, which is a higher value than the other measurement. However, the shape of the MR data indicates a complicated magnetic structure in the slightly larger contacts. Furthermore, subsequent MR measurements performed on the same device resulted in switching with a slightly different shape and switching field, indicating the presence of multiple

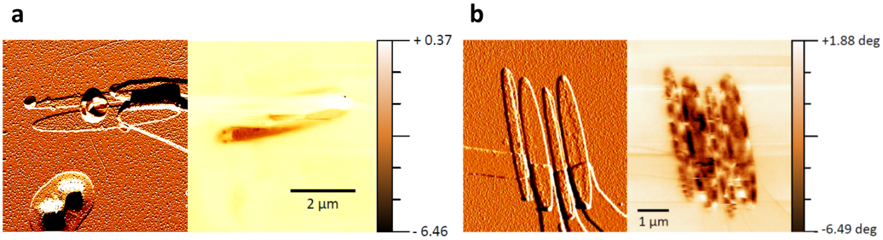

Figure 7.6: Topological characterization (left) via AFM and magnetic imaging (right) via MFM of the devices (a) CoPd2 and (b) CoPd3. Residual PMMA from an imperfect liftoff increases the roughness in (a), resulting in partially incomplete magnetic data.

domains and the occurrance of pinning. This device also appears to exhibit a side switching effect. In this case, it is likely the result of a step in the CoPd contact at the CoPd-Au interface, as the Au was deposited first in this sample. Similar to the other device, a nonplanar segment of the contact results in a secondary switching which occurs at higher applied field. The nonlevel background is likely an additional result of multi-step switching of the contacts.

In order to further our understanding of the transport behavior, additional characterization of the devices was performed. Magnetic force microscopy (MFM) was used to image the stray fields of the contacts in order to determine the domain structures. The samples were first magnetized to saturation in-plane parallel to the long axes of the contacts and then measured in the remanent state. Figure 7.6(a) shows an AFM topology image (left) and an MFM image (right) of the device CoPd2, discussed above, with 10 nm thick contacts. Unfortunately, residual PMMA from an imperfect liftoff makes it difficult to determine the domain structure of the entire sample, although the visible part shows only one clear domain. Together with the abrupt switching in the magnetoresistance data, this suggests the occurrence of a magnetic easy axis along the long direction of the contacts, as expected due to shape anisotropy. The TMR measurement of CoPd2 is clearly the result of one-to-two domain contacts exhibiting abrupt polarization reversal at their respective coercive field. This is the most reliable form of switching, as there is no influence of domain wall motion or pinning involved, and indicates that the smaller sized contacts are ideal for spintronics applications.

Figure 7.6(b) consists of two micrographs of the device CoPd3. To the left is a topological image, taken via atomic force microscope. Note: although the device had four contacts, measurements were performed between the two leftmost contacts only. Despite having been exposed to multiple thermal cycles, the device is shown to be in good condition, and the CNT is clearly visible.

The corresponding MFM image is shown on the right. Unlike in the other sample, multiple domains are clearly visible. It has previously been shown via SQUID magnetometry that CoPd exhibits a Bloch-Néel wall transition between 20 and 40 nm[29]. Therefore, the 10-nm thick contacts should contain only Néel walls, in which the local magnetization vector rotates in-plane to the sample, while the 40-nm contacts may include Bloch walls, in which the local magnetization vector rotate out-of-plane to the sample, and therefore require more energy to move via the application of an in-plane field. The MFM data shown here is in agreement with these findings. Furthermore, the inclusion of Bloch walls corresponds well to the TMR data, where the gradual switching is caused by domain wall shifting.

A slight difference in the domain structure of the wide and narrow contacts may also be observed in figure 7.6(b). The wider contacts have contrasting domains at the edges, but no clear domain structure at the center. In contrast, the narrow ovals exhibit a regular closure-like domain pattern throughout the contact. This also nicely compliments the transport data where the first switch, corresponding to the large contact, begins as soon as the field is swept to negative values, and continues gradually as the domains shift. The second switching, which occurs more abruptly, but only at quite high fields, and after significant fluctuation, is the result of many more domains being present in the narrow contact, which induce an additional pinning of the magnetization of the contact until it is saturated by a high external field. The dependence of the domain structure on in-plane geometry is likely the result of the narrow contact having a higher shape anisotropy. The effect is missing in the 10 nm thick contacts, which have a different in-plane shape anisotropy defined by their lower thickness. In the case of the thicker contacts, the effect of in-plane geometry on the magnetization of a contact must also be considered when designing spintronics devices, especially in materials like CoPd, which display a nontrivial magnetic behavior [29].

7.2.2 Sample-specific local magnetoresistance

While contact geometry is extremely important, it is not the only factor found to influence local MR in CoPd–CNT–CoPd devices. This section compares five devices with oval CoPd contacts of dimensions 2 μm × 400(150) nm × 20 nm. Throughout this section, applied biases are selected to optimize the MR signal.

Electronic characterization of the first device, CoPd4, is presented in figure 7.7. The device CoPd4 exhibited low ohmic resistance at room temperature, and a slightly lower ohmic resistance at cryogenic temperatures, which is indicative of a metallic

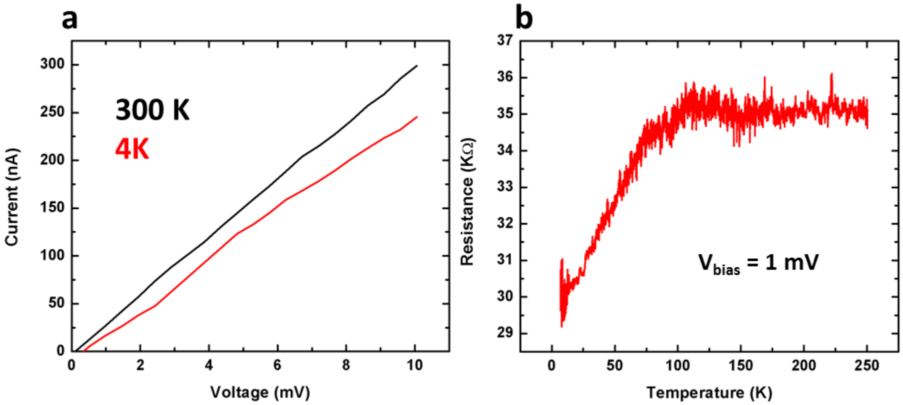

Figure 7.7: Electronic characterization of the device CoPd4. (a) I-V curves taken at room temperature (black) and 4 K (red) show ohmic behavior, with a reduced resistance at 4 K. The temperature vs resistance plot ($V_{bias} = 1$ mV) in (b) confirms that a metallic CNT is incorporated in this device.

device, in which resistance decreases at lower temperature as fewer scattering events occur. This is further confirmed by the resistance vs. temperature data plotted in (b), which shows a steady decrease in resistance beginning at T = 100 K. Unsurprisingly, the device exhibited no gate dependence. Additionally, no measurable MR was observed.

It has been shown both experimentally and theoretically that both the polarization of the ferromagnet and the strength of the insulating tunnel barrier influence the magnitude of TMR in a tunnel junction [104, 76]. While the effect hasn't been reported for devices with intrinsically formed barriers, a similar result may be expected. Tunneling magnetoresistance, which is widely thought to be the source of MR in CNT-based spin valves [21], requires the formation of a tunnel barrier, an event that occurs spontaneously at many CNT-metal contacts. Both semiconducting and semimetallic CNTs will intrinsically form a potential barrier with a metallic contact due to band bending at the interface. Furthermore, experience shows that many metallic CNTs develop a strain-induced band gap at low temperatures [66]. The reproducibility and intensity of TMR is likely closely linked to the stability and strength of the tunnel barrier, which is intrinsic to the nanotube, and therefore device dependent. In the case of device CoPd4, which contains a nanotube with no Schottky barrier formed at low temperatures, no potential barrier is formed, and thus TMR cannot occur.

Transport data for the device CoPd5 are presented in figure 7.8. From the I-V characteristics in (a), it is already clear that this device is electronically quite different from the device discussed above due to the formation of a potential barrier at low temperatures. The band gap appears to be quite narrow. Figure 7.8(b) shows the results of sweeping the back gate, while applying a constant bias of V$_{bias}$ = +/- 1 mV. While the resulting bias current is slightly higher in the positive direction, indicating different barrier heights between the CNT and the source and drain electrodes, the curves approximately mirror one another around zero current. Slight gate-dependent oscillations appear to exist, however the ability of the gate to tune the sample appears to be extremely weak, further indicating that only a small band gap is present.

Magnetoresistance measurements are plotted in (c) and (d) for applied voltages V$_{bias}$ +1 mV and -1 mV, respectively. While ΔR is quite high in both cases, approximately 20%, the shape of the MR curves is not ideal. The trace in (c) shows negative MR. The peaks are extremely broad, and are overlaid on a wide background resembling a hysteresis loop. The MR in (d) is even less complete, resulting only in a minor-loop, where polarization reversal is only recorded for one of the contacts. Once again, the nature of MR may be attributed to the electronic state of the sample. The existence of a small tunnel barrier allows some signal to be present. However, the barrier appears to be both narrow and uneven at the source and drain, resulting in poorly controlled MR. As it is unknown whether the resistance value would return to the original value if a high enough field was applied to flip the polarization of the second contact, the value of MR is only an estimate.

Figure 7.9 contains transport data for the next device, CoPd6. While the I-V sweeps at both room temperature and 4 K, shown in (a), appear to be roughly linear, the resistance increase at low temperatures, shown both in (a) and in the R vs. T sweep plotted in (b), indicate the formation of a small potental barrier, likely resulting from a semimetallic CNT.

MR data for the device, where V$_{bias}$ = 3 mV, is shown in (c). The shape of the curve is excellent, resulting in switching of both contacts at small fields. The measurement was repeatable, indicating that the device is highly sensitive to low fields, which is a requirement for many spintronics applications. The background was constant, and is not entirely understood, although similar backgrounds have previously been observed and are considered to be the result of electron-magnon interactions [5]. The magnitude of MR, $\Delta R = 5\%$, is relatively low. Again, this is likely the result of a weak tunnel barrier limiting the polarization of the current, although in this device, the barrier seems to be higher than in the device CoPd5, described above.

Increasing the height of the barrier via the back gate should, in principle, increase ΔR. Unfortunately, it was not possible to measure gate dependence in this device, as the back gate exhibited a leakage.

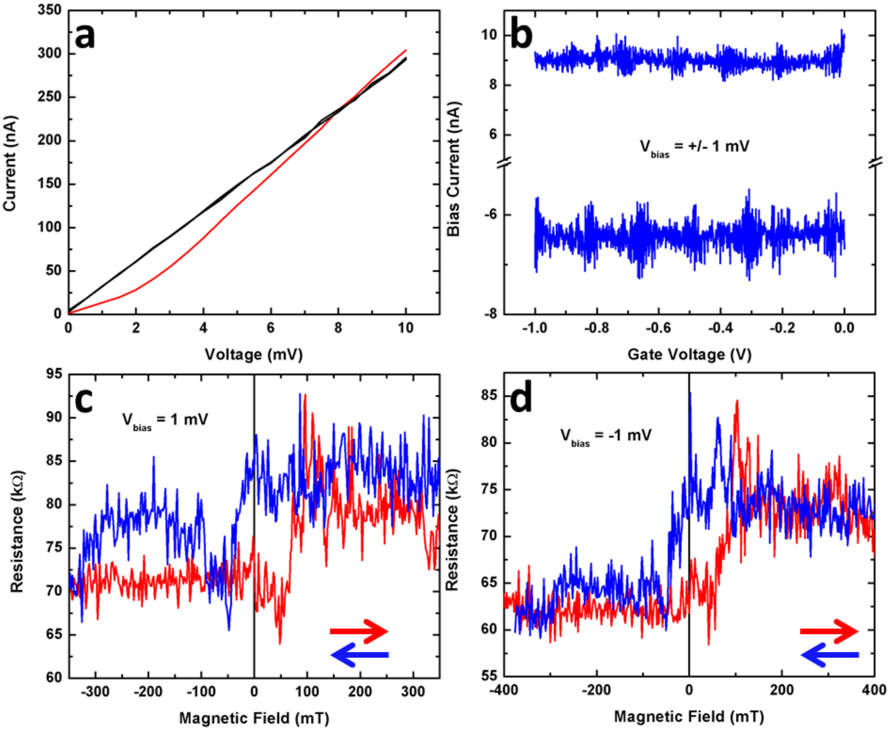

Figure 7.8: Electronic characterization and transport of the device CoPd5. (a) I-V curves taken at room temperature (black) and 4 K (red) showing the opening of a potential barrier. (b) Very little, asymmetric gate dependence indicates the presence of a metallic CNT with a strain-induced bandgap. (c) and (d) show MR curves taken at bias voltages of +/- 1 mV, respectively, where the red curve corresponds to a field sweep in the positive direction, and the blue in the negative direction.

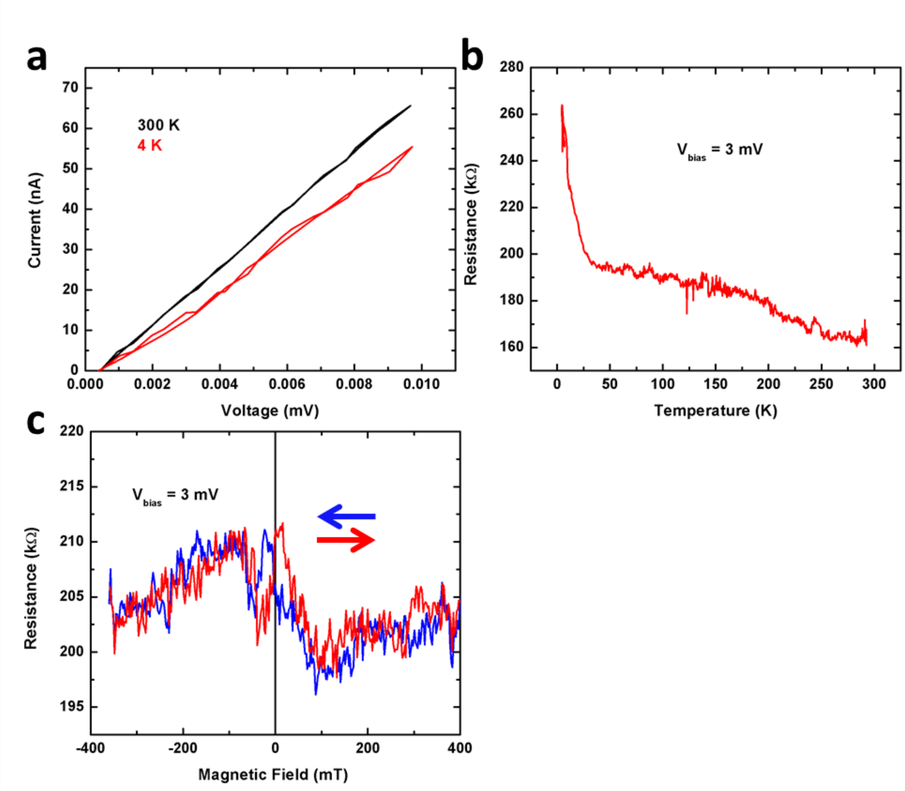

Figure 7.9: Electronic characterization and transport of the device CoPd6. (a) I-V curves taken at room temperature (black) and 4 K (red) showing a slight increase in barrier height at low temperature. (b) R vs. T plot further indicating the opening of a potential barrier. (c) MR plot taken at a bias voltage of 3 mV, where the red curve corresponds to a field sweep in the positive direction, and the blue in the negative direction.

Transport data for the subsequent device, CoPd7, is presented in figure 7.10. I-V characteristics at room temperature (black) and 4 K (red), are shown in (a), indicating an decrease in overall resistance at cryogenic temperatures, albeit with the opening of a potential barrier. This is thought to indicate the presence of a metallic CNT with a strain-induced band gap [66]. This idea is further confirmed by the R vs. T characteristics, plotted in (b). As helium is introduced into the cryostat and the temperature begins to lower, the resistance initially decreases, signifying a metallic device. At very low temperatures, beginning at approximately 30 K, the resistance begins to rise again, indicating the formation of a potential barrier. The device also exhibits reliable gate-dependence, plotted in (c). Although present, oscillations are fairly weak, and never approach zero current, which is perhaps a result of using a high bias $V_{bias} = 6$ mV. As the device had a high resistance, it was necessary to apply a larger bias to obtain a measurable signal, which possibly resulted in the lack of gate-dependence in the MR measurements.

An MR measurement with $V_{bias} = 9$ mV, is plotted in (d). The magnitude of MR, $\Delta R = 12\%$, is high, and the shape of the curve, although broader than that for the device shown above, showed two distinct peaks with H_c = -10 – -50 and 20 – 60 for negative (blue) and positive (red) sweep directions respectively. The shift in the positive direction is likely due to exchange bias, as the CoPd contacts in this device were uncapped. The measurement was reliable, and displayed no measurable gate dependence, likely due to the high bias used to obtain a measureable current in the high-resistance device.

Measurements performed on a final device, CoPd8, are presented in figure 7.11. I-V curves taken at room temperature (black) and 4 K (red) show the opening of a large potential barrier at low temperatures, in a device that was fairly low-ohmic at room temperature. A plot of R vs. T, shown in (b) further indicates the increase in resistance of several orders of magnitude between room temperature and 4 K. A gate sweep, performed with $V_{bias} = 15$ mV, shows the significant gate-dependence of the device in (c).

A magnetoresistance measurement performed at $V_{bias} = 15$ mV is shown in (d). Several bias voltages were attemped, and this resulted in the sharpest curve, with a magnitude $\Delta R = 6\%$. Narrow peaks were present between field H_c = -5 – -20 and 15 – 40 mT, for the negative (red) and positive (blue) sweep directions, respectively, and the measurement was highly repeatable at $V_{bias} = 15$ mV, although using a higher bias voltage resulted in increased background noise, and using a lower voltage resulted in wider MR. Furthermore, although only few measurements were taken, due to grounding issues of the back gate, using the gate to tune the barrier height influenced both the sign and magnitude of the MR. Figure 7.11(e) shows a measurement performed with V_{bias}= 15 mV, as in the measurement shown in (d), but with a gate voltage $V_{gate} = -1$ V. According to the gate sweep presented in (c),

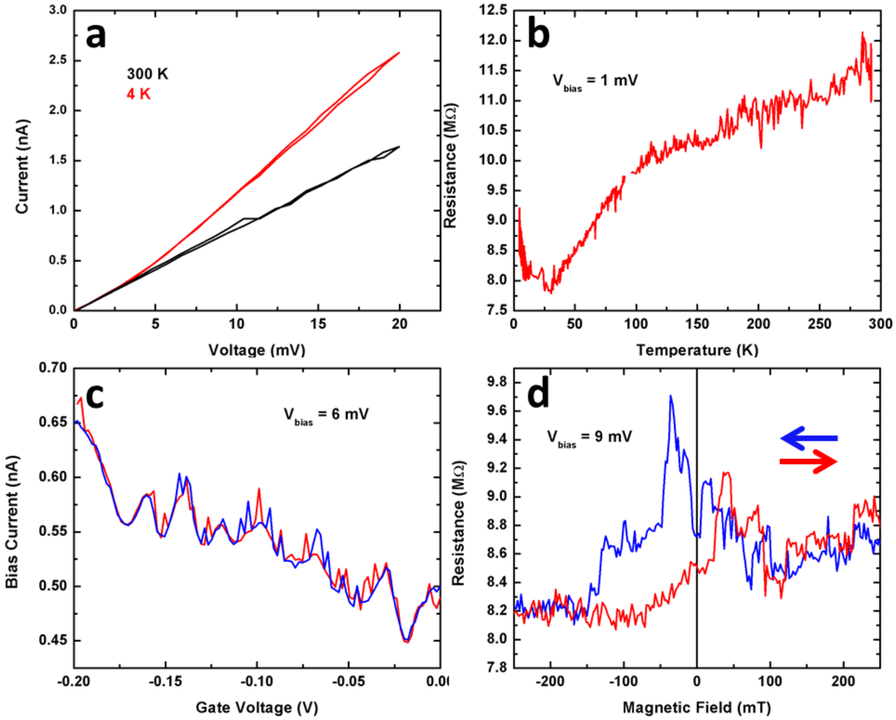

Figure 7.10: Electronic characterization and transport of the device CoPd7. (a) I-V curves taken at room temperature (black) and 4 K (red) showing the opening of a potential barrier. The device displays a significant contact resistance at room temperature. (b) R vs. T plot showing the initial decrease of resistance, followed by an increase, indicating a metallic CNT with a strain-induced band gap. (c) Small gate-dependent fluctuations confirm the existence of a potential barrier. Red and blue curves correspond to gate sweeps in the positive and negative direction, respectively. (d) MR curves taken at a bias voltage of 9 mV, where the red curve corresponds to a field sweep in the positive direction, and the blue in the negative direction.

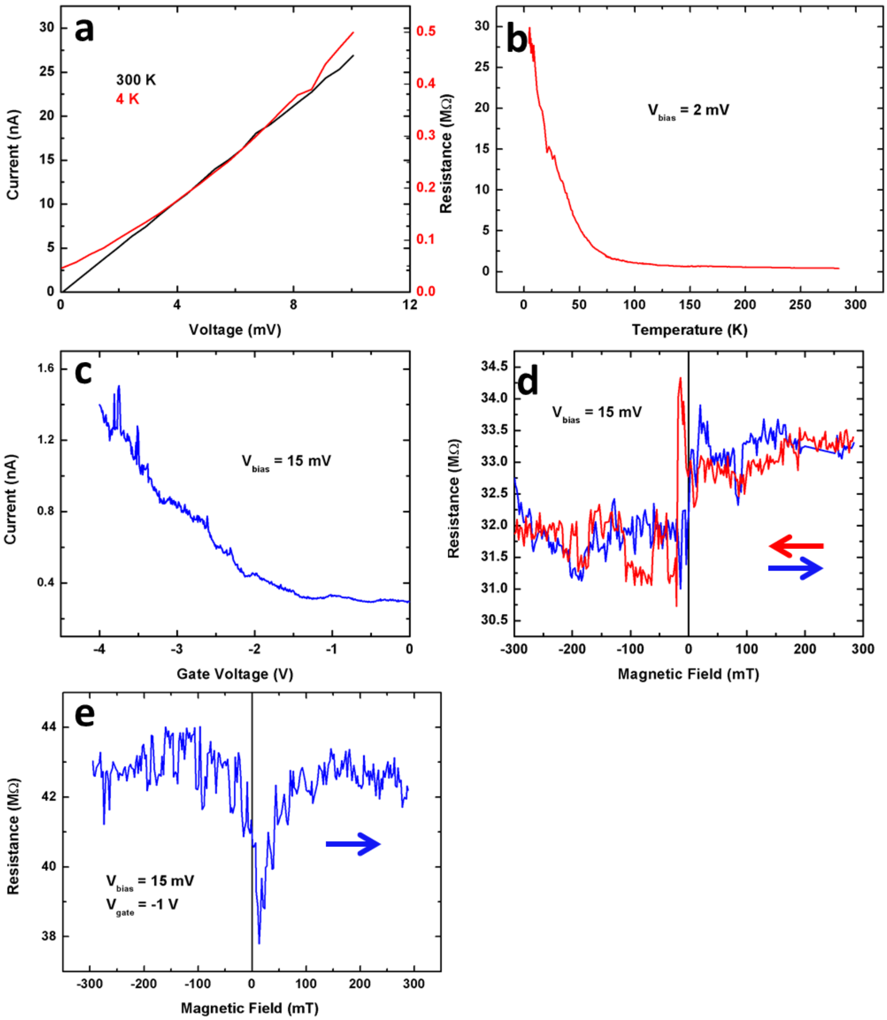

Figure 7.11: Electronic characterization and transport of the device CoPd8. (a) I-V curves taken at room temperature (black) and 4 K (red) showing the opening of a potential barrier. The significant offset in the 4 K measurement is an artifact of the measurement. (b) R vs. T plot further indicating the presence of a semimetallic CNT. (c) Gate-dependence showing the lowering of the Schottky barrier with applied back gate. (d) MR curves taken at a bias voltage of 15 mV, where the red curve corresponds to a field sweep in the negative direction, and the blue in the positive direction. (e) MR curve of a positive field sweep with an additional V_g = -1 V. The slight asymmetry in magnetic field is attributed to the positioning of the sample.

this should act to reduce the potential barrier in the device. The resulting curve, shown only in the positive sweep direction, shows a negative MR of approximately ΔR = -9%, with the lower value indeed corresponding to a reduced tunnel barrier. As expected, the application of a gate voltage has no influence on the position of the peak.

7.2.3 Electronic control and temperature dependence

Electronic control of magnetoresistance

The electronic state of the sample also strongly influences magnetoresistance. As discussed in chapter 6, use of a back gate can influence MR, affecting both the magnitude and possibly the sign. This effect has been shown in CNTs contacted with Py [30], and NiPd [25, 26, 99]. In this work, sweeping of a back gate voltage was shown to influence CoPd-contacted CNTs as well, albeit to a lesser extent. For example, the device CoPd3 required the use of a back gate in order to lower the Schottky barrier enough to measure MR, and MR measured on CoPd8 was shown to change both magnitude and sign as the gate was swept to reduce the Schottky barrier. However, most devices successfully showing magnetoresistance had fairly low resistances, and showed only little back gate dependence. This could be a result of the high transparency of Pd-based contacts to CNTs[6]. Another possible explanation is that the CNTs used in this work were grown at relatively high temperatures ($T_{growth} \geq 900$ °C), resulting in largely double and MWCNTs. The probability of one metallic wall influencing transport is therefore high, resulting in the low gate-dependence.

Another electronic factor that has been shown to affect MR is the applied bias, and it has previously been shown that lowering the applied bias leads to a maximum in MR [23]. For CoPd-contacted CNTs, the bias required to obtain MR appears to be extremely sample-specific. However, when performing measurements, most samples displayed the optimal MR when the bias voltage corresponded to a current on the order of 1-10 nA.

Figure 7.12(a) plots the MR versus current through the device for several devices measured in this thesis, including those discussed in the above section. The highest MR clearly occurs at around 1-5 nA, and the effect strongly decreases at higher currents. Data measured with a higher current through the device than that plotted here yielded no MR. The two outlying points, showing extremely high MR are not fully understood. However, they are an example of device specificity, and it should be noted that both measurements resulted in minor-loop switching, rather than complete MR. The zero resistance point at low current, which is included for

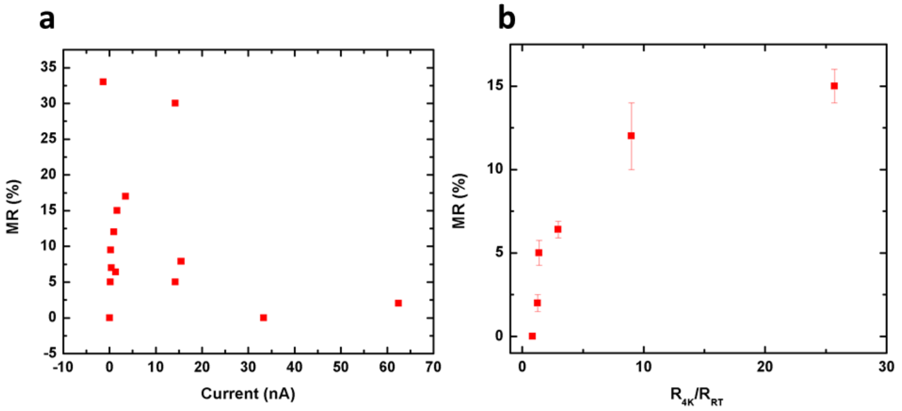

Figure 7.12: (a) Magnitude of local magnetoresistance versus current through a CNT. As large Schottky barriers were present in most devices at 4 K, current was calculated using the applied bias voltage and the resistance at that voltage. (b) MR versus change in resistance for a series of devices. Error bars represent deviation between the results of two measurements.

completeness, resulted from the device CoPd4, where no tunnel barrier formation or MR was observed.

The dependence of MR on current through the device is likely due to the fact that a low current results from the formation of a strong tunnel barrier. As the MR is thought to be tunneling magnetoresistance, a higher barrier forces the entire current to tunnel through the barrier, as opposed to the case of a low tunnel barrier, which some electrons would have high enough energy to overcome. Tunneling-only transport conserves spin and would therefore lead to higher spin polarization of the current, and a correspondingly higher MR. This is confirmed by figure 7.12(b), which plots magnetoresistance versus R_{4K}/R_{RT} for a series of devices. Here, it is shown that a high increase in resistance with temperature, which is related to the strength of the Schottky barriers in the device, leads to a strong increase in the magnitude of the local magnetoresistance. This strongly confirms the above statement that achieving optimal MR is extremely device specific, based on the electronic environment presented in each device, with optimal devices having stable ohmic contacts, but developing a strong potential barrier.

Temperature-dependent magnetoresistance

As TMR measurements rely on the formation of a tunnel barrier between the CNT and the ferromagnetic contact, which occurs spontaneously at low temperatures, a temperature dependence of the MR is expected. Previous work has shown that SWNTs contacted with Fe exhibit temperature-dependence, with respect to both the shape and the magnitude of MR [77]. According to [105], the magnitude of TMR should decrease exponentially as temperature increases, following the equation:

$$\frac{\Delta R}{R_p} \propto 1 - \exp\frac{-E_m}{k_B T} \tag{7.1}$$

where E_m is the energy needed to overcome the potential barrier, which agrees with the data presented in [77].

Temperature-dependent MR data taken on the device CoPd2 is shown in figure 7.13. Data was taken at a temperature range between 3.4 K and 75 K using a constant bias V_{bias} = 2 mV, and results for negative and positive field sweeps are plotted separately in (a) and (b) for clarity. The overall resistance is shown to decrease with increasing temperature, as would be expected for a semimetallic CNT or a narrow-band gap metallic CNT.

A strong temperature dependence is observed, with the TMR signal appearing to become lower and more narrow as temperature increases. The decrease in magnitude is expected, as the tunnel barrier loses strength at increased temperatures. It should be noted that the background noise in measurements also increases due to thermal fluctuation at higher temperatures, and it is possible that a small ΔR still exists at 75 K, but is lost in the noise.

The change in width of the TMR signal, corresponds to a changing difference in coercive fields of the contacts from ΔH_c = +/- 13 mT at 3.4 K to $\leq$ 4 mT at 50 K. This corresponds well to the temperature-dependent SQUID data presented in chapter 4, which shows that at 50 K, magnetostatic coupling strongly influences the magnetization of nanocontact arrays, resulting in a lowered coercive field. This finding, showing a strong magnetoelastic effect in a capped sample, indicates that strain induced at the metal-substrate interface has a large influence on magnetostriction. It is also possible that at higher temperatures, higher energy allows fabrication-induced pinning sites to be more quickly overcome, further decreasing the coercive fields of the contacts, however, this would be extremely device specific.

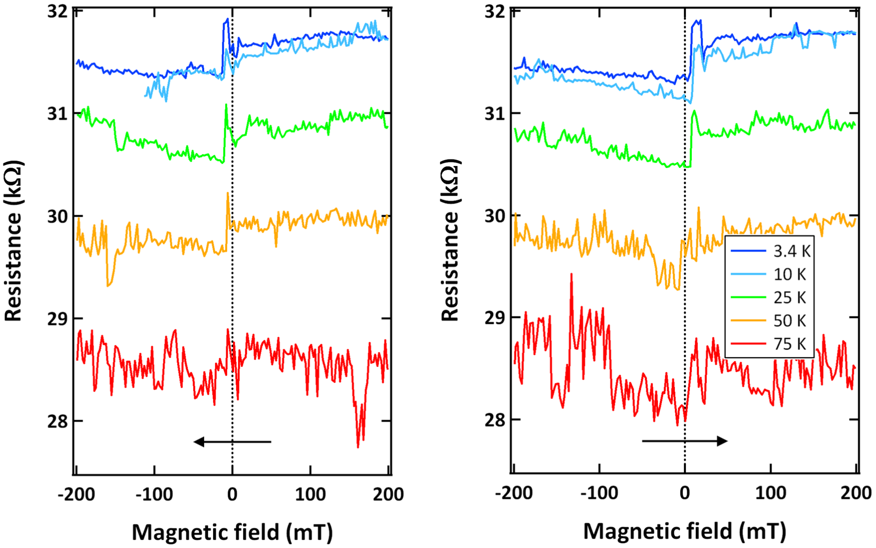

Figure 7.13: Temperature-dependent magnetoresistance measurements performed on device CoPd2 at temperatures ranging from 3.4 - 75 K. For all measurements, V_{bias} = 2 mV and V_{gate} = 0. Results are plotted separately in the (a) negative and (b) positive sweep directions.

7.2.4 Nonlocal measurements

The results presented above show that when properly designed, CoPd contacts to CNTs result in stable, sensitive TMR. However, with local measurements, it is possible to simultaneous measure several spurious effects, such as AMR, TAMR, or the magnetocoulomb effect, as well as other ohmic contributions in addition to spin transport. Therefore, nonlocal measurements are performed, in order to separate a pure spin current and offer definite proof of spin injection and detection.

A first attempt at a nonlocal measurement was performed on the device CoPd9. Although this device nominally contained four terminals, a four-terminal nonlocal MR measurement yielded no results. Additionally, two-terminal measurements indicated that at least one of the leads was unable to switch polarization, although electrical characterization showed all contacts to have a similar, high-ohmic contact, resulting in a resistance on the order of 50 MΩ.

Three-terminal nonlocal MR measurements were more successful, resulting in a magnetotransport signal. Figure 7.14 is a plot of one normalized measurement, with an applied bias $I_{bias} = 50$ nA. The setup of the sample, showing which contacts acted as spin injector and detector, is shown in figure 7.15(a). Rather than the negative peaks that are signature of nonlocal MR (see chapter 5), the data shows a more complicated transport consisting of a small negative peak in each direction overlaid on a larger hysteresis-like minor loop. Multiple measurements resulted in MR curves of a similar shape. The inset in figure 7.14 is a zoom-in of the negative peaks present at small magnetic fields. The peaks presented here are averaged over five measurements, in order to reduce noise. Here, it is clearly observed that although they are small, the peaks stand out from the noise and are definitely a transport feature of the device. A slight broadening of the peaks is observed due to thermal cycling between the measurements.

As discussed in chapter 5, although the measurement in a three-terminal setup occurs outside the direct path of applied current, the shared electrode makes the nonlocal nature of the measurement questionable. In materials such as Si and GaAs, where the band structure is known, it is possible to determine the effect of the shared lead based on whether the contact material forms deep-level impurities to the material [106]. In the case of CNTs, however, the band structure is highly sample-specific, and may even be dependent on external factors, such as temperature, within one device. Furthermore, doping of the CNT with contact material is not expected to occur, as it may in the case of Si and GaAs. It is therefore difficult to say whether a three-terminal measurement in a CNT-based device completely removes local components of MR.

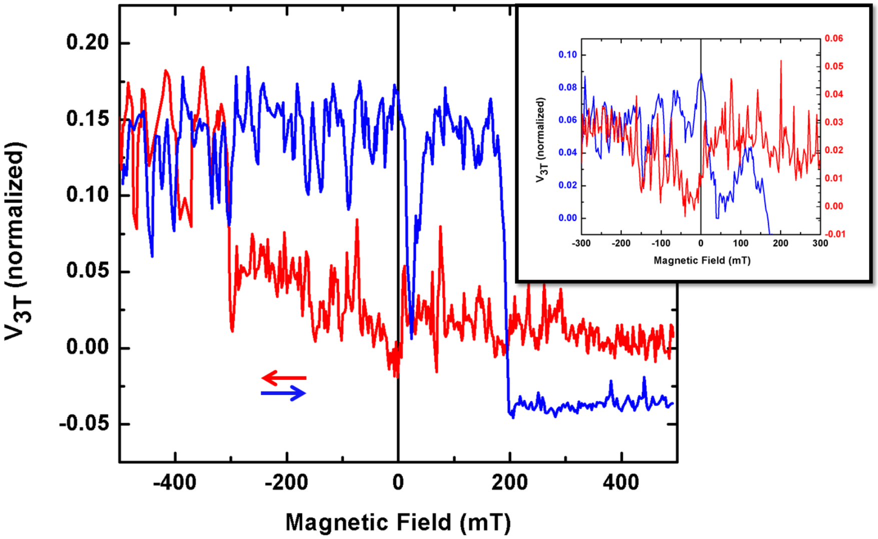

Figure 7.14: A nonlocal three-terminal MR measurement performed on the device CoPd9. Positive and negative sweep directions are indicated by the blue and red lines, respectively. A constant bias I_{bias} = 50 nA was applied. Inset: A zoom-in of the low-field transport region, in which five curves were averaged to improve the signal-to-noise ratio. The background voltage has been normalized.

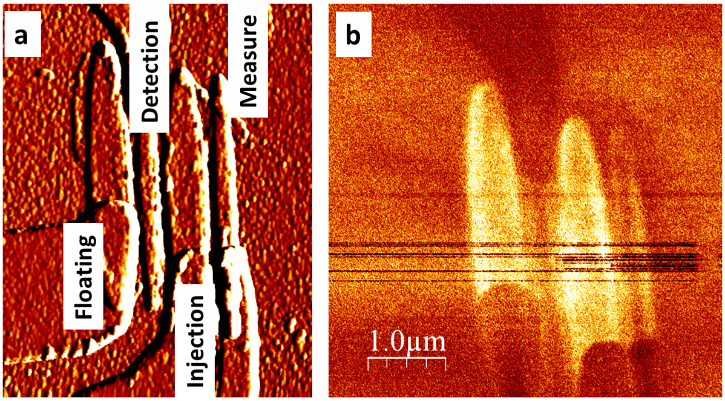

Figure 7.15: Characterization of device CoPd9 via (a) AFM and (b) MFM. The roughness in topologiy is expected due to exposure to multiple cooling cycles. The remanent-state MFM image shows a significantly lower magnetization of the narrow contacts.

Judging by the shape of the MR curve, it appears to consist of both local and nonlocal components which comprise the different features. The negative dips in MR occurring at approximately 15 – 35 mT in the positive (blue) sweep direction and 5 – -10 mT in the negative (red) sweep direction, resemble a typical nonlocal spin-valve signal. The occurrance of this feature is shifted in the positive direction, likely due to a slight misalignment of the sample within the magnetic field. The appearance of a minor loop in a three-terminal measurement is commonly thought to be an effect of local MR [107]. This feature occurs only at very high fields, another indication of possible pinning. Furthermore, the changes in resistance for the two effects are measured to be $\Delta R = 15\%$ and $\Delta R = 2\%$ for the minor loop and negative dips, respectively, which are of similar order of magnitude to local and nonlocal MR previously recorded on a single device [4].

In order to further understand the magnetic behavior of the device, MFM characterization was performed. Figure 7.15(a) shows the topological structure of the device as imaged via AFM. The roughness is likely induced by the multiple thermal cycles the sample was exposed to during measurements. However, the contact structure remains intact, and a further zoom of the sample (not shown here) shows that the nanotube is still present. The labels in the image indicate which contacts were used in the measurements. Bias was applied between the injection and measurement contacts, and voltage was measured between the injector and detector contacts. The fourth contact was kept on a floating bias throughout the measurement.

Figure 7.15(b) shows the magnetic image of the device. It should be noted that in this sample, only 20 nm of CoPd were deposited, in contrast to the 65 nm thick Au/Ti leads. Therefore, although the CoPd under the leads is still magnetic, the stray field is scattered before it can be detected via MFM. The image clearly shows a magnetic signal from all four contacts, in what appears to be a few-domain structure. However, a much stronger signal is observed in the wider contacts. It is therefore likely that the polarization reversal in the narrow contacts is influenced by the higher magnetization of neighboring wider contacts. The detector contact, which is surrounded by two such wider contacts, is especially vulnerable. The reason for the narrow contacts having lower magnetization is unknown. One possibility is that metallization into such high aspect ratio structures resulted in higher surface roughness, weaking the in-plane magnetization.

This magnetic environment would strongly effect the transport data. The shifting of the local signal toward the negative direction, which is strongly observed in negative field sweeps, is likely the result of the magnetization of the narrow contacts being influenced by that of the wider ones, specifically the detector contact being affected by the magnetization of the fourth, floating contact. The additional local effect could have many causes, but one hypothesis is that the narrow measurement contact is pinned, or simply difficult to switch due to low magnetization. At high magnetic fields, enough energy is present to switch the magnetization of the contact, which then influences the transport throughout the device.

While the three-terminal data is unlikely to consist solely of nonlocal data, the shape of the curve indicates that at least part of the signal represents spin-valve behavior. Therefore, although further studies are needed to determine polarization or spin lifetime, this device appears to indicate the definite ability of CoPd contacts to inject and detect spin in a CNT channel. Furthermore, characterization of the device via MFM offers a plausible explanation for the multiple features present in the MR data.

In order to further prove spin injection, Hanle measurements were performed on the same device, in the same 3T configuration. Measurements performed using a bias current $I_{bias} = 10$ nA are shown in figure 7.16. The data, which was recorded for the spin injector and detector being aligned in parallel only, may be fitted with a Lorentzian peak (blue in the figure), and the magnetic field at the full width half maximum of the peak is measured to be approximately 5.2 mT.

Following Equations 5.9 and 5.10, and taking the g-factor $g = 2$ for a CNT in a perpendicularly applied magnetic field [97], we obtain a spin lifetime of $\tau_s = 1.1$ ns in the nanotube channel. This value is lower than what is theoretically thought to be possible for a CNT [91]. Experimentally, however, while Hanle measurements on CNT-based devices have not been previously reported, the spin lifetime is on target with that commonly experimentally observed in graphene[108]. There are

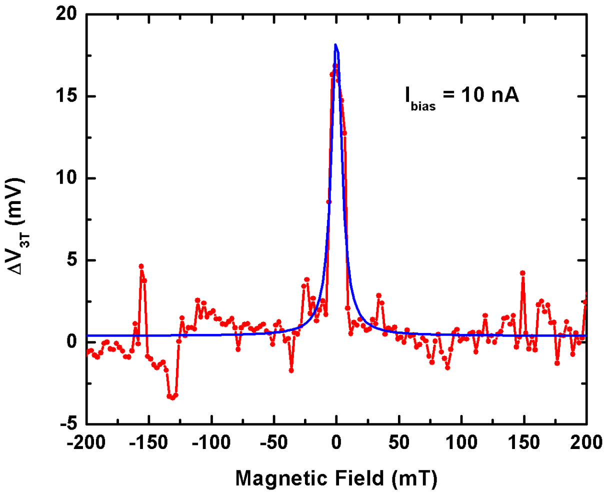

Figure 7.16: Hanle measurement performed with injector and detector contact aligned parallel. A Lorentzian peak fitting gives a FWHM corresponding to a spin lifetime τ_s = 1.1 ns. Measurements were taken at approximately 4 K, and a bias I_{bias} = 10 nA was used. Red points correspond to measured data, and the blue line is a Lorentzian fit. The data has been normalized.

several possible explanations for the lower spin lifetime. One possibility is that spin orbit coupling plays a larger role than expected. As shown in Table 7.1, the diameter of the CNT in this device is 1.5 nm. Although it is impossible to tell for sure without transmission electron microscopy, this is likely a double-walled CNT with an inner tube with a diameter of approximately one nm or less. Due to the effects of extreme curvature, spin orbit coupling has been shown to be nonnegligible in such a small CNT, despite the fact that it is almost zero for larger CNTs [18]. Another possible explanation involves the interaction of spin current in the CNT with charge traps, which are known to be present in the SiO_2 substrate [109]. Both of these sample-specific factors could contribute to a lower spin dephasing time in the device.

7.3 Conclusions

While CoPd is in many ways an ideal contact for a CNT-based spintronics device, transport measurements prove that magnetoresistance in such devices is extremely dependent on both contact geometry, and the band structure of the incorporated nanotube. As expected due to precharacterization of CoPd, the lateral dimensions of the contacts strongly influenced MR, with large unshaped contacts displaying complex magnetoresistance. However, small changes in the thickness of contacts also served to drastically alter MR, with 40 nm thick contacts resulting in broad curves while 10 nm thick contacts led to abrupt, sensitive switching. Studying several devices with contacts of the same shape led to the conclusion that MR is also highly device dependent, most likely due to the diverse electronic character of CNTs. Optimal results were achieved in samples with overall resistances on the order of approximately 100 kΩ–1 MΩ, in which a large potential barrier was opened. Devices with lower resistance likely lacked the potential barrier necessary for TMR to occur, while devices with higher resistance were either poorly contacted, or required such a high bias that the signal-to-noise ratio becomes unsustainable.

The % TMR of a device was shown to depend heavily on the strength of the tunnel barrier formed at low temperatures. While the dependence of TMR on tunnel barrier strength has been shown for tunnel junctions [104, 76], based on insulator material and thickness, it has not yet been reported for CNT-based devices, where an intrinsic tunnel barrier develops, depending on the chirality of the incorporated CNT. The ability to separate CNTs based on their chirality, which is presently being investigated, would therefore likely improve the reliability in CNT-based spin-valves [110]. Diameter of the CNTs was not shown to strongly influence MR. Temperature-dependence was recorded, and showed optimal MR at 4 K with a lowering magnitude as the temperature was increased, eventually disappearing at 75 K. This finding further indicates that the presence of a potential barrier enhances MR, which is expected to be tunneling magnetoresistance [21].

Finally, first nonlocal measurements, performed on a three-terminal device, indicated the occurrance of spin injection and detection by CoPd into a CNT channel. The magnetic behavior of the contacts prohibited the implementation of four-terminal measurements and influenced the transport properties of the device, however the shape of the curve confirmed spin valve-like behavior. A Hanle measurement indicates clear spin precession through the CNT, with a fitted spin lifetime $\tau_s = 1.1$ ns, which is a reasonable value. While further data, such as a 4-terminal measurement, to determine current polarization, or a Hanle measurement comparing results from electrodes aligned parallel and antiparallel, would be useful to further understand the system, this is a definite proof that CoPd-contacted CNTs exhibit spin valve behavior, including injection, detection, and precession.

8 Conclusions

A typical carbon nanotube exhibits 1-dimensional, quasi-ballistic transport, and is expected to have only low spin-orbit coupling [1, 2] and hyperfine interactions, suggesting a long spin-dephasing length. Additionally, the high aspect ratio and intrinsic formation of a tunnel barrier at low temperatures facilitates the integration of CNTs into devices. The challenge is finding an optimal material for spin injection and detection into a nanotube, as permalloy and 3-D transition elemental FMs have been shown to form poor electronic interfaces with CNTs, leading to unstable magnetotransport[4, 23, 77].

Recent research has focused on diluted ferromagnetic alloys as FM contacts to CNTs. FePd, which has a composition-dependent crystal structure, was deemed unsuccessful as a contact material, as it was impossible to remove the effects of a large out-of-plane component to the magnetization[5]. NiPd has been more successful, showing a clear switching signal, but only when a field is swept transverse to the contact direction [26, 27]. This work focused on establishing CoPd-contacted CNTs. In many ways, CoPd is an ideal contact material for CNT-based spintronics applications. The palladium component is known to form transparent contacts to CNTs [6, 111], while the cobalt component contributes a high polarization, which is expected to remain even when alloyed with large amounts of Pd [7]. However, the complex magnetic structure of CoPd requires a careful analysis in order to determine under which conditions reliable spin injection and detection can be achieved.

8.1 Summary of main results

This work encompassed the structural and magnetic characterization of a series of CoPd alloys and geometries, and the implementation into CNT-based spin-valve devices. Magnetotransport was recorded in many CoPd-contacted devices, in addition to devices contacted with permalloy as a reference. The main results are as follows:

- Extended films of CoPd display a complex magnetic structure which is improved as the composition shifts toward more cobalt and the thickness is decreased. Room temperature magnetization is further improved with the fabrication of nanostructures, resembling contacts. When the geometry is limited in all dimensions, one to two in-plane magnetic domains are present.

- CoPd nanostructures exhibit a complicated temperature-dependent magnetization in which the hysteresis becomes less square at intermediate temperatures. This is attributed to the magnetoelastic effect due to strain at the interfaces of CoPd with the substrate and with the native oxide. Careful control of the geometry, especially the in-plane aspect ratio, ensures the prevalence of shape anisotropy in determining the easy axis of magnetization. At 4 K, the magnetization is square, indicating abrupt polarization reversal, which is favorable for spintronics applications.

- In both CoPd and Py-contacted samples, controlling contact geometry led to higher sensitivity of switching, and to a higher magnitude of ΔR. This occurs because single-domain contacts switch abruptly at the coercive field, rather than relying on domain-wall rotation. The higher ΔR is the result of more in-plane polarization.

- CoPd leads to TMR that is at least as high as that observed in Py-contacted devices.

- Local magnetoresistance performed on multiple devices showed reproducible TMR. The shape and magnitude of the signal was highly sample-dependent. The shape of the magnetoresistance could often be attributed to fabrication-induced defects. All factors contributing to magnitude of the TMR are not yet understood, but may be related to spurious effects, such as AMR or the magneto-Coulomb effect.

- CoPd-contacted CNT-based devices exhibited a temperature-dependent MR, in which the highest values were observed at 4 K. As the temperature was increased, MR peaks became smaller, and the noise level of the measurement increased, making it difficult to determine the exact magnitude and switching fields. The signal was lost at 75 K. This is consistent with the formation of a tunnel barrier at low temperatures, indicating that tunneling magnetoresistance is occurring.

- Bias-dependence of the magnetoresistance was also observed, although extremely sample-specific. In general, MR was optimized when a voltage was applied that generated 1-10 nA of current, and the most successful devices tended to have resistances ranging from 100 kΩ to 1 MΩ. Devices with higher resistances required the use of a high bias, which resulted in a high signal-to-noise ratio, making it difficult to detect a signal. Devices with lower resistances didn't exhibit tunnel-barrier formation, making TMR impossible to achieve.

- The strength of the tunnel barrier formed at low temperatures, as defined by R_{RT}/R_{4K}, has a strong effect on ΔR, with high tunnel barriers leading to the highest TMR. This is likely due to the fact that a strong tunnel barrier ensures a high spin polarization of the current passing through the device.
- Nonlocal measurements were performed in a three-terminal configuration. The results showed both a local contribution resembling a minor loop, and a nonlocal contribution consisting of negative MR. This is the first definite proof of spin injection and detection by CoPd in CNT-based devices. Hanle measurements confirm spin precession and give an approximate spin lifetime $\tau_s = 1.1$ ns.

These results highlighted that CoPd does form stable low-ohmic contacts to CNTs which are highly polarized. The material has a complex magnetic behavior which is controllable via geometry manipulation. With defined CoPd nanostructures as contacts, stable, highly field sensitive MR is observed in CNT quasi spin valves. While the two-terminal results could be largely enhanced by electronic effects, nonlocal results clearly indicate spin injection and detection by CoPd contacts.

Unlike NiPd contacts, CoPd exhibits an easy axis in-plane parallel to the long axis of the contact. This is at least partially due to the reduced dimensions of contact used in this work resulting in less internal strain, allowing shape anisotropy to be the dominant factor in determining the preferential magnetization direction. This work is also set apart by the electronic regime in which experiments are conducted. Transport measurements in CNT-based devices are often conducted at subkelvin temperatures to increase stability. However, such low temperatures may effect magnetoresistance by suppressing an ohmic background component that is present at higher temperatures[25]. The measurements in this work were all performed in a regime where the device acts as an opening transistor [30]. In this regime, which is more realistic for eventual applications, it is possible to effectively study both ohmic and magnetic contributions to magnetoresistance.

When properly dimensioned, CoPd is therefore an excellent material for contacts in a CNT quasi-spin valve. Published results may be found in references [29, 30, 31]

8.2 Future work

In order to gain understanding of and optimize spin transport in CoPd-contacted CNTs, several further experiments would be beneficial. Nonlocal measurements are crucial in determining spin injection. While three-terminal measurements are effectively nonlocal, one electrode is shared between the injection and detection path. Therefore, a local effect may be induced, as was indeed the case in this work. In order to completely eliminate this effect, four-terminal measurements must be performed [15, 94].

The three-terminal measurements presented in chapter 7 are a clear indication of spin injection. However, due to the large local contribution and noise level, it is impossible to determine any parameters such as spin dephasing time or length. It is only possible to determine that the detection contact in that specific device was located within the spin dephasing length. Such information is important for designing future devices. In contrast to three-terminal measurements, measurements performed on devices with four terminals would exhibit only nonlocal magnetoresistance resulting from injection of a pure spin current. Data may be extracted from nonlocal magnetoresistance measurements to determine the polarization of the injected current. This is valuable, as polarization of CoPd of varying alloys is the single most important factor in determining the effectiveness of spin injection and the expected magnitude of TMR. Preparation of samples with four-terminal configurations is currently underway and will likely result in more concrete information about spin injection by CoPd in CNTs.

In addition to nonlocal magnetoresistance measurements, Hanle measurements are an accurate means of determining spin injection. As briefly defined in chapter 5, Hanle measurements are performed similarly to magnetoresistance measurements with the important difference that the magnetic field is swept out-of-plane to the sample after an in-plane magnetization is used to saturate the contacts. During the out-of-plane field sweep, polarized current diffuses between the injector and detector, continuing to propagate until the spin dephasing time is reached. The spin dephasing time, τ, may therefore be extracted from Hanle measurements, as was done in this work. It is debatable, however, whether three-terminal and four-terminal measurements give the same value for τ. This appears to depend on both the contact and channel material, and is not currently being studied in CNT-based systems. As a direct proof of spin accumulation with the potential to determine several useful parameters for spin injection, performing nonlocal 4-terminal Hanle measurements would yield extremely beneficial results. Additionally, in this work, only a sweep with the spin injector and detector aligned parallel was performed. A four-terminal Hanle measurement with the electrodes aligned antiparallel should give a negative peak, and more information regarding spin lifetime may be obtained from the position where the peaks from parallel and antiparallel aligned electrodes meet. Currently, a rotatable sample holder is being built in order to perform such measurements.

Finally, in order to move beyond research into eventual application, TMR must occur beyond 4 K, preferrably at room temperature and beyond. Until now, research has largely made use of the intrinsic tunnel barrier CNTs develop at low temperatures. To work at elevated temperature, however, a tunnel barrier must be introduced. Typical oxide tunnel barriers include MgO and Al_2O_3, and are often incorporated into spintronics devices using graphene or semiconducting nanowires. Additionally, a new family of materials, spin filters, is currently being developed [112, 113] Such materials, including EuO and EuS, both act as an insulating tunnel barrier and include the further function of being highly spin selective. Although not all materials currently work at room temperature, much work is currently being performed to learn about spin filters and optimize their functionality. Incorporation of such materials into CNT-based spintronics devices would potentially introduce a highly effective tunnel barrier at elevated temperatures, further enabling the eventual integration of CNTs in application.

Appendix

A Catalyst preparation

Table A.1 gives a list of the materials used in this work to make a catalyst for the CVD growth of carbon nanotubes. The materials include ferric nitrate nonahydrate, $Fe(NO_3)_3{\cdot}9H_2O$, which contains the active material for the iron-based catalyst, and Al_2O_3, which acts as a scaffolding material, holding the other components of the catalyst together in islands. Additionally, $MoO_2(acac)_2$ is thought to improve growth by attracting amorphous carbon, and therefore keeping the active catalyst free for a longer period of time [114]. Increasing the amount of $MoO_2(acac)_2$ therefore leads to higher nanotube yield. The dry materials are put into solution in methanol and sonicated for 2 hours. Before each use, the catalyst is sonicated for 30 minutes and left to settle for 20 minutes, in order to prevent results of demixing.

Table A.1: Components of catalyst for CVD growth of CNTs

Material	Quantity	Purpose
Al_2O_3	30 mg	scaffold material
$Fe(NO_3)_3{\cdot}9H_2O$	40 mg	supplier of active iron catalyst
$MoO_2(acac)_2$	4-10 mg	keep amorphous carbon from active catalyst
Methanol	30 ml	solvent

B Supplementary information for electron beam lithography

Electron beam lithography (EBL) was performed using a Leica EBPG 5000 Plus e-beam writer. A standard acceleration voltage of 50 kV was used for all processes in this work, but the current, dose, beam size and step size were considered for each structure. Table B.2 lists the parameters used for writing various structures in the course of this work. To determine these parameters, dose tests were conducted using test structures. For positive structures, this was accomplished prior to the start of this work and is published in [115]. The process for designing negative marker structures was determined during this work.

The most common resist used for EBL is the polymer polymethylmethacrylate (PMMA). Different molecular weights of PMMA, as well as different concentrations of PMMA in solution, may be used, and the choice of PMMA strongly influences processing parameters. For the samples processed in this work, both negative (etched) and positive (deposited metal) structures are needed. For negative markers, 7% 600K molecular weight PMMA in ethyl lactate solution was used (AR-P 669.07 from Allresist GmbH). The relatively high concentration ensured a thick layer after spin-coating, which was necessary to protect the substrate from damage during the etching process. For positive structuring, a double layer of 4% 200K PMMA (AR-P 649.04) and 2% 950K PMMA (AR-P 679.02) was used. Using such a bilayer has the result that the lower layer, which has a lower molecular weight, is more sensitive to the electron beam, and a slightly wider part will be developed and removed than from the upper layer. This creates an undercut in the resist layer, which is used to ensure a clean metal deposition without the formation of sidewalls.

In general, larger structures require smaller doses due to the proximity effect, which describes the spread of energy when an electron beam is directed in one position. Smaller structures, in which fewer neighboring sites are being exposed, tend to require larger doses. A smaller beam step size results in a higher resolution. Therefore, it is necessary to use the smallest possible step size, 2.5 nm, for the fine marker structures, which need to accurately be placed over the nanotubes, but a much higher step size can be used for structures such as the bonding pads, where accuracy is less critical. The current is related to the beam step size.

Table B.2: Parameters used in electron-beam writing of various stages of sample fabrication.

structure	size (μm)	beam step size (nm)	current (nA)	dose (μC/cm^2)
alignment markers	20–800	12.5	10	265
AFM markers	0.5–1	12.5	10	345
Bonding pads	6–200	50	150	280
Coarse leads	0.2–4	2.5	1	500
Fine leads	0.03–0.2	2.5	1	750

Figure B.1 shows the process steps for a standard metallization procedure using EBL. First, the substrate is spincoated, written, and developed, as described above. Spin coating parameters of 60 seconds with no ramp at 3000 rpm were used for all positive processes in this work. In step (b), EBL is performed and the exposed resist is developed, creating a mask for the subsequent metal deposition in (c). Finally, the PMMA and additional metal are removed in acetone.

A similar process is used for selectively placing catalyst on the substrate. In this case, the sample is written to include small square patches between selected AFM markers. The catalyst solution may then be pipetted onto the substrate, accounting for the metallization step in Fig.B.1(c), which is then baked to remove the solvent. Finally, sonicating the sample in acetone removes the PMMA, including all catalyst particles that are not on the sample surface. Providing the sonication is relatively weak, catalyst will adhere to the substrate due to van der Waals attraction.

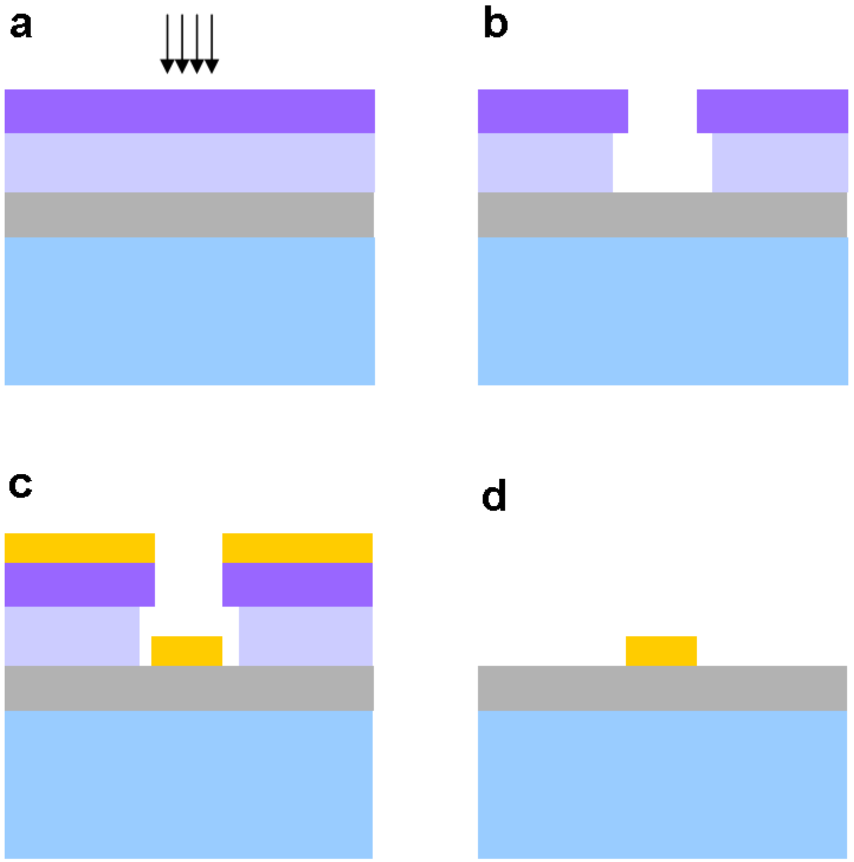

Figure B.1: Illustration of the metal lift-off technique used in this work. Standard processing steps include (a) spincoating two layers of PMMA (purple) onto a silicon substrate (blue) with a gate oxide (gray), (b) exposing and developing the resist, (c) metallization (gold), and (d) liftoff in acetone.

Bibliography

[1] T. Ando, *Journal of the Physical Society of Japan* **69**, 1757 (2000).

[2] T. S. Jespersen, K. Grove-Rasmussin, J. Paaske, K. Muraki, T. Fujisawa, J. Nygard, and K. Flensberg, *Nat Phys* **7**, 348 (2011).

[3] H. Vinzelberg, B. Zhao, I. Mönch, J. Schumann, and C. M. Schneider, *J. Magn. Magn. Mater.* **290-291**, 1100 (2004).

[4] N. Tombros, S. J. van der Molen, and B. J. van Wees, *Phys. Rev. B* **73**, 233403 (2006).

[5] D. Preusche, S. Schmidmeier, E. Pallecchi, C. Dietrich, A. K. Hüttel, J. Zweck, and C. Strunk, *Journal of Applied Physics* **106**, 084314 (2009).

[6] A. Javey, J. Guo, Q. Wang, M. Lundstrom, and H. Dai, *Nature* **424**, 654 (2003).

[7] K. Buschow, P. van Engen, and R. Jongebreur, *Journal of Magnetism and Magnetic Materials* **38**, 1 (1983).

[8] W. Thompson, *Proc. Roy. Soc.* **8**, 546 (1857).

[9] T. McGuire and R. Potter, *Magnetics, IEEE Transactions on* **11**, 1018 (1975).

[10] G. Binasch, P. Grünberg, F. Saurenbach, and W. Zinn, *Phys. Rev. B* **39**, 4828 (1989).

[11] M. N. Baibich, J. M. Broto, A. Fert, F. N. Van Dau, F. Petroff, P. Etienne, G. Creuzet, A. Friederich, and J. Chazelas, *Phys. Rev. Lett.* **61**, 2472 (1988).

[12] P. Grünberg, R. Schreiber, Y. Pang, M. B. Brodsky, and H. Sowers, *Phys. Rev. Lett.* **57**, 2442 (1986).

[13] M. Julliere, *Physics Letters A* **54**, 225 (1975).

[14] S. Ikeda, J. Hayakawa, Y. Ashizawa, Y. M. Lee, K. Miura, H. Hasegawa, M. Tsunoda, F. Matsukura, and H. Ohno, *Applied Physics Letters* **93**, 082508 (2008).

[15] F. J. Jedema, A. T. Filip, and B. J. van Wees, *Nature* **410**, 345 (2001).

[16] F. J. Jedema, M. S. Nijboer, A. T. Filip, and B. J. van Wees, *Phys. Rev. B* **67**, 085319 (2003).

[17] S. A. Wolf, D. D. Awschalom, R. A. Buhrman, J. M. Daughton, S. von Molnár, M. L. Roukes, A. Y. Chtchelkanova, and D. M. Treger, *Science* **294**, 1488 (2001).

[18] F. Kuemmeth, S. Ilani, D. C. Ralph, and P. L. McEuen, *Nature* **452**, 448 (2008).

[19] A. Cottet, T. Kontos, S. Sahoo, H. T. Man, M.-S. Choi, W. Belzig, C. Bruder, A. F. Morpurgo, and C. Schönenberger, *Semiconductor Science and Technology* **21**, S78 (2006).

[20] G. A. Prinz, *Science* **282**, 1660 (1998).

[21] M. Bockrath, D. H. Cobden, P. L. McEuen, N. G. Chopra, A. Zettl, A. Thess, and R. E. Smalley, *Science* **275**, 1922 (1997).

[22] R. Meservey and P. M. Tedrow, *Physics Reports* **238**, 173 (1994).

[23] B. Zhao, I. Mönch, H. Vinzelberg, T. Mühl, and C. M. Schneider, *Appl. Phys. Lett.* **80**, 3144 (2002).

[24] W. G. Stirling, R. A. Cowley, and M. W. Stringfellow, *Journal of Physics F: Metal Physics* **2**, 421 (1972).

[25] S. Sahoo, T. Kontos, J. Furer, C. Hoffmann, M. Graber, A. Cottet, and C. Schönenberger, *Nat. Phys.* **1**, 99 (2005).

[26] C. Feuillet-Palma, T. Delattre, P. Morfin, J.-M. Berroir, G. Fève, D. C. Glattli, B. Plaçais, A. Cottet, and T. Kontos, *Phys. Rev. B* **81**, 115414 (2010).

[27] D. Steininger, A. K. Hüttel, M. Ziola, M. Kiessling, M. Sperl, G. Bayreuther, and C. Strunk, *Journal of Applied Physics* **113**, 034303 (2013).

[28] H. Takahashi, S. Tsunashima, S. Iwata, and U. S, *Jpn. J. Appl. Phys.* **32**, L1328 (1993).

[29] C. Morgan, K. Schmalbuch, F. García-Sánchez, C. M. Schneider, and C. Meyer, *Journal of Magnetism and Magnetic Materials* **325**, 112 (2013).

[30] C. Morgan, C. M. Schneider, and C. Meyer, *Journal of Applied Physics* **111**, 07B309 (2012).

[31] C. Meyer, C. Morgan, and C. M. Schneider, *physica status solidi (b)* **248**, 2680 (2011).

[32] C. Morgan, D. Metten, C. M. Schneider, and C. Meyer, *physica status solidi (b)* (2013).

[33] S. Blundell, *Magnetism in condensed matter.*, Oxford University Press, 2001.

[34] E. C. Stoner, *Proceedings of the Royal Society of London. Series A - Mathematical and Physical Sciences* **154**, 656 (1936).

[35] W. Heisenberg, *Zeitschrift für Physik* **49**, 619 (1928).

[36] R. Skomski, *Simple models of magnetism*, Oxford Graduate Texts, Oxford Univ. Press, Oxford, 2008.

[37] I. I. Mazin, *Phys. Rev. Lett.* **83**, 1427 (1999).

[38] H. Ibach and H. Lüth, *Festkörperphysik - Einführung in die Grundlagen*, Springer Verlag, 2009.

[39] M. Müller, *Electronic structure of ferromagnet-insulator interfaces: Fe/MgO and Co/MgO*, Phd thesis, Universität Duisburg-Essen, 2007.

[40] J. Stöhr and H. C. Siegmann, *Magnetism - from fundamentals to nanoscale dynamics*, Springer Verlag, 2006.

[41] B. D. Cullity, *Introduction to magnetic materials*, Addison-Wesley Publishing Company, 1973.

[42] F. García-Sánchez, *Modeling of field and thermal magnetization reversal in nanostructured magnetic materials*, Phd thesis, Universidad Autónoma de Madrid, 2007.

[43] E. Friend, *Interaction of stress and magnetic properties in patterned copper-nickel-copper thin films*, Phd thesis, Massachusetts Institute of Technology, 2007.

[44] W. L. Roth, *Journal of Physics and Chemistry of Solids* **25**, 1 (1964).

[45] C. Kittel, *Phys. Rev.* **70**, 965 (1946).

[46] S. J. Yuan, L. Wang, S. M. Zhou, M. Lu, J. Du, and A. Hu, *Applied Physics Letters* **81**, 3428 (2002).

[47] S. Krause, L. Berbil-Bautista, T. Hänke, F. Vonau, M. Bode, and R. Wiesendanger, *Europhysics Letters* **76**, 637 (2006).

[48] C. Haas, *Phys. Rev.* **168**, 531 (1968).

[49] N. F. Mott, *Proceedings of the Royal Society of London. Series A - Mathematical and Physical Sciences* **153**, 699 (1936).

[50] B. Dieny, *Journal of Magnetism and Magnetic Materials* **136**, 335 (1994).

[51] P. A. Grünberg, *Sensors and Actuators A: Physical* **91**, 153 (2001).

[52] Y. Sakuraba, K. Izumi, T. Iwase, S. Bosu, K. Saito, K. Takanashi, Y. Miura, K. Futatsukawa, K. Abe, and M. Shirai, *Phys. Rev. B* **82**, 094444 (2010).

[53] L. V. Radushkevich and V. M. Lukyanovich, *Soviet Journal of Chemical Physics* **26**, 88 (1952).

[54] A. Oberlin, M. Endo, and T. Koyama, *Journal of Crystal Growth* **32**, 335 (1976).

[55] S. Iijima, *Nature* **354**, 56 (1991).

[56] S. Iijima and T. Ichihashi, *Nature* **363**, 603 (1993).

[57] W. Hoenlein, F. Kreupl, G. Duesberg, A. Graham, M. Liebau, R. Seidel, and E. Unger, *Materials Science and Engineering: C* **23**, 663 (2003).

[58] S. Heedt, C. Morgan, K. Weis, D. E. Bürgler, R. Calarco, H. Hardtdegen, D. Grützmacher, and T. Schäpers, *Nano Letters* **12**, 4437 (2012).

[59] C. Spudat, *Correlation between Raman spectroscopy and electron microscopy on individual carbon nanotubes and peapods*, Phd thesis, Universität Duisburg-Essen, 2010.

[60] S. Reich, C. Thomsen, and J. Maultzch, *Carbon nanotubes - basic concepts and physical properties*, Wiley - VCH Verlag, 2004.

[61] X. Zhao, Y. Liu, S. Inoue, T. Suzuki, R. O. Jones, and Y. Ando, *Phys. Rev. Lett.* **92**, 125502 (2004).

[62] P. R. Wallace, *Phys. Rev.* **71**, 622 (1947).

[63] S. Reich, J. Maultzsch, C. Thomsen, and P. Ordejón, *Phys. Rev. B* **66**, 035412 (2002).

[64] S. Ilani and P. L. McEuen, *Annual Review of Condensed Matter Physics* **1**, 1 (2010).

[65] A. K. Geim and K. S. Novoselov, *Nature Materials* **6** (2007).

[66] E. D. Minot, Y. Yaish, V. Sazonova, J.-Y. Park, M. Brink, and P. L. McEuen, *Phys. Rev. Lett.* **90**, 156401 (2003).

[67] A. Thess, R. Lee, P. Nikolaev, H. Dai, P. Petit, J. Robert, C. Xu, Y. H. Lee, S. G. Kim, A. G. Rinzler, D. T. Colbert, G. E. Scuseria, D. Tomanek, J. E. Fischer, and R. E. Smalley, *Science* **273**, 483 (1996).

[68] J. Kong, H. T. Soh, A. M. Cassell, C. F. Quate, and H. J. Dai, *Nature* **395** (1998).

[69] K. Goss, A. Kamra, C. Spudat, C. Meyer, P. Kögerler, and C. M. Schneider, *physica status solidi (b)* **246**, 2494 (2009).

[70] R. Landauer, *IBM Journal of Research and Development* **1**, 223 (1957).

[71] M. Büttiker, *Phys. Rev. Lett.* **57**, 1761 (1986).

[72] D. Mann, A. Javey, J. Kong, Q. Wang, and H. Dai, *Nano Letters* **3**, 1541 (2003).

[73] J. Kong, E. Yenilmez, T. W. Tombler, W. Kim, H. Dai, R. B. Laughlin, L. Liu, C. S. Jayanthi, and S. Y. Wu, *Phys. Rev. Lett.* **87**, 106801 (2001).

[74] M. Biercuk, S. Ilani, C. Marcus, and P. McEuen, *Carbon nanotubes*, Springer, 2008.

[75] S. Heinze, J. Tersoff, R. Martel, V. Derycke, J. Appenzeller, and P. Avouris, *Phys. Rev. Lett.* **89**, 106801 (2002).

[76] L. Hong-Xia, D. Zheng-Chao, and F. Hao, *Chinese Physics B* **17**, 680 (2008).

[77] A. Jensen, J. R. Hauptmann, J. Nygård, and P. E. Lindelof, *Phys. Rev. B* **72**, 035419 (2005).

[78] A. W. Hull, *Phys. Rev.* **17**, 571 (1921).

[79] E. Chason and T. Mayer, *Crit. Rev. Solid State* **22**, 1 (1997).

[80] F. Schmidt and A. Hubert, *Journal of Magnetism and Magnetic Materials* **61**, 307 (1986).

[81] S. Hashimoto, Y. Ochiai, and K. Aso, *Japanese Journal of Applied Physics* **28**, 1596 (1989).

[82] J.-R. Jeong, J. Kim, J.-W. Lee, S.-K. Kim, and S.-C. Shin, *Applied Physics Letters* **79**, 3296 (2001).

[83] M. J. Donahue and D. G. Porter, *OOMMF Users Guide, Version 1.0* **NISTR 6376** (1999).

[84] H. Callen and E. Callen, *Journal of Physics and Chemistry of Solids* **27**, 1271 (1966).

[85] Z. A. Kaszkur and B. Mierzwa, *Philosophical Magazine A* **77**, 781 (1998).

[86] G. Sarau, *Spin-dependent transport in cobalt nanocontacts*, Phd thesis, Universität Duisburg-Essen, 2006.

[87] H. Aurich, A. Baumgartner, F. Freitag, A. Eichler, J. Trbovic, and C. Schönenberger, *Applied Physics Letters* **97**, 153116 (2010).

[88] D. Metten, *Magnetoresistance measurements on carbon nanotubes with CoPd contacts*, Dipl. thesis, Rheinische Friedrich-Wilhelms-Universität Bonn, 2012.

[89] S. Krompiewski, *physica status solidi (b)* **242**, 226 (2005).

[90] P. M. Tedrow and R. Meservey, *Phys. Rev. B* **7**, 318 (1973).

[91] L. E. Hueso, J. M. Pruneda, V. Ferrari, G. Burnell, J. P. Valdés-Herrera, B. D. Simons, P. B. Littlewood, E. Artacho, A. Fert, and N. D. Mathur, *Nature* **445**, 410 (2007).

[92] J. C. Slonczewski, *Phys. Rev. B* **39**, 6995 (1989).

[93] M. Johnson and R. H. Silsbee, *Phys. Rev. Lett.* **55**, 1790 (1985).

[94] E. S. Garlid, *Electrical detection of the Spin Hall Effect in ferromagnet-semiconductor heterostructures*, Phd thesis, University of Minnesota, 2010.

[95] M. Tran, H. Jaffrès, C. Deranlot, J.-M. George, A. Fert, A. Miard, and A. Lemaî tre, *Phys. Rev. Lett.* **102**, 036601 (2009).

[96] S. P. Dash, S. Sharma, R. S. Patel, M. P. de Jong, and R. Jansen, *Nature* **462**, 491 (2009).

[97] J. Fischer, B. Trauzettel, and D. Loss, *Phys. Rev. B* **80**, 155401 (2009).

[98] M. Schneider, J. Liszkowski, M. Rahm, W. Wegscheider, D. Weiss, H. Hoffmann, and J. Zweck, *Journal of Physics D: Applied Physics* **36**, 2239 (2003).

[99] H. T. Man, I. J. W. Wever, and A. F. Morpurgo, *Phys. Rev. B* **73**, 241401 (2006).

[100] K. Tsukagoshi, N. Yoneya, S. Uryu, Y. Aoyagi, A. Kanda, Y. Ootuka, and B. Alphenaar, *Physica B: Condensed Matter* **323**, 107 (2002).

[101] P. E. Lindelof, J. Borggreen, A. Jensen, J. Nygard, and P. R. Poulsen, *Phys. Scr. T* **102** (2002).

[102] J.-R. Kim, H. M. So, J.-J. Kim, and J. Kim, *Phys. Rev. B* **66**, 233401 (2002).

[103] C. Spudat, C. Meyer, K. Goss, and C. M. Schneider, *physica status solidi (b)* **246**, 2498 (2009).

[104] Y. Qi, D. Y. Xing, and J. Dong, *Phys. Rev. B* **58**, 2783 (1998).

[105] C. T. Black, C. B. Murray, R. L. Sandstrom, and S. Sun, *Science* **290**, 1131 (2000).

[106] T. Sasaki, T. Oikawa, M. Shiraishi, Y. Suzuki, and K. Noguchi, *Applied Physics Letters* **98**, 012508 (2011).

[107] T. Last, M. Wahle, S. Hacia, S. F. Fischer, and U. Kunze, *Journal of Superconductivity: Incorporating Novel Magnetism* **18**, 385 (2005).

[108] W. Han and R. K. Kawakami, *Phys. Rev. Lett.* **107**, 047207 (2011).

[109] S. Vitusevich and F. Gasparyan, *Low frequency noise spectroscopy at nanoscale: carbon nanotube materials and devices, carbon nanotubes applications in electron devices*, InTech, 2011.

[110] M. Zheng, A. Jagota, E. D. Semke, B. A. Diner, R. S. Mclean, S. R. Lustig, R. E. Richardson, and N. G. Tassi, *Nature Materials* **2**, 338 (2003).

[111] Y. Zhang, N. W. Franklin, R. J. Chen, and H. Dai, *Chemical Physics Letters* **331**, 35 (2000).

[112] J. S. Moodera, T. S. Santos, and T. Nagahama, *Journal of Physics: Condensed Matter* **19**, 165202 (2007).

[113] M. Müller, M. Luysberg, and C. M. Schneider, *Applied Physics Letters* **98**, 142503 (2011).

[114] A. R. Harutyunyan, E. Mora, T. Tokune, K. Bolton, A. Rosén, A. Jiang, N. Awasthi, and S. Curtarolo, *Applied Physics Letters* **90**, 163120 (2007).

[115] K. Goss, *Interactions between parallel carbon nanotube quantum dots*, Phd thesis, Universität Duisburg-Essen, 2011.

List of Publications

(in chronological order)

Papers

- G. D. Nessim, A. J. Hart, J. S. Kim, D. Acquaviva, J. Oh, **C. Morgan**, M. Seita, J. S. Leib, and C. V. Thompson "Tuning of vertically-aligned carbon nanotube diameter and areal density through catalyst pre-treatment" *Nano Letters* **8**, (11), 3587 (2008).
- C. Meyer, **C. Morgan**, and C. M. Schneider "Spin transport in ferromagnetically-contacted carbon nanotubes" *physica status solidi (b)* **248**, 2680 (2011).
- **C. Morgan**, C. M. Schneider, and C. Meyer "Permalloy and $Co_{50}Pd_{50}$ as ferromagnetic contacts for magnetoresistance measurements in carbon nanotube-based transport structures" *J. Appl. Phys.)* **111**, 07B309 (2012).
- S. Heedt, **C. Morgan**, K. Weis, D. E. Bürgler, R. Calarco, H. Hardtdegen, D. Grützmacher, and Th. Schäpers "Electrical spin injection into InN semiconductor nanowires" *Nano Letters* **12** (9), 4437 (2012).
- **C. Morgan**, K. Schmalbuch, F. Garcia-Sanchez, C. M. Schneider, and C. Meyer "Structure and magnetization in CoPd thin films and nanocontacts" *Journal of Magnetism and Magnetic Materials* **325**, 112-116 (2013).
- **C. Morgan**, D. Metten, C. M. Schneider, and C. Meyer "Effect of contact geometry on magnetoresistance in CoPd-contacted carbon nanotubes" *physica status solidi (b)* (accepted 2013).

Poster Contributions

- **C. Morgan**, K. Goß C. Meyer, C. M. Schneider
  "Fabrication of CNT-based devices for spin transport measurements"
  CNR Department of Materials and Devices National School "Physics of spin in matter" 02.09.11.2009, Chiavari (Italy).
- **C. Morgan**, K. Goß, C. Meyer, C. M. Schneider
  "CNT-based devices for transport measurements and characterization"
  16th International Winterschool on New Developments in Solid State Physics, 2010, Mauterndorf (Austria).
- **C. Morgan**, K. Goß, C. Meyer, C. M. Schneider
  "CNT-based devices for transport measurements and characterization"
  Frühjahrstagung SKM 2010 der DPG in Regensburg (Germany).
- **C. Morgan**, C. Meyer, K. Schmalbuch, C. M. Schneider
  "Magnetoresistance in ferromagnetically contacted carbon nanotube devices"
  JARA-FIT Nanoelectronic Days 2010, 04-07.4.2010 Aachen (Germany).
- C. Meyer, **C. Morgan**, K. Schmalbuch, C. M. Schneider
  "Ferromagnetically contacted CNTs for spin injection"
  International Winterschool on Electronic Properties of Novel Materials, 2011, Kirchberg (Austria).
- **C. Morgan**, D. Metten, K. Schmalbuch, C. M. Schneider, C. Meyer
  "Permalloy and $Co_{50}Pd_{50}$ as ferromagnetic contacts for TMR measurements in CNT-based devices"
  56th Conference on Magnetism and Magnetic Materials, 30.10-03.11.2011, Scottsdale, AZ (USA).
- D. Metten, **C. Morgan**, C. M. Schneider, C. Meyer
  "Magnetoresistance on carbon nanotubes with CoPd contacts"
  Frühjahrstagung SKM 2012 der DPG in Berlin (Germany).
- **C. Morgan**, D. Metten, K. Schmalbuch, C. M. Schneider, C. Meyer
  "Magnetoresistance in carbon nanotubes with CoPd contacts"
  21st International Colloquium on Magnetic Films and Surfaces, 24-28.09.2012, Shanghai (People's Republic of China).
- **C. Morgan**, D. Metten, C. M. Schneider, C. Meyer
  "Magnetoresistance in carbon nanotubes with $Co_{50}Pd_{50}$ contacts"
  International Winterschool on Electronic Properties of Novel Materials, 2013, Kirchberg (Austria).

Talks

- ”Ferromagnetic contacts for magnetoresistance measurements of carbon nanotube-based devices”
  Deutsche Physikerinnentagung, 2010, München
- ”Ferromagnetically contacted carbon nanotubes for spin injection”
  2011 Früjahrstagung SKM der DPG in Dresden

Acknowledgements

For the past years, I have had the privilege of being in a wonderful environment. The people that I interacted with on a daily basis both at work and at home have had a profound impact on both this thesis and my own personal growth.

First, I would like to thank **Prof. Claus M. Schneider** for giving me the opportunity to work on my PhD here in Jülich, and for always being there with a joke or a word of advice. It has been a great experience working at the PGI-6, where there is so much expertise and motivation.

I thank **Dr. Daniel Bürgler** for agreeing to take the time to be the second referee for this thesis, and for always having some friendly advice, from topics ranging from physics to running.

To **Dr. Carola Meyer**, the head of the nanotube group, thank you for being a wonderful doctor mother on a daily basis. I was very lucky to get a position in your Young Investigator's group, and I really appreciated the energy and the team approach you provided. Thanks for being such a great role model, and for all your support in the last years.

The other student members of the nanotube group always contributed to the friendly environment. I would like to acknowledge **Christian Spudat** for his help in learning about the chemistry lab and CNT growth. **Karin Goß**, thank you for teaching me so much about fabrication and transport, and for being a wonderful office mate, as well as a friend. **Robert Frielinghaus**, thank you for being a great group leader in Carola's absence, and for taking the time to organize so many activities outside of work. To **Michael Schnee**, thank you for the many conversations, and for fuelling my GoT addiction. I would like to acknowledge **Dominik Metten** for his work with me as a Diploma student. Working with Dominik was a great learning experience for me, and I thank him for both his motivation and sense of fun. I would also like

to thank **Fabian Fritz** for being a great office mate.

Outside of the nanotube group, there were many other people who contributed to the good atmosphere of the institute. I would like to thank all my colleagues at the PGI-6, especially the lunch/coffee group for both good times and support. I would also like to acknowledge **Tobias Burnus**, who was one of my office mates for several years and was always ready to offer help, from solving Latex problems to helping me move to a new apartment. To **Raji** and **Hatice**, thank you for being good friends. **Claire Besson**, thank you for the many fun times and adventures ranging from bike rides to dinner parties to vacations in Paris.

Fabricating my samples involved a lengthly process, and there were many people who helped along the way. I would like to thank **Dr. Stefan Trellenkamp** for his extemely efficient and high accuracy e-beam writing, and for answering all my questions about the process. I acknowledge the staff of the PGI-7 cleanroom, **Holger John, René Borowski, and Mirka Grates** for keeping the clean room in excellent condition and for always helping with processing steps. I would also like to thank **Reinert Schreiber and Thomas Jansen** for MBE growth and **Christoph Krause and Hans Wingens** for metal evaporation.

I thank Artur Glavic for showing me how to use the MFM, and I acknowledge **Klaus Schmalbuch** for his help with magnetic characterization at the RWTH. Also, many thanks to **Felipe García-Sánchez** for always offering me clear explanations to the theory of micromagnetism, often providing a good explanation to my experimental results.

I would like to thank **Prof. Thomas Schäpers** for the use of the magnet lab for many of my transport measurements. Also, thanks to **Herbert Kertz** for keeping all the equipment in working condition, and for always being there to help with Helium transfers and leak testing. I would especially like to acknowledge **Sebastian Heedt** for his many collaborations, helpful discussions, and being a good friend.

In our own transport lab, I was lucky to have the help of **Heinz Pfeifer** with electronics, **Franz-Josef Köhne** with the cryostat setup, and **Norbert Schnitzler** and **Jürgen Lauer** with labview. With your help, we managed to get everything up and running on a (fairly) normal basis.

Thank you very much to **Jutta Gollnick and Margret Frey** for always helping with administrative things.

I would certainly not be the person I am today without my family and friends. I acknowledge my parents **Tim and Cindy Morgan** who have been and always will be there for me with unconditional love and support, and my Grandmother, **Virginia Dunne**, who always understood and supported the importance of education. My sister **Nora Morgan** has been with me for almost my entire life, and is always a great person to talk to. I would also like to acknowledge my new family here in Germany - one of the best parts of living in the Aachen/Jülich region was getting to know you better. I thank my friends, especially **Kate Soto and Martin Segado**, for being with my since day one of our time at MIT, and **Kendra Bussey**, for her friendship and for following me to Europe.

Finally, I come to the people who are with me every day. My son **Frederik** was born during the course of this thesis, and watching and helping him grow has been an extraordinary experience. My husband **Christian** has been by my side for the most important moments of my life, and his love and support are invaluable.

Curriculum Vitae

Personal Data

Caitlin Morgan
born 19.02.1985 in Syracuse, New York (USA)
American

Education

09/1999 – 06/2003	C. W. Baker High School, Baldwinsville NY
06/2002	Graduated with Honors
09/2003 – 06/2007	Massachusetts Institute of Technology, Cambridge
05/2008	BSc in Materials Science and Engineering Supervisor: Prof. Dr. C. V. Thompson Dept. Mat. Sci. Eng.
10/2007 – 04/2009	Technische Universität München
05/2008	MSc in Materials Science Supervisor: Prof. Dr. Anna Fontcuberta i Morral Lehrstuhl für Experimentelle Halbleiter Physik 1
since 05/2009	Peter Grünberg Institut Forschungszentrum Jülich Ph.D. candidate in physics Supervisor: Prof. Dr. C. M. Schneider PGI-6, Elektronische Eigenschaften

Work Experience

06/2006 – 09/2006	Continental AG in Hannover, Germany Internship in group Advanced Tire Materials
06/2007 – 10/2007	OSRAM OS GmbH in Regensburg, Germany Internship in group Back End Technology

Jülich, September 06, 2012

Erklärung

Hiermit erkläre ich, dass ich die vorliegende Arbeit selbstständig und ohne fremde Hilfe verfasst habe. Ferner habe ich außer den angegebenen Quellen keine anderen Quellen und Hilfsmittel benutzt. Die dem Sinn oder Wortlaut nach entnommenen Textpassagen oder Abbildungen habe ich in jedem Einzelfall kenntlich gemacht. Dieser Dissertation geht weder ein erfolgloser Promotionsversuch voraus, noch wurde sie in einem weiteren Promotionsverfahren eingereicht. Abgesehen von den angegebenen Publikationen sind die Ergebnisse dieser Dissertation unveröffentlicht. Diese Dissertation, die den Doktorgrad "Dr. rer. nat." anstrebt, wurde von Prof. Dr. C. M. Schneider betreut.

Jülich, den 12. Juli 2013

Caitlin Morgan

Band / Volume 65
Solutions of Exercises in “An Introduction to Dynamics of Colloids”
J. K. G. Dhont, K. Kang (2013), 143 pp
ISBN: 978-3-89336-882-2

Band / Volume 66
Strukturelle und chemische Charakterisierung von selbst-assemblierten Monolagen organischer Moleküle auf Oberflächen
M. Müller (2013), 168 pp
ISBN: 978-3-89336-883-9

Band / Volume 67
Adsorption of (hetero-)organic Phthalocyanine and PTCDA thin films on Ag(111)
C. Kleimann (2013), iv, 149 pp
ISBN: 978-3-89336-888-4

Band / Volume 68
High-energy high-momentum surface spin waves of ultrathin epitaxial 3d transition metal films
R. Jayaraman (2013), ix, 135 pp
ISBN: 978-3-89336-890-7

Band / Volume 69
Magnetic Oxide Heterostructures: EuO on Cubic Oxides and on Silicon
C. Caspers (2013), xiii, 153 pp
ISBN: 978-3-89336-891-4

Band / Volume 70
Femtosecond Spin Dynamics in Magnetic Multilayers Employing High Harmonics of Laser Radiation
D. Rudolf (2013), vi, 121 pp
ISBN: 978-3-89336-894-5

Band / Volume 71
Development and application of a massively parallel KKR Green function method for large scale systems
A. R. Thieß (2013), ii, 173 pp
ISBN: 978-3-89336-906-5

Band / Volume 72
Conformational Dynamics of Calmodulin and Ribosome-Nascent Chain Complexes Studied by Time-Resolved Fluorescence Anisotropy
P. Lamprou (2013), 182 pp
ISBN: 978-3-89336-907-2

Band / Volume 73
Stereoselective synthesis of vicinal diols with enzymatic cascade reactions
J. Kulig (2013), XV, 177 pp
ISBN: 978-3-89336-911-9

Band / Volume 74
Computing Solids
Models, ab-initio methods and supercomputing
Lecture Notes of the 45th IFF Spring School 2014
March 10 – 21, 2014 Jülich, Germany
ed. by S. Blügel, N. Helbig, V. Meden, D. Wortmann (2014), ca. 1000 pp
ISBN: 978-3-89336-912-6

Band / Volume 75
Aberrationskorrigierte Photoemissionsmikroskopie an magnetischen Systemen: Von statischer Charakterisierung zu zeitaufgelöster Abbildung
F. Nickel (2013), x, 99 pp
ISBN: 978-3-89336-913-3

Band / Volume 76
Temperature-Induced Metamagnetic Transition and Domain Structures of Single-Crystalline FeRh Thin Films on MgO(100)
X. Zhou (2013), xi, 104 pp
ISBN: 978-3-89336-919-5

Band / Volume 77
Interplay between Magnetism and Superconductivity in Iron Based High Temperature Superconductors
S. Price (2013), 196 pp
ISBN: 978-3-89336-921-8

Band / Volume 78
Magnetoresistance and transport in carbon nanotube-based devices
C. Morgan (2013), viii, 131 pp
ISBN: 978-3-89336-926-3

Weitere ***Schriften des Verlags im Forschungszentrum Jülich*** unter
http://wwwzb1.fz-juelich.de/verlagextern1/index.asp

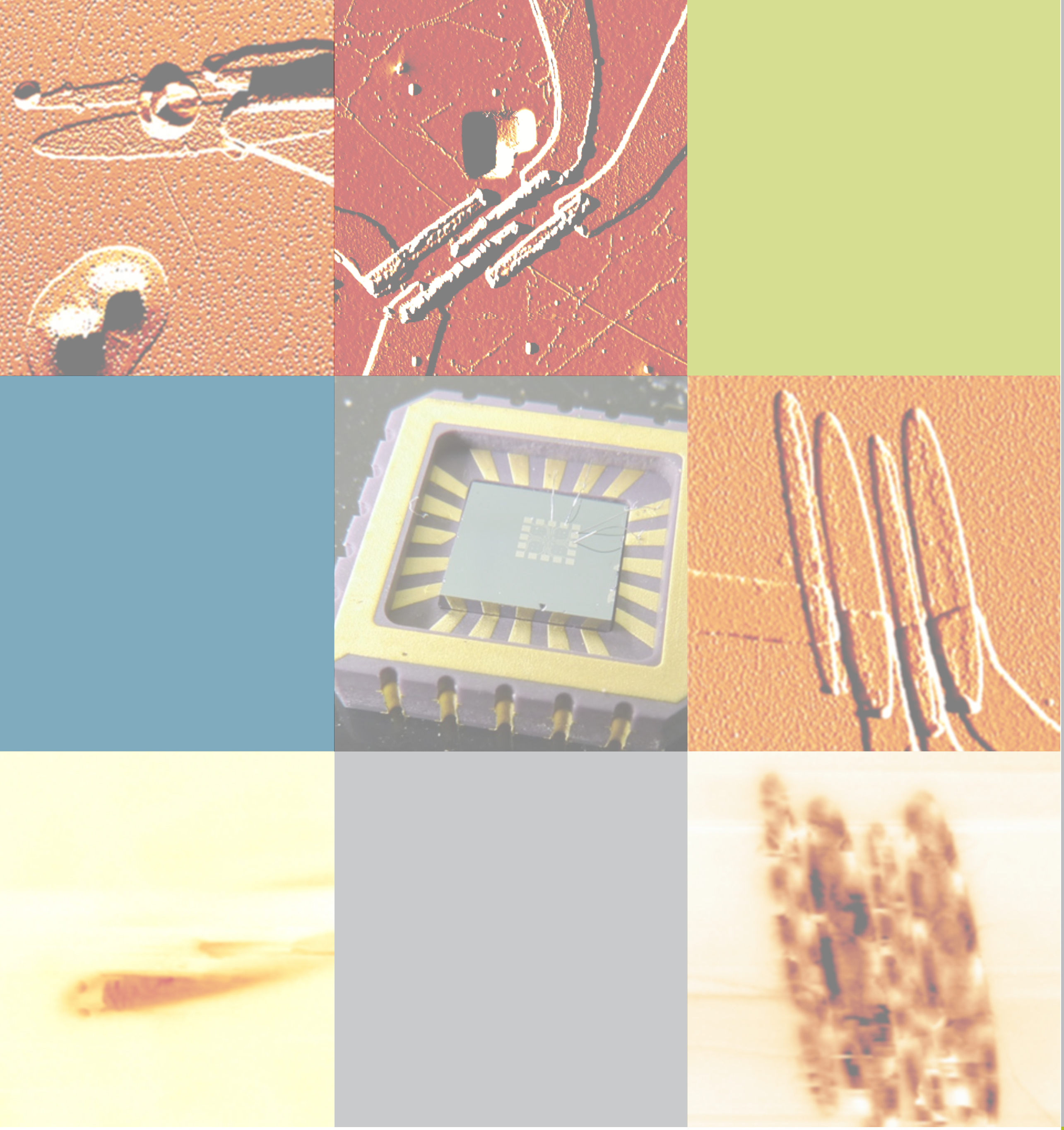

Schlüsseltechnologien / Key Technologies
Band / Volume 78
ISBN 978-3-89336-926-3

JÜLICH
FORSCHUNGSZENTRUM